UNIVERSITA' DEGLI STUDI DI MILANO

FACOLTÀ DI SCIENZE E TECNOLOGIE
SCUOLA DI DOTTORATO IN INFORMATICA
DIPARTIMENTO DI INFORMATICA
DOTTORATO DI RICERCA IN INFORMATICA, XXVII CICLO

NON-BLIND SOURCE SEPARATION AND FEATURE EXTRACTION:

THEORY, APPROACH AND CASE STUDIES IN CARDIAC SIGNALS

INF/01

Doctoral dissertation of:
Massimo Walter Rivolta

Supervisor:
Roberto Sassi

Doctorate school's director:
Prof. Ernesto Damiani

XXVII Doctorate cycle, 2011 – 2014

ACKNOWLEDGMENTS

First of all, I would like to thank Prof. Roberto Sassi, head of the Biomedical image and Signal Processing Laboratory (BiSP Lab) who has supervised me for more than three years. He helped me as a friend in several situations regarding both work and life. Having a good mentor makes the difference.

Second, I thank all the referees for their useful suggestions to improve the quality of this manuscript. They are Luca Mainardi, Jean-Philippe Couderc and Francisco Sales Castells-Ramòn. In particular, Luca as a very expert co-author in many publications, and Jean-Philippe who has taught me to valorize and present my works.

Third, I express my gratitude to Mr. Md Aktaruzzaman, Mr. Matteo Migliorini and Dr. Valentina Corino, unique fellows who have shared their lives during my PhD. I would also like to thank all my other collegues as Mr. Ebadollah Kheirati Roonizi, Dr. Angelo Genovese, Dr. Ruggero Donida from the Universitá degli Studi di Milano.

Finally, I need to thank my family for the encouragements they have always given to me.

ABSTRACT

Source separation (SS) and feature extraction (FE) are tools employed in digital signal processing. The former permits to estimate the values of some sources that have been mixed, and the latter extracts features from a set of measurements.

SS and FE are widely applied on biomedical signals such as electrocardiogram (ECG), electroencephalogram, arterial blood pressure, etc., because these signals are collected in noisy environments. For instance, ECG recordings show the electrical activity generated by the whole heart at once. Yet, there are cardiac pathologies or arrhythmias related to only the atrial or ventricular chambers and thus, tools capable to separate them become fundamental for the diagnosis, prognosis and prediction of life-threatening events. Therefore, the quality of treatments depends on the reliability of the features extracted from the signals and then, the reduction of possible interferences becomes very relevant in this context.

The study and the development of new SS technique play an important role in those application in which the components of a measurement cannot be splitted using classical temporal or frequency analysis. In addition, non-blind SS aims to employ further information and to develop mathematical and statistical model to make the estimates more reliable.

Features extraction is fundamental for the classification task. In biomedical signals, features are used to characterize the status of the subjects in either healthy or pathological condition. For example, features to predict the risk of developing cardiac arrhythmias are continuously encouraged by regulatory agencies as the US Food and Drug Administration.

The study of reliability and feasibility of features requires an extensive use of tests. These tests are necessary to evaluate some properties, *e.g.*, the capability of the feature to be resilient to noise, variability of the estimate, classification power, etc.

The aim of this thesis is to study, develop, validate and test new SS techniques and features applicable to different kind of signals. The new algorithms and features are extensively studied to characterize their properties from a methodological point of view. In addition, simulated and real data are considered as a test bench. Cardiac signals will be the specific field of application.

First, a new algorithm for non-blind SS will be presented and discussed. In particular, this new methodology is an extension of a well-known algorithm, *i.e.*, template, matching and subtraction (TMS), normally used to estimate transient sources, *i.e.*, sources that are located only somewhere in the signals, in stationary conditions. TMS estimates the values of the source by averaging a set of measurements in which it is known to be constant over time. However, there are situations in which this assumption does not hold and the results obtained are not "good" estimates. In order to track changes over

time, we proposed a method based on a multi-goal optimization problem to modulate the estimate provided by the classic TMS.

The multi-goal optimization problem has been defined as a weighted sum of three subgoals measuring: i) difference in the power of the residue and that of the signal when the transient source is not present; ii) difference in the power of the first derivative of the residue and that of the signal when the transient source is not present; and iii) difference between the estimate provided by the classic TMS and its modulated version.

A multi-particle swarm optimization algorithm was used to find the solution of a non-linear problem in a very high dimensional space (a vector $\in \Re^{100}$). This technique employs a set of particles that moves in the search space with an heuristic rule and it has been shown to be highly robust to local optima.

The algorithm was tested on synthetic and real data. First, a synthetic dataset was generated and the mean square error between the real source and the estimated one was determined. Second, a dataset collected from subjects undergoing ablation for the treatment of atrial fibrillation (AF) was employed. These signals contain both atrial and ventricular activity, but only the atrial one can be used by clinicians to perform the ablation. We tried to separate the atrial activity from the ventricular one. Two features, *i.e.*, the amplitude reduction of the ventricular peak (VDR) and the percentage of residues in which their power was outside the 95^{th} percentile of the atrial one (PP), were computed as measure of goodness of the separation.

In both tests, the modulated TMS provided better performance than the classic TMS ($p < 0.001$), suggesting that a power-based modulation could be suitable to keep tracking the morphology of the ventricular activity.

Second, three features have been study and tested. These three features can determine: i) the variability of times of occurrence of transient sources ($\mathcal{V}$-index); ii) the organization of the propagation of wavefronts (OD); and iii) the average acceleration (AC) and deceleration capacities (DC) of a system.

Briefly, the $\mathcal{V}$-index is particularly suitable to be applied on signals in which: i) multiple measurements are available; ii) transient sources are linearly mixed; iii) the shape of each realization of the transient sources are similar between each other; and iv) the variability of the times of occurrence is relatively small. It is based on two models, a linear equivalent surface model and a statistical model, respectively. When applied on the T-wave of the ECG, it can provide an estimate of the spatial heterogeneity of the ventricular repolarization, measured as the standard deviation of the repolarization times of the myocytes. This index was tested on three scenario: i) before and after administration of sotalol; ii) before and after administration of moxifloxacin; and iii) on subjects affected by Chagas disease. In all the three cases, the $\mathcal{V}$-index was sensitive to the known effects of the drugs on the ventricular repolarization as well as symptoms of the Chagas disease ($p < 0.05$).

The second feature combines morphological, temporal and organization information to build a new index more suitable for the characterization of wave propagation. In several situations, sensors are not sensitive to the direction of the wave propagation because they can measure only scalar quantities: this is typical for electrodes. The use

of multiple sensors permits to quantify/estimate the direction of the wave propagation. We proposed a new index, the organization degree (OD), to measure the degree of organization of a series of symbolic words. Each symbolic word is built labelling the electrical activity and the time of arrival of an electrical wave detected by a set of electrodes using a symbol for each signal. A sequence of words is then built for each wave detected and the Shannon entropy was used to determine the organization.

OD was tested on a real dataset collected on subjects suffering from atrial fibrillation in four different situations: i) before and after the onset of AF; and ii) before and after the onset of AF after infusion of isoproterenol (ISO). Such drug stimulates the activation of the sympathetic branch of the autonomous nervous system and it is supposed to decrease the organization of the atrial activity (making it more "random"). OD was able to discriminate between all the cases ($p < 0.05$) and in particular between AF and AF+ISO, in which only the morphology was not.

The last feature is related to the evaluation of the acceleration and deceleration capacities of a system. Both quantities have been introduced by Bauer *et al.* and depend on three free parameters, *i.e.*, L, T and s. This index is built determining a list of anchor points that satisfy a specific rule (acceleration or deceleration rule) depending on the T value. Then, all the portions of signals of length 2L centered on each anchor point are aligned and then averaged. This series is called phase-rectified signal averaging (PRSA). Both capacities are computed subtracting the sum of s samples from the right side of the PRSA from the sum of s samples from the left one (divided by a normalization factor).

In this study, we investigated the role of each parameter to better understand their significance when applied on stochastic signals, specifically on inter-time beat series (RR). These tests were performed on simulated data employing different strategies. All the parameters are somehow frequency related. s, more than T, plays a role of frequency band selector in which both AC and DC are maximally sensitive. While T, acting only on the anchor point list, less affects the value of the capacities. Since it acts as a lowpass filter, T equispaced zeros are placed in the frequency domain. Finally, L permits to select the lowest oscillation detectable.

AC and DC were tested on an *in*-vivo model composed by 7 near-term pregnant sheep. The umbilical cord was occluded with three different level of strength. The main goal of this study was to determine whether AC and DC were sensitive to change in the autonomic regulation of the heart rate during lack of oxygen and if they were correlated with biomarkers such as pH, level of lactates and base deficit. Both capacities were maximally correlated with the biomarkers when using $s = T$ within $[2 - 5]$. The range of s was coherent with the frequency band related to the autonomic regulation of the fetal RR series when a lack of oxygen occurs for a little period of time.

CONTENTS

1

INTRODUCTION ON SOURCE SEPARATION AND FEATURE EXTRACTION

1.1 GENERAL INTRODUCTION AND AIM OF THE THESIS

Source separation (SS) and feature extraction (FE) are tools employed in digital signal processing; the former estimates the values of sources that have been mixed together, and the latter extracts features from a set of measurements.

SS and FE are widely applied on biomedical signals such as electrocardiogram (ECG), electroencephalogram, arterial blood pressure, etc., because these signals are collected in noisy environment. For instance, ECG recordings show the electrical activity generated by the whole heart at once. Yet, there are cardiac pathologies or arrhythmias related to only the atrial or ventricular chambers and thus, tools capable to separate them become fundamental for the diagnosis, prognosis and prediction of life-threatening events. Therefore, the quality of treatments depends on the reliability of the features extracted from the signals and then, the reduction of possible interferences becomes very relevant in this context.

The study and the development of new SS technique play an important role in those application in which the components of a measurement cannot be splitted using classical temporal or frequency analysis. In addition, non-blind SS uses additional information to develop mathematical and statistical model to make the estimates more reliable.

Features extraction is fundamental for the classification task. In biomedical signals, features are used to characterize the status of the subjects in either healthy or pathological condition. For example, features to predict the risk of developing cardiac arrhythmias are continuously encouraged by regulatory agencies as the US Food and Drug Administration (FDA).

The study of the reliability and feasibility of features requires an extensive use of tests. These tests are necessary to evaluate some properties, *e.g.*, the capability of the feature to be resilient to noise, variability of the estimate, classification power, etc.

In conclusion, the aim of this thesis is to study, develop, validate and test new SS techniques and features applicable to different kind of signals. The new algorithms and features are extensively studied to characterize their properties from a methodological point of view. In addition, simulated and real data are considered as a test bench. Cardiac signals will be the specific field of application.

In this chapter, a wide overview on non-blind source separation and feature extraction is presented.

1.2 INTRODUCTION ON SOURCE SEPARATION

During signal acquisition, data is always corrupted by noisy sources in some extent. Those noisy sources that cannot be avoided, or reduced, during the acquisition, will be carried through the next steps of the processing. *Source separation* (SS) represents a set of mathematical/probabilistic techniques able to separate sources that have been mixed.

In order to determine an estimate of the source value before the mixing, multiple assumptions on the nature of the phenomenon that has merged the measurements need to be defined. For instance, knowledges about mixing rules, statistical dependence or independence between sources and constraints on their values are important information to address the problem.

SS techniques can be distinguished in two main areas. The first one, called *blind source separation* (BSS) employs no information about the sources. This property means that the problem is highly undetermined and usually, the statistical uncorrelation or independence has to be employed for reducing this uncertainty. Typical techniques for solving BSS problems are *principal component analysis* (PCA) and *independent component analysis* (ICA), with all their variants.

The second category of techniques, called *non-blind source separation* (NBSS) is represented by those methodologies that exploit information on the sources for completing the separation task. Techniques such as *Kalman Filter* (KF), *extendend Kalman Filter* (EKF), *Bayesian Filter* (BF) and *Template, Matching and Subtracion* (TMS), are normally employed for this purpose [1].

1.2.1 NON-BLIND SOURCE SEPARATION

Since NBSS methodologies can be applied on signals collected in different environments, we will present a discussion on those techniques applied on electrocardiogram (ECG) signals (see chap. 6).

Most of the commercial electrocardiographic devices measures the ECG with a sample frequency f_s between 200 Hz and 1000 Hz. This information has to be taken into account in the development of any kind of SS technique.

Typically, ECG signals are contaminated by broad band noise, muscular artifact, powerline interference and respiration (that leads to baseline wandering). Moreover, all such noisy sources have frequency bands overlapped to that of the ECG, limiting the performance of classical numerical filters for a complete separation.

Let's take a look on a bunch of methods employed for the separation of those noisy sources. First of all, low and high frequency components are reduced using classical numerical filters. Cut-off frequencies are normally set from 0.5 to 3 Hz and from 25 to 250 Hz, depending on the application. This procedure reduces drastically the baseline wandering and both muscular and broad band noise. However, the slow waves of the ECG, as the T-wave, have low frequency components partly overlapped on that of the respiration. In this context, the baseline wander has to be removed without using classical numerical filters.

Modifications of classic adaptive filters are commonly employed for this task. For example, information about the time of occurrence of the beats can be exploited to track changes in the wandering of the baseline [2, 3]. These frameworks can be easily recast to address different problems.

Other techniques based on spline interpolation have provided interesting results in the estimation of the baseline. Such methods require to define points on the ECG in which a spline, typically cubic, is interpolated. However, the definition of these points is challenging and highly influenced by the noise. An interesting algorithm has been proposed by Brown and Arunachalam [4] in which anchor points have been selected on the T-P segment between each beat. However, if a beat is not detected, the interpolation could add artifacts.

Recently, a new method for reducing the baseline wandering has been introduced by Fasano and Villani [5, 6, 7]. This method is based on the minimization of a figure-of-merit, *i.e.*, the quadratic variation, for which it has been proven that the solution is unique. The quadratic variation measures the energy of the derivative of the signal and its minimization leads to reduce the baseline wander. Moreover, the algorithm has a complexity proportional to the number of samples of the signal to be filtered, making this technique one of the fastest available, currently.

Another important noisy source to remove is the powerline interference characterized by a fundamental frequency at 50 or 60 Hz and high order harmonics. In many application, a notch filter, typically an IIR filter, is considered a good solution when the frequency is known and not time varying. However, even when the frequency is fixed and known, the presence of steep changes in the signal, such as the QRS complexes, can lead to add undesired ringing artifacts on the ST segment of the ECG. This problem has been addressed in different ways. For example, employing a time-varying Q factor of the notch filter [8, 9] or using tracking algorithm as Kalman filter and recurrent least square estimation [10, 11, 12].

The methodologies described so far are part of the typical preprocessing steps of ECG signals; they are clear examples of non-blind SS because they use information about the sources involved in the ECG, such as temporal location of beats or frequency bands. However, such techniques are not robust enough to provide reliable estimates in more complex applications like detecting fetal ECG from abdominal ECG recordings (fig. 1.1) or detecting atrial activity from electrograms during atrial fibrillation (see sec. 6). In this context, adding further information such as the characterization of the statistical properties of the sources can play an important role in the separation task.

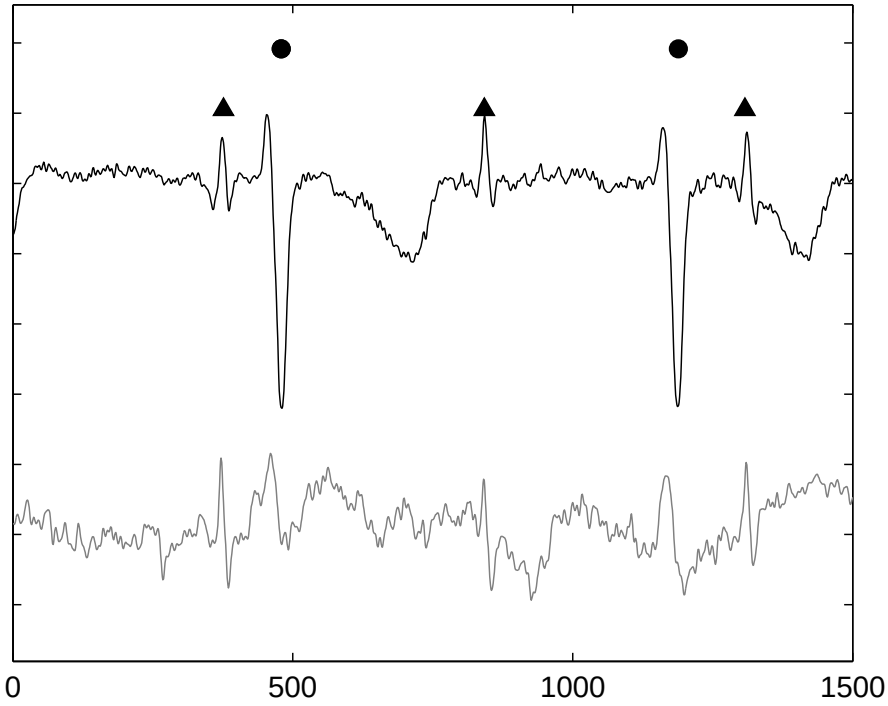

Figure 1.1: Examples of 2-lead abdominal ECG. Circles and triangles indicate the mother and the fetal beat locations respectively.

One of the most challenging application involving ECG recordings is the separation of the fetal ECG from the maternal ECG in non-invasive abdominal ECG recordings. The extraction of the fetal ECG is important for the evaluation of the hear rate variability of the fetus, *i.e.*, an important factor to diagnose its wellbeing [13, 14, 15, 16].

Such measurements contain both the maternal and fetal ECG, and all the noisy sources described above (fig. 1.1). Also, the signal-to-noise ratio is commonly low due to muscular contraction of the mother, movement of the fetus and the small amplitude of the fetal QRS complex.

BSS technique are not a suitable tool for the separation of sources because of the low number of leads normally employed in clinical practice. Information about beat correlation and noise uncorrelation between leads, temporal location of beats and accelerometer signals (for muscular contraction) are typically used to perform the separation.

In this regard, different algorithms have been proposed to separate the maternal ECG from the fetal ECG. Of note, Kalman filters employing the state model proposed by Mc Sharry *et al.* [17] are becoming popular because of their good performance [18, 19, 20]. Such state model describes the ECG waves using a dynamical model and a composition of Gaussian functions. This model requires the location of the maternal beats and the performances are highly influenced by misdetected beats. Recently, this framework was also used for ECG denoising [21, 22].

Another important fetal and maternal ECG separation framework was proposed by Martens *el al.* [23]. Their algorithm uses a combination of blind and non-blind SS techniques for a multi lead-based detection of the fetal beats. In particular, after prepro-

cessing of each recordings, the maternal activity is detected using PCA that exploits the large inter-channel correlation of the ECG components and the small inter-channel correlation of the noise. This information is subsequently used to reduce the maternal activity by means of the template-matching-substraction method (see sec. 1.2.3).

Non-blind SS methods have brought significant results even in the separation of the ventricular and atrial activity on signals collected during episodes of atrial fibrillation (AF). Indeed, standard ECG recordings or electrograms, *i.e.*, signals collected directly within the atria chambers, are typically employed to determine atria-related features (see sec. 1.3) for the risk stratification of subjects affected by AF. However, such recordings are corrupted by the ventricular activity that can alter significantly the interpretation of the features extracted. The separation of the two sources is more challenging in this situation because, during AF, the morphology of the ventricular activity changes quickly over time. When these changes are not tracked well enough, high power residues of ventricular activity are left on the signal [24, 25].

In this context, one of the most effective techniques for estimating the ventricular activity is the template matching and subtraction (see sec. 1.2.3). Such method builds an estimate of the source by averaging a set of ventricular activities. It requires the stationarity of the morphology of the source, a criterion which is not met when analyzing signals collected in AF.

1.2.2 SOURCE MODELING

Mathematical modeling permits to describe complex systems employing mathematical language and concepts. In particular, source modeling defines each sources mathematically and/or probabilistically. When they are dependent on specific parameters, they are called parametric models. Such parametric source models reduce the dimensionality of the problem, *i.e.*, number of samples vs a few parameters, and, depending on the application, can aid to infer new knowledge about the analyzed phenomenon.

Excluding high controlled experimental protocols and environments, real measurements normally contain more than one source. For instance, the electrical activity measured on the skin is the expression of million of cells that have been filtered by the human tissue and the recording instruments. The mixing rule is thus a part of the modeling procedure and it must be chosen carefully.

Furthermore, the use of models in NBSS task permits to increase the reliability of the estimate and to provide measures of similarity, *i.e.*, how distant the estimate is from the model.

In this section, the models employed in this thesis will be briefly discussed.

1.2.2.1 SOURCES LINEARLY MERGED

The most used mixing rule is the linear one. Such rule permits to model several biological signals because, normally, they are the results of a series of chemical phenomena that generate measurable electrical activities in which the assumption of superposition holds.

Let's start with linear dynamical models. The general form of linear dynamical model is

$$\mathbf{z}_k = \sum_{i=1}^{p_{AR}} \mathbf{A}_i \mathbf{z}_{k-i} + \sum_{i=0}^{p_X} \mathbf{B}_i \mathbf{u}_{k-i} + \sum_{i=0}^{p_{MA}} \mathbf{C}_{k-i} \mathbf{w}_{k-i} \tag{1.1}$$

Previous eq. (1.1) establishes a relationship between three components; they are called: i) the *autoregressive* (AR) part; ii) the *exogenous* (X) part; and iii) the *moving average* (MA) part.

Another important class of mixing rule is composed by a linear combination of two kind of sources: i) transient sources; and ii) continuous sources. The mixed output could be as follow

$$\mathbf{z} = \mathbf{A}_t \mathbf{s}_t + \mathbf{A}_c \mathbf{s}_c + \mathbf{w} \tag{1.2}$$

where $\mathbf{z}$ is the mixed multidimensional vector ($\in \Re^{N_m}$), $\mathbf{s}_t$ models the transient sources ($\in \Re^{N_t}$), $\mathbf{s}_c$ models the continuous sources ($\in \Re^{N_c}$), $\mathbf{A}_t$ and $\mathbf{A}_c$ mix the sources and they are $N_m \times N_t$ and $N_m \times N_c$ matrices, respectively. The model uncertainty is modeled by $\mathbf{w}$.

The difference between a transient source and a continuous one is that, the former lasts just for a relative small period of time whereas the latter is always present. For instance, the voice in a phone call is the transient source whereas the background noise, always present, is the continuous one. Such classification permits, when possible, to handle separately the sources because it is known when those transients are not occurring.

An important subclass of source models in eq. (1.2) is when just a single mixed output is available, *i.e.*, N_m=1, and $\mathbf{A}_t$ and $\mathbf{A}_c$ are unitary matrices; that is expressed as following

$$z_k = \sum_{j=1}^{N_t} s_{j,k}^t + \sum_{i=1}^{N_c} s_{i,k} + w_k \tag{1.3}$$

where z_k is the single output, $s_{j,k}^t$ is the transient source j, $s_{i,k}$ is the continuous source i, k is the time, and w_k has the same meaning of eq. (1.2). Such subclass of source models covers a wide range of situations within biomedical applications. Indeed, most of the measurements collected on a human body refers to electrical potentials. Here, the assumption about the superposition of the electrical potentials holds.

1.2.3 TEMPLATE, MATCHING AND SUBTRACTION

One of the most used and robust methodology in non-blind source separation when: i) a single mixed signal is available; ii) transient sources are statistically independent between each others; and iii) sources are stationary over time; is called template, matching and subtraction (TMS).

This method builds a template by means of an average of realizations of transient sources, producing an improvement of the signal-to-noise ratio (SNR) equal to the square root of the number of averaged signals. In order to take into account temporal changes of the sources, a template is built for each realization employing the average of the closest ones. Typically, an average on 20 realizations is considered reliable enough in biomedical application involving cardiac signals.

In this thesis a recursive estimate of the source has been employed.

$$t_k^{b+1} = t_k^b + \gamma(z_k^{b+1} - t_k^b), \tag{1.4}$$

where b is the realization index, k is the time, t_k^b the value of the template at realization b, z_k^{b+1} is the value of the single mixed signal at realization $b+1$ and γ is a constant. The value of γ is set in function of the equivalent number of realizations considered in the average procedure ($\gamma = 0.1$ corresponds to about 20 realizations). This implementation permits to have a much more compact code and to consider only the current realization, however, it requires the first template t_k^0, normally estimated as the average of few realizations (for instance the first 20 realizations). The computational cost of this filter is not different from the averaging procedure.

It is worth noting that the expected value of t_k^b, following the definition of eq. (1.4), is equivalent to that of $z^b(n)$ and so, the expected value of the residue

$$r_k^b = z_k^b - t_k^b \tag{1.5}$$

is equal to zero. This result means that a baseline misalignment could lead to add an offset in the estimate of the source. In order to reduce the effects of such jumps on the boundaries of the window considered, each realization z_k^b is multiplied by a smooth function with compact support, such as a trapezoidal window.

In biomedical signal processing, TMS is broadly applied in source separation even when more than one signal is available. Indeed, techniques like PCA or ICA cannot be applied when the number of channels is too small to ensure robustness in the source estimate.

1.3 INTRODUCTION ON FEATURE EXTRACTION

Feature extraction (FE) is a part of the data processing and analysis related to the study and the research of parameters that are able to concentrate information. Therefore, FE permits to reduce the dimensionality of the problem from an high value, typically the number of samples of the measurements, to a lower one composed by a few and most representative parameters.

Such features are normally categorized depending on the domain where they are calculated. The three principal kind of features typically used in biomedical applications are: time, frequency and complexity.

Once a possible feature is proposed, a set of statistical analysis is performed to determine its properties. Typical analysis are: i) robustness to noise; ii) dependency on the number of samples; and iii) possible correlation with other parameters. In addi-

tion, in biomedical applications, it is also necessary to study the intra/inter-subject variability, the discriminative power between control group and pathological one and the predictive power.

In conclusion, FE represents a way to describe and characterize the main properties of a phenomenon employing a small number of parameters.

In this chapter, the main features collected on signals related with the heart, *e.g.*, electrograms, electrocardiograms, inter-time beat series, etc., will be described.

1.3.1 TIME-BASED FEATURES

Time-based features are extracted in the time domain.

Typical time-based features are average, standard deviation, mean power, mean square error (MSE), root mean square (RMS) and rates (or slopes) of increasing and decreasing trends.

The most important time-based features extracted from the ECG are time intervals [26]. Indeed, time intervals have proven to determine whether a subject has some cardiac disorders or does not. Typical time intervals computed on single beats are PR interval, QRS and QT interval, and RR or NN intervals on series of beats.

PR interval reflects the amount of time to have the atria completely depolarized and the conduction delay of the atrioventricular node (see chap. 6). It is computed as the time distance between the onset of the P wave and the onset of the QRS complex. QRS is the time for the depolarization of the ventricles and it is determined as the time interval between Q and S. Finally, the QT interval, *i.e.*, the amount of time between Q and the end of the T-wave, is linked with the duration of the repolarization phase of the ventricles.

The RR interval measures the time distance between two consecutive beats. Such quantity can be computed beat-to-beat and it has proven to be related with the functionality of the autonomic nervous system. The NN interval is the same of RR but considering only beats labeled as normal, *i.e.*, triggered by the sinus node and following normal conduction paths.

1.3.1.1 TIME-BASED FEATURES DETERMINED ON BEATS

In a normal ECG beat, the P wave represents the depolarization phase of the atria (see sec. 6.2). However, the electrical activity measured on the thorax is relative little (in amplitude) compared with that of the ventricles. Therefore, an average P wave is usually computed for increasing the signal-to-noise ratio. Typically, algorithms based on cross-correlation (CC) identifies those P waves that share similar shapes (*e.g.*, $CC > 0.90$ or $CC > 0.95$) and builds an average P wave for each lead. Once the average P wave is computed for each lead, features like average and standard deviation of quantities as amplitude, power and duration of P waves are normally computed as biomarkers related with the risk of developing an episode of AF [27, 28, 29, 30]. For example, a larger P wave duration was found in subjects with history of AF with respect to that in healthy individuals.

However, the computation of these features on the average P wave still presents numerous challenges. Indeed, the P wave can have different shapes, *e.g.*, monophasic, biphasic, double notched, etc., depending on the lead considered and the pathological status of the subject. Censi *et al.* [31] have addressed such issue modeling the P wave as a sum of Gaussian functions and computing the features directly on the model.

The repolarization phase of the ventricles is encoded on the ECG by the T-wave. In particular, such wave arises because of different transmembrane action potentials (TMP) among the myocytes of the ventricles: the so-called spatial heterogeneity of the ventricular repolarization (SHVR). Since lethal arrhythmias are mainly associated with a high SHVR, biomarkers able to capture the degree of heterogeneity have proven to be fundamental in risk stratification. QT intervals is one of the most powerful time-based features able to characterize the heterogeneity of the repolarization phase of the ventricles directly from the ECG (see sec. 6.3). However, a correct definition of the QT interval is difficult to achieve, it depends on the specific algorithm implementation and it often requires the inspection of an expert clinician [32]. It is worth noting that 10 ms (a very little quantity) of increase in the QT interval is retained to be enough for developing ventricular arrhythmias [33].

In addition, QT intervals depend both on the heart rate, *i.e.*, intra-subject variability, and on the basal level of the subject, *i.e.*, inter-subject variability. Therefore, in order to reduce the dependence of the QT interval on the heart rate, correction formulas are typically employed [34, 35, 36, 37]. Such formulas try to make the QT interval linearly uncorrelated with the heart rate but they can interfere with the clinical interpretation [38].

Another important biomarker related to the heterogeneity of repolarization, is the T peak-to-end interval (TpTe) [39]. It is measured as the difference between the end of the T-wave and its maximum peak. This measure reflects differences in the time for completion of repolarization at different regions in the ventricle. However, a reliable detection of both peak and end of the T-wave is still difficult to achieve. Even in this case, Gaussian models can be employed for modeling the T-wave and estimating such points [40].

These features are dependent on the definition of specific points on the ECG that are highly influenced by noise. The problem has been addressed proposing features less dependent on the position of such points. Biomarkers such as T-wave amplitude variability (TAV) [41], *i.e.*, a measure of the average maximum variability of the amplitude of the T-wave, and power percentage of the PCA [42] are related with the power of the T-wave. Being the end of the T-wave located on the isoelectric line, little changes in its location does not lead to a significant change in the computation of the power.

Even if all the biomarkers discussed so far are related with the physiology, they are just "measures" on the ECG. A physiological interpretation is difficult to achieve because a link between the measure and real physiological quantities misses. In such context, a new measure of the heterogeneity has been recently introduced by Sassi and Mainardi [43]: the $\mathcal{V}$-index. This new biomarker is based on two models. The first one links the TMP of the cardiac cells with the ECG [44] and the second one provides a way to model the time instant of repolarization for those cells. $\mathcal{V}$-index is still being

validated; however, it has already proven to be sensitive as much as the QT interval to several pathological conditions (see chap. 4).

1.3.1.2 TIME-BASED FEATURES DETERMINED ON RR SERIES

The RR series contains the intervals between successive beats. In brief, it shows the variability of the cardiac cycle over time.

During AF, measures as mean and standard deviation (SDNN) are normally computed on sliding windows. Since the heart rate is higher, a low average and a high standard deviation of the RR series are typically observed. In addition, drug-induced alterations can modify the regulation of the ANS and thus, the spectral components of the RR series change [45].

Other measures are *root mean square of successive differences* (RMSSD), *standard deviation of successive differences* (SDSD) and proportion of pairs of adjacent RR (or NN) intervals that differ more than a prefixed time threshold (pNNXX where XX is the time). Such measures are capable to assess the variability of the cardiac cycle [46, 47].

A new time-based feature computable on RR series is called *Phase-Rectified Signal Averaging* (PRSA) [48]. PRSA is a methodology capable of extracting quasi-periodic oscillations out of noisy and non-stationary signals. It provides two measures that quantify the average cardiac acceleration (AC) and deceleration (DC) capacity. AC and DC are linked to the asymmetries between the rates of growth and decrease and they are capable of discriminating between different pathological conditions [49, 50, 51, 52] (see chap. 5 for further details).

1.3.2 FREQUENCY-BASED FEATURES

Frequency-based features are determined in the frequency domain. Typically, after Fourier Transform (FT), features like frequency peak and power in specific frequency bands are determined from the spectrum. Moreover, other characteristics as coupling, causality and bispectrum are computed in the frequency domain [53, 54, 55].

Many application have been developed exploiting frequency-based features to characterize cardiac signals. The two main ones are related to the risk assessment of atrial fibrillation [56, 57, 58, 59] and the evaluation of the sympathovagal balance [60, 61, 62].

Atrial fibrillation is characterized by repetitive and disorganized waves propagation through the atrial tissue. However, this propagation has got a an important characteristic: it has a quasi-periodic rhythm typically from 3 to 15 Hz. The frequency peak is called dominant frequency and it varies from region to region along the atrial surface. This feature is widely employed to determine the best location for the ablation treatment (see chap. 6.2).

The interaction of the ANS on the regulation of the heart rate, that leads to the so-called heart rate variability, is typically assessed by analyzing the RR series in its spectral components. Indeed, such interactions are delimited in different frequency bands of the RR series. Spectral analysis can thus provide useful information on the autonomic regulation evaluating the proportion of the signal power in such frequency bands.

1.3.3 COMPLEXITY-BASED FEATURES

Complexity features measure the level of *complexity* or *organization* on a series of values. However, the definition of *complexity* as well as of *organization* is arbitrary.

A large number of possible definitions has been given during the last decades. The most important ones applied to biomedical signals are Shannon Entropy (SE), Conditional Entropy (CE), Approximate Entropy (ApEn) and Sample Entropy (SampEn). Many other definitions are present in the literature.

These features have proven to be highly sensitive to different pathological conditions, when applied on RR series. For instance, atrial fibrillation episodes can be detected analyzing the complexity of the RR series. Indeed, prior the onset of the fibrillation, the complexity (measured by using different definitions) increases [63, 64, 65].

Other examples are coronary disease [66, 67, 68] and myocardial infarction [69, 70, 71, 72]

2

SOURCE SEPARATION BY MODULATED TEMPLATE, MATCHING AND SUBTRACTION

This chapter describes the formalization of a new methodology for source separation employing the non-blind paradigm. The modeling of sources, algorithm, synthetic validation, real cases and experimental results will be presented. Since the new method is based on mathematical optimization, a brief section about the optimization algorithm exploited has been included.

2.1 PARTICLE SWARM OPTIMIZATION

Particle swarm optimization (PSO) is an iterative algorithm able to solve optimization problem. Originally developed for the study of social behaviors of swarms by means of numerical simulations, it was subsequently employed in the field of mathematical optimization. Nowadays it is one of the most used algorithm for optimization tasks in high dimensional spaces and with noisy functions (hereafter called fitness function).

The main advantage of PSO/MPSO is that it does not require the computation of the gradient of the function to optimize. This property means that problems in which the gradient cannot be easily estimated, for example because of its high computational cost or when the function is not differentiable, can be solved by this algorithm.

PSO uses a set of N_p possible candidate solutions, called particles, that move in the space of the parameters in accord with the function to optimize. It is classified as a cooperative algorithm. Indeed, each particle shares information about its current and best position achieved, *i.e.*, solutions of the problem, with the other ones. Such information are employed to build an heuristic rule of movement.

Formally, each particle x_i is an n-dimensional vector, *i.e.*, $x_i \in \Re^n$, and represents a possible solution of the problem. The movement of each particle is performed employ-

ing three different terms: i) inertia; ii) own best solution; and iii) global best solution. Specifically, movement rule is defined as

$$x_i(k+1) = x_i(k) + v_i(k) \tag{2.1}$$

where i is the particle index, k is the iteration (called "epoch") and $v_i(k)$ is the "velocity". Such velocity $v_i(k)$ is defined as

$$v_i(k+1) = \lambda_1 v_i(k) + \lambda_2(G_i(k) - x_i(k)) + \lambda_3(G_{all}(k) - x_i(k)) \tag{2.2}$$

in which λ_1, λ_2 and λ_3 are parameters of the algorithm to be set in advance. In particular, λ_1 is the inertia parameter whereas λ_2 and λ_3 are respectively the coefficient of own best solution and global best solution terms, $G_i(k)$ is the best solution achieved by the particle i and $G_{all}(k)$ represents the best solution of the whole swarm. The values of $G_i(k)$ and $G_{all}(k)$ are updated when the solution improves.

Because PSO is based on such heuristic rule and its final solution depends on the initial particle position, its convergence is not guaranteed.

In order to reduce these issues, a multi-initialization procedure based on N_{sw} concurrent swarms is normally employed [73, 74, 75]. In this work an extension of PSO termed Multi-swarm Particle Swarm Optimization (MPSO) [76] has been employed. In MPSO, the search space is further enlarged by exchanging particles between swarms after a fixed number of iterations (the worst solutions are traded for the best ones of another swarm). The topology of the set of swarms, the number of particle exchanged across them and the number of iterations before swaps of particles play a fundamental role for the convergence time and they depend on the problem to resolve. In general, if the exchange is done too early, the convergence time increases and on the contrary, if done after too many iterations, the risk of falling into local sub-optimum increases.

Summarizing, at each epoch, the function is evaluated for each particle and optimal values G_i and G_{all} are updated whenever solutions are improved. Then, particles are moved employing eq. (2.1) and eq. (2.2). After a predefined number of iterations a few particles among the worst ones of a swarm are exchanged with those of the next one, according to the topology. Initialization of swarms is made either randomly in the space or using some prior knowledge about the specific problem to solve. The algorithm stops either the maximum number of epoch or the minimum tolerance is reached.

2.2 SOURCES MODELING

In this section, we limited our methodology to signals that can be considered as a sum of multiple sources. Therefore, sources have been linearly merged as explained into sec. 1.2.2.1 and modeled as stationary processes.

First, the continuous sources were modeled as colored Gaussian noises in order to capture temporal relationships. The well-known autoregressive (AR) model is employed as follows

$$s_i(k) = \sum_{j=1}^{p} a_j s_i(k-j) + \epsilon_i(k) \tag{2.3}$$

where i is the i^{th} source, p is the order of the model, a_j are the coefficients of the model and $\epsilon_i(k)$ is a white Gaussian noise.

Second, transient sources were modeled with the following statistical properties

$$E[s_i^t(k)] = \bar{s}_i^t(k) \tag{2.4}$$
$$E[(s_i^t(k) - \bar{s}_i^t(k))^2] = \sigma^2_{s_i^t}(k) \tag{2.5}$$
$$E[(s_i^t(k) - \bar{s}_i^t(k)) \times (s_j^t(k) - \bar{s}_j^t(k))] = 0 \tag{2.6}$$
$$E[(s_i^t(k) - \bar{s}_i^t(k)) \times (s_i^t(j) - \bar{s}_i^t(j))] = 0 \tag{2.7}$$

Equation (2.7) defines the expected value $\bar{s}_i^t(k)$ of the source s_i^t at each time k, its variability $\sigma^2_{s_i^t}(k)$, the statistical independence between sources and between difference time lags.

Finally, the error $w(k)$ was modeled as a white zero-mean Gaussian noise; statistical properties were

$$E[w(k)] = 0 \tag{2.8}$$
$$E[w(k)w(j)] = \sigma_w^2 \delta(k-j) \tag{2.9}$$

where δ is the Kronecker delta function.

2.3 MODULATED TEMPLATE, MATCHING AND SUBTRACTION: A NOVEL ALGORITHM

A new algorithm suitable to separate transient sources from a single mixed signal is presented. The main idea is to treat one transient source at a time and to separate it from the remaining part, *i.e.*, background, employing the prior information provided in sec. 2.2.

Considering the transient source s_i^t and given the time position of each realization of the transient source $p(b)$ (b represents the index of the source realization), a template is built by classical TMS approach. Hence, for each realization, a template $TMS_i^b(k)$ (column vector of N_w samples) is modulated by a weighting matrix $\mathbf{W}$. The modulated template is then

$$mTMS_i^b(k) = \mathbf{W} TMS_i^b(k) \tag{2.10}$$

where $\mathbf{W}$ is a $N_w \times N_w$ diagonal matrix; the notation is the same of sec. 2.2.

The modulation is performed in such a way to have the mean power and mean power of the derivative of the residue,

$$r(k) = z(k) - mTMS_i^b(k), \tag{2.11}$$

similar to those of the background (in which the source $s_i^t(k)$ is not present).

The weighting matrix $\mathbf{W}$ is obtained by maximizing, via MPSO, the fitness function

$$J(\mathbf{W}) = \alpha J_1(\mathbf{W}) + \beta J_2(\mathbf{W}) + \delta J_3(\mathbf{W}) \tag{2.12}$$

where α, β and δ are the weight of each goal (see sec. 2.5 for determining them).

The first term in the fitness function of eq. (2.12)

$$J_1 = j(\rho_1), \quad \rho_1 = P_r/P_{bkg} \tag{2.13}$$

quantifies the similarity between the power of the residual signal and the power of the background. P_r and P_{bkg} are the mean power of the residue and the background, respectively. The function $j(\rho)$ is defined as

$$j(\rho) = \begin{cases} 1, & \rho \leqslant 1 \\ -(\rho-1)^3, & \rho > 1. \end{cases} \tag{2.14}$$

The third power of the polynomial in eq. (2.14) permits to improve each goal in balanced way (see 2.5). The mean power of the discrete signal $x = [x(1), ..., x(N)]$ is as follow

$$P_x = \frac{1}{N}\sum_{k=1}^{N} x(k)^2 \tag{2.15}$$

where $N = N_w$ is the number of samples.

The second term J_2 quantifies the discrepancy in the derivatives of the residue $r(k)$ and that of the background. Similarly to eq. (2.13), it is defined as

$$J_2 = j(\rho_2), \quad \rho_2 = P_{D_r}/P_{D_{bkg}} \tag{2.16}$$

where D_r and D_{bkg} are the derivative of the residue and the background, respectively, and P_{D_r} and $P_{D_{bkg}}$ their powers. The first derivative of a discrete signal x was approximated by

$$D_x(k) = x(k+1) - x(k) \tag{2.17}$$

where $k = [1, \ldots, N-1]$.

Finally, J_3 is used to constrain $mTMS_i^b(k)$ to remain similar to the original template $TMS_i^b(k)$:

$$J_3 = j(\rho_3) - 1, \quad \rho_3 = d(mTMS_i^b(k), TMS_i^b(k))/\theta \tag{2.18}$$

The metric

$$d(x,y) = \frac{1}{\pi}\arccos\left(\frac{x^T y}{\|x\|\|y\|}\right) \tag{2.19}$$

measures the distance between the two discrete signals x and y. $d(x,y)$ is minimum when x and y are parallel. An alternative metric could have been the mean square error of the difference signal, but the definition in eq. (2.19) was preferred as it leads to a bounded quantity. The threshold θ defines the maximum acceptable distance between $TMS_i^b(k)$ and $mTMS_i^b(k)$.

It is worth noting that the quantity J of eq. (2.12) is superiorly bounded to $\alpha + \beta$.

2.4 SYNTHETIC ATRIAL ELECTROGRAM GENERATOR

Since several applications could exploit such algorithm, we concentrated our efforts on signals recorded on the surface of the atria chambers, *i.e.*, atrial electrograms (AEGs). In order to evaluate the performance of the method, we proposed a set of equations [77] to model AEGs in different conditions, *e.g.*, sinus rhythm (SR), atrial flutter (AFL) and AF. The performance of the new algorithm was tested in the most difficult situation, *i.e.*, AF [24, 78].

2.4.1 ATRIAL ELECTROGRAM SOURCE MODEL

Let's start defining an atrial electrogram (AEG) as following

$$AEG(t) = AA(t) + VA(t) \tag{2.20}$$

where $AA(t)$ is the electrical activity generated only by the atrial cells and $VA(t)$ is the ventricular activity that interferes with the measurements.

The atrial activity AA can be rewritten using two subcomponents

$$AA(t) = AA_{far}(t) + AA_{near}(t) \tag{2.21}$$

where $AA_{far}(t)$ and $AA_{near}(t)$ represent the far field and near field effects. Such activities correspond to electrical waves that travel far and near to the electrodes, respectively. Although a clear distinction between far and near field effects does not exist, this has been previously used as a reasonable approximation [79].

2.4.2 ATRIAL ACTIVITY MODEL

2.4.2.1 FAR FIELD EFFECT AND MEASURING NOISE

During sinus rhythm, atrial flutter and AF, measurement noise can be modeled as a colored noise. Moreover, during AF, the far field effects become much more powerful but still remaining quite stationary, in the statistical sense, over time and making the measurement noise neglectable. Indeed, the high number of far sources produces a

noisy effect added to the near field activity. The autoregressive model (AR) is suitable for representing these electrical sources.

AA_{far} is modeled by means of an autoregressive model

$$AA_{far}(t) = \sum_{k=1}^{p} c_k AA_{far}(t-k) + w(t) \tag{2.22}$$

The model parameters (c_k and p) can be derived by fitting a set of real AEG signals to the AR model. To do that, we consider segments of AEG between two atrial depolarizations, *i.e.*, the AA_{far}. Each segment is fitted by an AR model of order p, with p ranging from 1 to 40. A common model is determined by averaging the c_k coefficients among all the models fitted. The model order p is selected using the Akaike information criterion (AIC).

2.4.2.2 MORPHOLOGY OF NEAR FIELD ACTIVITY

The near field effect AA_{near} is modeled using the formula of the electrical dipole moving along a line (not necessarily straight) [80]. The potential generated by this dipole in a uniform infinite medium is

$$\phi(t) = \frac{\mathbf{p} \cdot \mathbf{u_d}}{4\pi\sigma \|\mathbf{r}(t)\|^2} \tag{2.23}$$

where $\mathbf{p}$ is the dipole moment, $\mathbf{u_d}$ is the unit vector directed from the source point to the field point, σ is the electrical conductivity and $\mathbf{r}(t)$ is the vector directed from the source point to the field point vector, pointing the evaluation point.

Furthermore, multiple near field sources can be approximated by a summation of N dipoles moving nearby the measurement point. The near field effect AA_{near} becomes

$$AA_{near}(t) = \sum_{k=1}^{N} \phi_k(t) \tag{2.24}$$

where $\phi_k(t)$ is the electrical potential generated by the $k-$th dipole that travels along a specific direction and N is the total number of dipoles.

2.4.2.3 POSITION OF NEAR FIELD ACTIVITY

In normal SR, the time location of the near field atrial activity always precedes the ventricular one. Therefore atrial and ventricular rate are the same. In such situation, we first set the time location of the ventricular activity, being more models available for this case, and then, the near field activity was shifted backward of 150 ms (see sec. 2.4.3.2).

Due to the lack of relevant models of AF, the position of the near field activity was considered temporally uncorrelated. The position of AA_{near} was selected assuming that atrial depolarizations' front arrives to the electrodes according to a gamma distribution $AA_{near} \sim \Gamma(k, \theta)$, whose probability density function approximates the exponential one (for small values of k) or the normal distribution (for high values of

k). Depending on the rhythm to simulate, different values were used, keeping in mind that $k\theta$ is the mean inter-time beat interval.

2.4.3 VENTRICULAR ACTIVITY MODEL

2.4.3.1 MORPHOLOGY OF VENTRICULAR ACTIVITY

The ventricular activity (VA) is generated by the current dipole described in eq. 2.23. Local variations in VA amplitude and time width are modeled on a beat-to-beat basis. Since the ventricular activity is a far field effect, the electrical potential can be modeled by a single dipole.

2.4.3.2 POSITION OF VENTRICULAR ACTIVITY

Different models exist to generate sequences of RR intervals.

In normal SR, an AR model is adequate to model the RR series [81].

In AF, a realistic sequence of RR intervals can be generated using an atrioventricular node model as described by Lian et al. [82] or Corino *et al.* [83]. The latter is used in this work and is characterized by parameters to describe the arrival rate of atrial impulses, the probability of an impulse choosing either one of the two atrioventricular nodal pathways, the refractory periods of these pathways, and the prolongation of the refractory periods. The parameters of the model are chosen to generate RR series with different mean heart rate (HR) (90, 120 and 150 bpm). In particular, the mean arrival rate of AF impulses is varied in the range $5-8$ Hz, the refractory period of the slow and fast pathways in the range $0.1-0.4$ s and $0.2-0.7$ s respectively, with a maximal prolongation of 0.2 s. The probability of an impulse choosing either one of the two paths ranges between $0.2-1$.

2.4.4 VALIDATION OF THE GENERATOR

In this section, different rhythms are simulated: i) SR; ii) AFL; iii) AF. Figure 2.1 shows the AEGs for the different simulated rhythms. It is worth noting that in all examples the amplitude of the ventricular activity is much smaller than that of the atrial one. However, this ratio can be changed and the ventricular activity can be bigger, for example when simulating signals recorded closer to the ventricles.

2.4.4.1 SINUS RHYTHM

During SR, the internal surface of the atrium chambers is crossed by a wave that can be approximated by a plane wave. We simulated this situations using a set of parallel dipoles (equispaced) that, fixed the direction, traveled along a straight line. The simulation could be optimized taking into account the symmetric properties of the dipole potential, in fact, the electrical component transversal to the direction becomes null. Figure 2.1a shows the simulated AEG during SR.

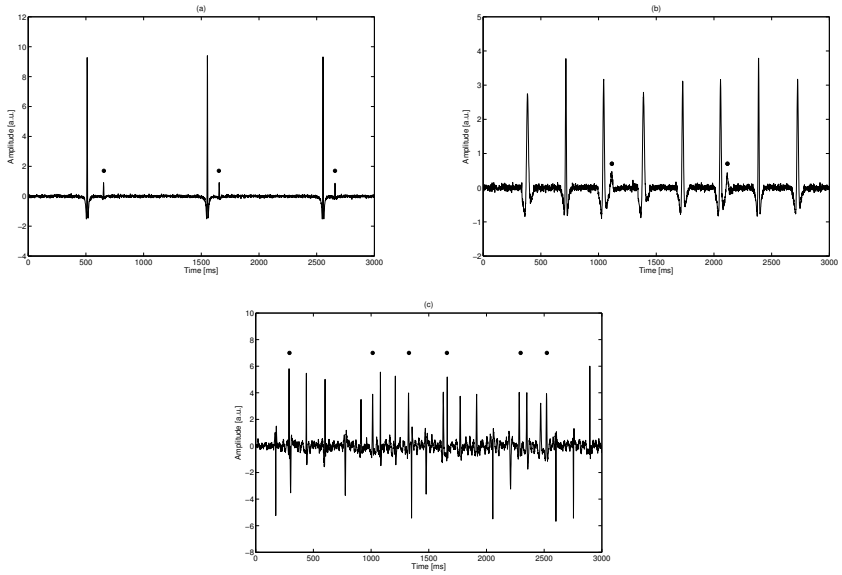

Figure 2.1: Examples of AEG during SR, 3 : 1 AFL and type-II AF. The circles represent the ventricular activity position. It is worth noting that in AF the ventricular activity cannot be visually identified, as it can during SR and AFL.

2.4.4.2 ATRIAL FLUTTER

After model identification of the position of the ventricular activity, we defined the flutter rate as the mean heart rate multiplied by 2, 3 and 4. Figure 2.1b shows the simulated AEG during AFL.

2.4.4.3 ATRIAL FIBRILLATION

In order to mimic different degrees of atrial organization according to the three Wells' classes, the standard deviation of the white Gaussian noise in input to AA_{far} was varied in the range $0.05 - 0.4$ a.u. The position of AA_{near} was selected assuming that atrial depolarizations' front reaches to the electrodes according to a gamma distribution $AA_{near} \sim \Gamma(k, \theta)$. Thus, Wells' type-I was simulated using $k = 255$ and $\theta = 0.56$, Wells' type-II $k = 100$ and $\theta = 1.43$, and Wells' type-III $k = 20$ and $\theta = 7.14$, corresponding to an AF rate of 7 Hz. To have a certain variability in the shape of AA_{near} waves, their morphology was randomly chosen among a set of possible shapes for atrial potentials (see sec. 2.4.5).

2.4.5 SYNTHETIC VALIDATION OF THE ATRIAL ELECTROGRAM GENERATOR

To qualitatively assess the proposed generator, a small database of AEGs during AF was built.

In order to build AA_{near} and VA, a bipolar electrode was placed in the origin of the cartesian axes (2-mm electrodes distance) and two points on a circle around it were considered as the starting and the ending point of the traveling dipole. We discretized

Table 2.1: Mean ± standard deviation of the spectral concentration (SC) and wave-morphology similarity (WMS) for the three AF Wells' classes with 7 Hz dominant frequency.

	SC	WMS
type-I	0.67 ± 0.02	0.78 ± 0.02
type-II	0.48 ± 0.02	0.34 ± 0.02
type-III	0.17 ± 0.01	0.11 ± 0.01

the circle in 30 equispaced points, for a total of 870 possible shapes. In function of the desired Wells' class, we chose the shapes in a subset of the possible ones.

A spectral and morphology analysis was performed to evaluate both the dominant frequency and the regularity of the signal. We computed the spectral concentration [84] and the wave-morphology similarity [85]. In particular, 50 AEGs for each of the Wells' class and dominant frequency were simulated. The recordings had a dominant frequency of 5 Hz, 7 Hz and 9 Hz. The results of each Wells' class and 7 Hz dominant frequency are shown in tab. 2.1.

2.5 OPTIMIZATION PROBLEM FOR TUNING PARAMETERS OF THE MODULATED TMS

The topology of the set of swarms, the number of particle exchanged across them and the number of iterations before swaps of particles play a fundamental role on the convergence time. If the exchange is done too early, the convergence time increases. However, if done after too many iterations, the risk of falling into local maxima increases. In this work, we tried to balance between these two issues. We selected a ring topology with 10 swarms of 12 particles each. Swarms were initialized into a hypersphere of center equal to 1. Every 10 iterations, 5 particles were exchanged from a swarm to another.

The stopping criterion was either reaching the maximum number of iterations (1000) or reaching 99.9% of the maximum value of the fitness function, *i.e.*, $\alpha + \beta$, see eq. (2.12).

Regarding the selection of the fitness function used in this work, it was build in eq. (2.12) as a linear combination of sub-functions $J(x) = \sum_{i=1}^{N} \lambda_i J_i(x)$ to solve a multi-goal optimization problem. To avoid having one $J_i(x)$ predominant over the others, we built each of them as in eq. (2.14) with a function that increase more rapidly when the solution is distant from the optimum. In this way the swarms compete and cooperate to reach the optimal solution, *i.e.*, when the values of λ_i are balanced and coherent with the objective of the optimization.

The values of λ_i could be chosen empirically. In this work we preferred to study their influence on the final result before taking a choice. Several values of the parameters α, δ and θ (β was set to 1 in advance with no lack of generality) were tested with the mTMS method on two sets of simulated signals with 60 ventricular activities each.

They were generated as in sec. 2.4 with different organization and HR. For each set of parameters we computed the metric

$$I(\alpha, \delta, \theta) = (C - 1)^2 + NMSE^2, \tag{2.25}$$

which takes into account both the normalized mean square error and the linear correlation C. A large value of C means that the shape of the modulated template is preserved in mTMS, whereas a small value of NMSE forces a larger departure from the TMS template.

To further guide our selection, we also employed a second MPSO algorithm to minimize the metric I, but this time having as variables the parameters α, δ and θ. Their final value jointly minimizes the NMSE and maximizes the linear correlation C. The results obtained were $\alpha = 6.97$, $\delta = 0.99$ and $\theta = 0.43$ which prompted our final choice: $\alpha = 7$, $\delta = 1$ and $\theta = 0.4$.

2.6 SYNTHETIC VALIDATION OF THE MODULATE TMS

The synthetic generator of AEG described in sec. 2.4 has been employed for validating and comparing the modulated TMS with the classical one.

In particular, a set of synthetic signals was built for reproducing the three Wells classes with three different heart rates (70, 90 and 120 bpm). Wells' type-I was simulated using $k = 20$ and $\theta = 10$, Wells' type-II $k = 10$ and $\theta = 14$, and Wells' type-III $k = 1$ and $\theta = 111$, corresponding to an AF rate of 5, 7, and 9 Hz, respectively.

To quantitatively compare the performances of the algorithms, three indexes were employed.

The first one measures the degree of similarity between the AEG and the residue by means of the normalized mean squared error, defined for each beat as

$$NMSE^j = \frac{P^j_{s-r}}{P_s} \tag{2.26}$$

where j indicates the j-th beat, thus P^j_{s-r} is the mean square error between the signal and the residue in a 100 ms window centered in the VA, and P_s is the power of the whole signal s (P is defined as in eq. (2.15)). Obviously, being the actual AA unknown in real data, this index can be used to evaluate the cancellation performance on simulated data only.

The second one evaluates the beat-by-beat amplitude reduction of the peak of VA (VDR) and is defined as

$$VDR = 10 \log_{10} \left(\left| \frac{R^j_s}{R^j_r} \right| \right) \tag{2.27}$$

where j indicates the j-th beat, R^j_s is the j-th peak amplitude of the original AEG in a 100 ms window centered in the VA, and R^j_r is the j-th peak amplitude of the residue (*i.e.*, the amplitude of the residue signal at the same position of the peak on the original

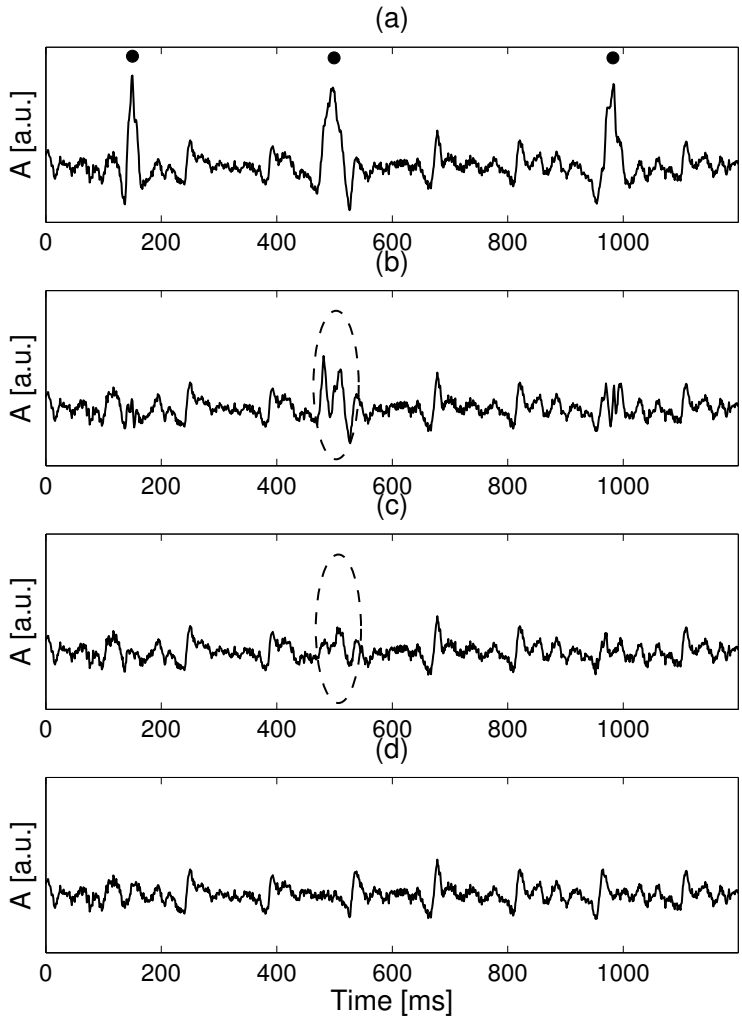

Figure 2.2: Example of cancellation of VA from a simulated AEG. Original AEG (a), where occurrences of VA are identified by black dots. Cancellation obtained by TMS (b) or mTMS (c). Original atrial signal (d). A = amplitude.

AEG). High positive values of VDR will indicate good performance of the algorithm. Values close to zero are associated with poor performance and negative values indicate reduction errors because the peak is larger than before. This index is introduced in [25] and therefore computed here for comparison. However, its value is limited. In fact, it must be noted that if the segment containing VA is set to a value close to zero, the VDR would be very high and thus the performance considered optimal. Luckily, in our approach, J_3 (eq. (2.18)) avoids this extreme possibility. This index can be computed on simulated data as well as on real recordings.

The third index (PP) evaluates whether the power of the residue is inside the standard range of the atrial power range (AP_{95}), evaluated non parametrically, *i.e.*, it is within the 2.5 and 97.5 percentiles of the distribution of the values of AA measured

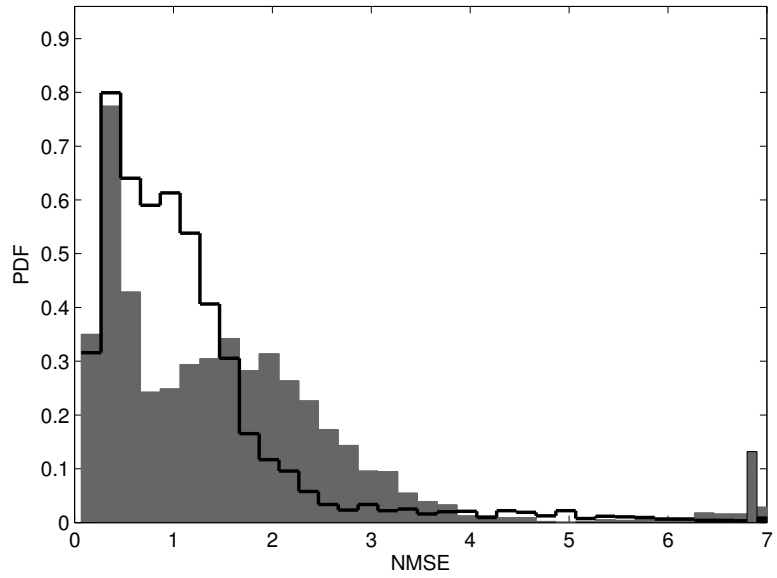

Figure 2.3: Histogram of NMSE obtained after removal of VA from simulated signals, using TMS (grey area) or mTMS (black thick line). The signals were Wells' type-III and heart rate of 120 bpm. PDF = probability density function.

on the same data. PP is computed as the percentage of segments with residual power outside the standard range AP_{95}.

First, the segments containing AA only are divided into 100-ms segments (a new signal segment is defined every ms, and thus, segments overlap), the mean power for each segment computed and the standard range AP_{95} for the specific signal obtained. Then, the power of the residue is computed on the segments containing VA and the PP index is determined. It should be noted that this index can be used for real data too. Obviously, the quality of the estimates for the residual power is limited by the length of the AEGs at disposal.

2.7 REAL DATA VALIDATION OF THE MODULATED TMS

The proposed algorithm was also tested using 11 electrocardiographic bipolar recordings collected in the electrophysiology laboratory of San Paolo Hospital at the University of Milan, from 3 patients undergoing radiofrequency ablation of the pulmonary veins for treatment of AF.

The signals were stored during a standardized electrophysiological procedure, exported and anonymized for subsequent analysis. Bipolar electrograms were recorded for 2 min (sample frequency of 1000 Hz).

This investigation was designed as an observational study and it conforms to the principles outlined in the Declaration of Helsinki; the Research Ethics Board of the San Paolo Hospital of the University of Milan, Italy approved the study protocol. All patients were informed about the procedure and gave their written consent.

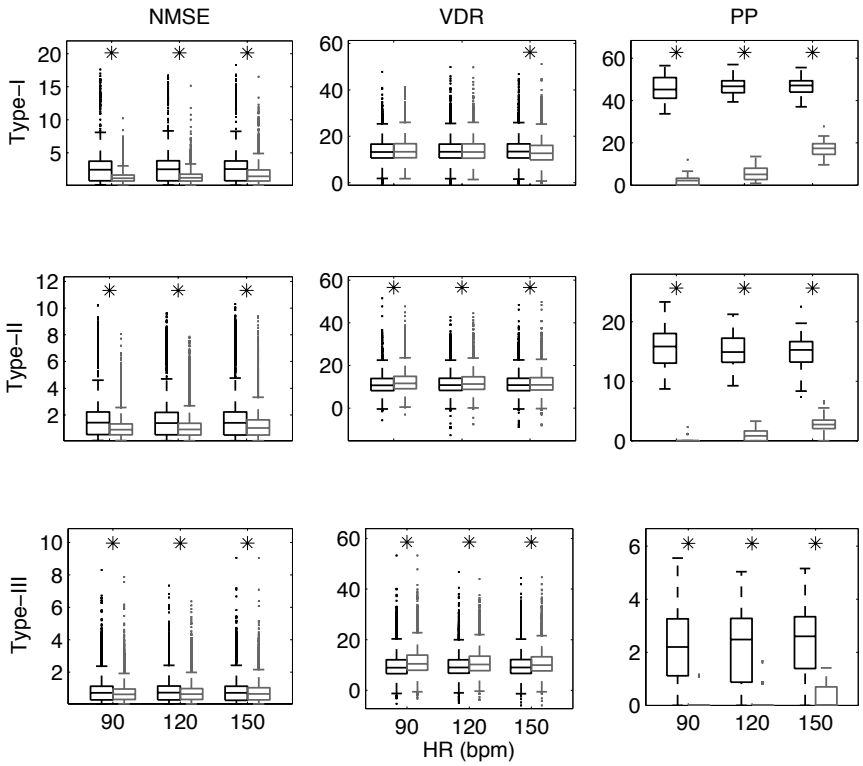

Figure 2.4: Boxplots of the indexes assessing performance using TMS (black) and mTMS (grey). Each row shows results for a different Wells' type, whereas each column shows a different index. Each subplot presents results with increasing HR. It can be noted that NMSE and PP are significantly lower for mTMS and VDR higher. ‡$p < 0.05$, †$p < 0.01$,* $p < 0.001$

2.8 RESULTS

2.8.1 SIMULATED DATA

Figure 2.2 shows the cancellation of VA from a simulated AEG. A clear residual of VA cancellation is still present when TMS is employed (see ellipses in fig. 2.2(b)). Conversely, using mTMS (Fig. 2.2(c)), a lower remainder of VA is observed.

Figure 2.3 shows the histogram of NMSE values obtained on simulated signals from Wells' type-III and HR of 150 bpm. The values of NMSE obtained with mTMS are generally smaller (the histogram is left-shifted in fig. 2.3) and, on average, lower errors are obtained.

These results are confirmed on all the sets. Figure 2.4 shows the results for the Wells' types and HR. In particular, the values of NMSE are always significantly lower, when using mTMS implying that the residual signals are closer to the original ones, leading to more reliable results. The VDR is higher using mTMS, implying a better cancellation. The PP, *i.e.*, the percentage of segments whose residual power is outside the standard range of atrial power AP_{95}, is always lower for mTMS, implying that there are fewer high-power residual segments.

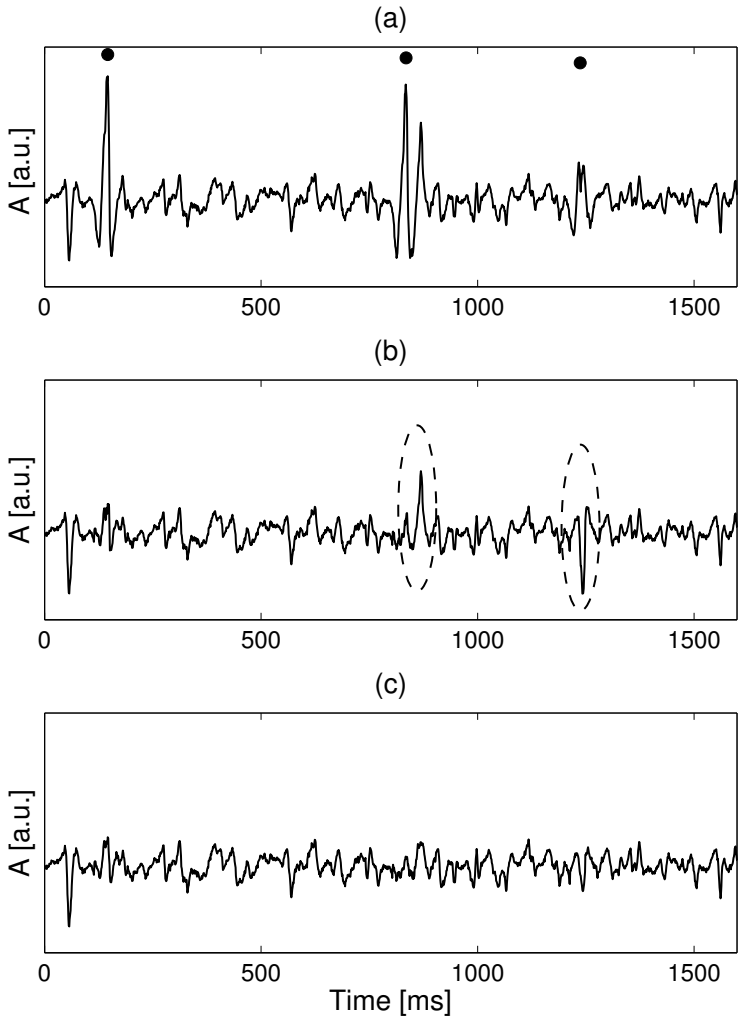

Figure 2.5: Example of VA cancellation of a real endocardial signal recorded in the coronary sinus: (a) original AEG with QRS position (black dots) from the surface ECG, residue obtained after (b) TMS and (c) mTMS cancellation. See text for details.

2.8.2 REAL DATA

Figure 2.5 shows an example of ventricular cancellation on real signals, recorded from the coronary sinus. It can be noted that a high residual is still present when TMS is employed (see ellipses in fig. 2.5(b)), conversely, using mTMS, a lower remainder of VA is observed. The three VA being different from each other (see fig. 2.5(a)), the TMS algorithm fails to completely cancel them, because the actual template is highly dependent on the previous one. On the contrary, the higher flexibility in building the template in the mTMS algorithm provides a better cancellation.

A comparison of VDR computed for TMS and mTMS is shown in tab. 2.2. In all recording sites (CS1-CS5), VDR is significantly higher for the mTMS algorithm. In addition, moving away from the ventricles (from CS1 to CS5) VDR decreases, probably

Table 2.2: Median ($25\% - 75\%$ percentiles) of VDR and PP computed on real AEGs ($\ddagger p < 0.05, \dagger p < 0.01, ^* p < 0.001$)

		TMS	mTMS
VDR	CS1	$6.71(3.24 - 9.88)$	$8.15(4.91 - 11.52)^*$
	CS2	$5.48(2.01 - 9.56)$	$6.82(3.42 - 10.84)^*$
	CS3	$1.44(0.13 - 6.08)$	$2.73(0.29 - 7.52)^*$
	CS4	$0.77(-0.90 - 3.65)$	$1.60(-0.45 - 5.36)^*$
	CS5	$2.34(0.51 - 4.88)$	$3.39(1.02 - 6.34)^*$
PP	CS1	$2.44(0.38 - 3.55)$	$0.38(0.00 - 0.97)^*$
	CS2	$1.65(1.17 - 2.72)$	$0.46(0.00 - 0.78)^*$
	CS3	$1.95(1.15 - 3.55)$	$0.46(0.00 - 0.78)^*$
	CS4	$2.20(1.43 - 2.96)$	$0.48(0.00 - 0.99)^*$
	CS5	$2.54(1.56 - 2.86)$	$0.80(0 - 1.18)^*$

because of the larger distance from the ventricles which implicitly reduces the amplitude of the ventricular complexes and their relevance on the AA. In fact, the amplitude of the VA on the original AEGs (normalized to the background noise) decreases moving from CS1 to CS5 from 3 ± 1 in CS1 to 1.8 ± 0.5 in CS5.

Table 2.2 also shows the atrial power values for TMS and mTMS. A statistically significant reduction in PP can be noted in all recording sites, in particular in CS1 which is the closest to the ventricles.

Value for the NMSE can not be computed on real data, being the true AA unknown.

2.9 CONCLUSION

In this chapter, a new methodology to iteratively separate transient sources has been proposed, discussed and then validated on both synthetic and real data. Also, a generator of synthetic AEGs has been proposed for the first time.

Autoregressive models were used for simulating VA locations in SR and AFL, a specific model for the atrioventricular conduction during AF, a Γ distribution for AA_{near} locations and the dipole equation for generating the wave forms. Tuning the model parameters allowed the generation of synthetic AEGs with properties similar to the real ones.

All the synthetic AEGs were created using a single equivalent dipole. In SR, a planar wave was simulated by placing a set of parallel dipoles along a straight line and employing eq. (2.24). This was reasonable for SR, AFL and type-I AF. For higher disorganized class of AF, it has been shown [79] that localized activity is given by the summation of both near and mid-field effect. In fact, in real data, simple wave forms are not present for Wells' type-II, type-III and type-IV. It is worth noting that we considered only Wells' type-I, type-II and type-III because type-IV is highly disorganized

and the dipole model is not suitable. In such case, the AR model can describe the atrial electrical activity.

Unfortunately, a realistic model of the inter-times among consecutive close-field effects during AF is not available yet. We proposed to use a Γ distribution for simulating them.

The proposed unified approach for simulating AEGs provided reasonable results. Indeed, the SC and WMS increased in function of the Wells' classification, in particular, the values of the latter were in the range of those showed in [85].

In order to test the performance of the new algorithm, a specific application was considered. The separation of VA in AEG is the most important preliminary step for almost all the subsequent analysis of AEG. The beat-to-beat variability in the morphology of the QRS complex might induce the classic TMS method to leave residuals of cancellation with large localized power. To overcome this problem, while constraining the shape of the template not to vary too much from what suggested by TMS, we modulated its shape, via an optimization procedure, so that the power of each AEG interval after separation is constrained to have power levels similar to the nearby atrial activity.

The main findings of this study are: i) the modulation of the TMS template improves the separation during noisy scenario; ii) the separation of VA from AEG during AF has been improved; iii) the performance of the proposed method is largely independent (at least in the range tested) of ventricular rate or AEG organization.

We showed using both synthetic signals and AEGs recorded during routine ablation procedures that the proposed approach is superior to TMS alone. When compared with the results of a previous study addressing the same issue [25], we note that: i) VDR was on average comparable to the values previously reported; ii) mTMS did not alter AEG signal outside the ventricular segment; and iii) mTMS was firstly tested on simulated data which permitted a limited but objective performance evaluation.

This work expands the concept we have recently proposed in [78], *i.e.*, to modulate the TMS template to obtain better VA cancellation. While in [78] a preliminary attempt to solve the problem of TMS poor cancellation has been anticipated, this work formalizes the solution. In particular, we showed that the new proposed strategy to modulate the template and keep the residual power in the range of the expected atrial one, provides good results. We quantified the improvement using NMSE, VDR and PP for the simulated data, and VDR and PP for the real data. A limitation of the study is to rely only on data collected from three patients. However, the extensive analysis made on synthetic signals offered a severe methodological workbench.

Another limit of our approach is that temporal relations among samples are lost. In fact, the element of the diagonal matrix $\mathbf{W}$ are selected independently from each other by MPSO. The problem might become relevant when the residual signal contains localized atrial activity. In fact, in these situations, part of such activity might be inadvertently canceled along with the ventricular one. However, the results of our simulations showed that this problem is of limited importance with the parameters selected in the fitness function.

Finally, in this work we employed MPSO for the selection of the coefficients. Other algorithms could have been used, however the large number of members that compose the particle swarm makes MPSO impressively resilient to the problem of local maxima, in comparison to other global maximization strategies such as simulated annealing [76].

3

MODEL-BASED FEATURE EXTRACTION: CHARACTERIZATION OF THE WAVE PROPAGATION

This chapter describes the formalization of a new index of organization for transient phenomena or wave propagation based on symbolic analysis. It employes both morphological, temporal and organization features to produce an unified parameter to represent the local status of a system.

3.1 SOURCES MODELING

Sources are modeled as in eq. (1.2). A set of measurements N_m is available over time in which both transient and continuous sources are mixed linearly.

3.2 ORGANIZATION DEGREE FOR WAVE PROPAGATION: A NOVEL METRIC

The new parameter aims to characterize the degree of organization of the wave propagation merging the information collected by a set of sensors. Let's give a simple example to introduce the main idea.

Consider a classical problem of weather forecasting in which the air flux in a particular geographic region is employed to determine the probability of raining. Pressure sensors are normally used to convert the velocity of the wind in pressure. However, the pressure is a scalar quantity and so, it does not carry information regarding the direction of the air flux. When employing more than a single pressure sensor, other information as direction of propagation, curvature of the wavefront, etc. becomes available. Such fact permits to conclude that the level of pressure and the order of arrival of the wavefront on a set of sensors can describe the local status of that region, with an accuracy dependent on the number of sensors employed.

Moreover, the evaluation of the randomness of patterns, *i.e.*, pressure, direction, curvature, etc., aids to characterize the phenomenon over time.

In such context, a novel feature, the organization degree (OD), based on morphology, time and regularity/complexity has been proposed for characterizing traveling phenomena [86]. Figure 3.1 shows the scheme for the composition of the feature to study.

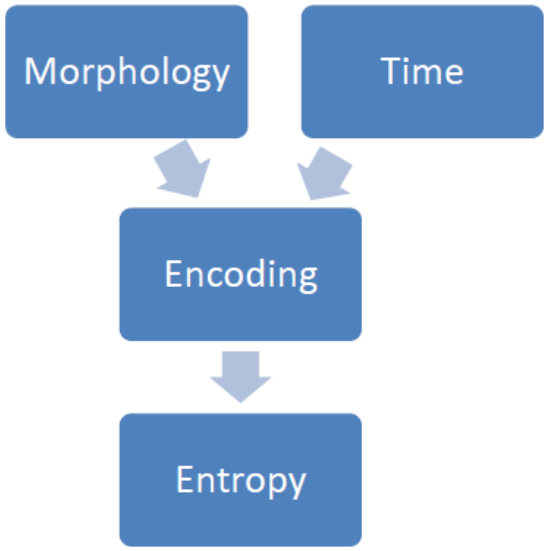

Figure 3.1: Structure of the algorithm for the composition of the new organization index.

First, the morphology of the waves measured by a set of sensors is classified considering a predefined set of classes. To do that, a clustering procedure can be considered to characterize the morphology. Figure 3.2 shows a schema of two possible signals.

Second, the time or the order of arrival of the wave on the sensors plays an important role in the definition of the direction of propagation. A practical way to define such time instant could be the barycenter of the signal when the wave goes through the sensors.

Third, a different symbol is assigned to each morphology and each order of arrival. This step builds a sequence of symbolic words.

Finally, the word sequence can be used to determine the organization or complexity degree. It is worth noting that every symbolic-based parameter from Information Theory can be applied (*e.g.*, Shannon Entropy, Conditional Entropy, etc.).

3.3 APPLICATION OF THE ORGANIZATION DEGREE

In this section, the OD will be implemented, discussed and applied on AEGs during normal sinus rhythm or atrial fibrillation.

AEGs contain wavefronts, *i.e.*, localized atrial activity (LAA), travelling on the atrial surface. The electrodes are capable to measure such local electrical potential.

For this specific application, the new parameter, considering also the order of arrival of the wave on the electrodes, could aid to characterize the organization of the atrial activity and possibly helping physicians to locate the most suitable sites to perform the ablation (see sec. 6.2).

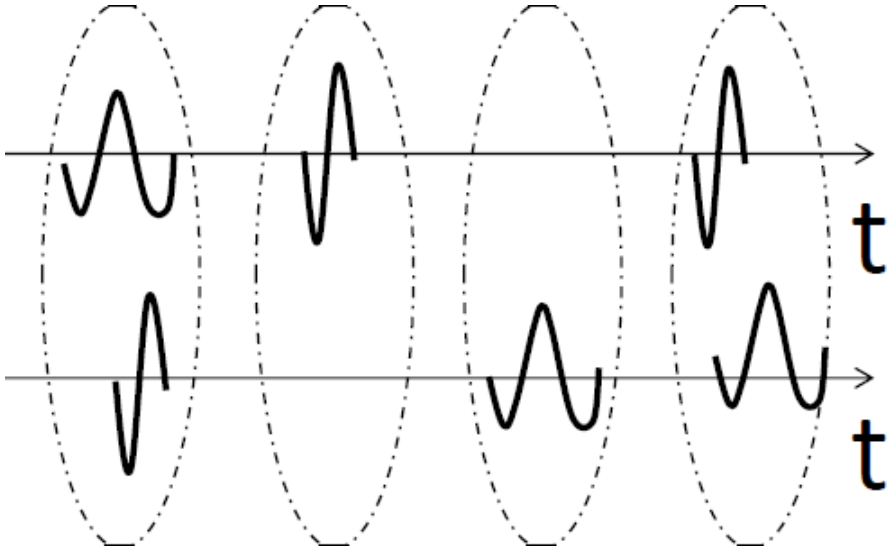

Figure 3.2: Two signals with only transient waves (located in dashed circles).

3.3.1 DEFINITION OF EVENT

In order to build the symbolic word, it was necessary to detect the atrial activity on each electrode (see sec. 3.4.3). Such activity was associated with the triggering of an event (see fig. 3.3). The concept was to consider the atrial activities detected on different electrodes as part of same event. Consequently, when no wavefronts were detected, no events were triggered. All the wavefronts whose their barycenter were within a maximum time τ_E after the first detection, were considered belonging to the same event. In here, τ_E was set to 50 ms. The barycenter of wavefront was called activation time (AT) [85].

3.3.2 MORPHOLOGICAL FEATURE: CLUSTERING PROCEDURE

For each event we defined a window of 90 ms centered on the AT and we built an input matrix containing the waves coming from all the leads. (Thus the size of the input matrix was $90 \times N$ being N the number of detected waves).

Principal component analysis was applied to reduce the dimensionality of the input matrix. We selected a number of principal components (PCs) that covered at least the 90% of the total power. The number of PCs can be either kept fixed or selected independently for each set of electrodes. Here, PCs were selected independently.

We used K-means, an unsupervised learning method [87], for automatically detecting clusters because this algorithm is usually robust and able to generalize quite well. Also, it is not necessary to select a threshold on distances between clusters.

Since the initialization of the centroids was random, we reinforced the procedure repeating the training 10 times and taking into account only the solution that maximized the variance between centroids. The number of clusters was set to 4.

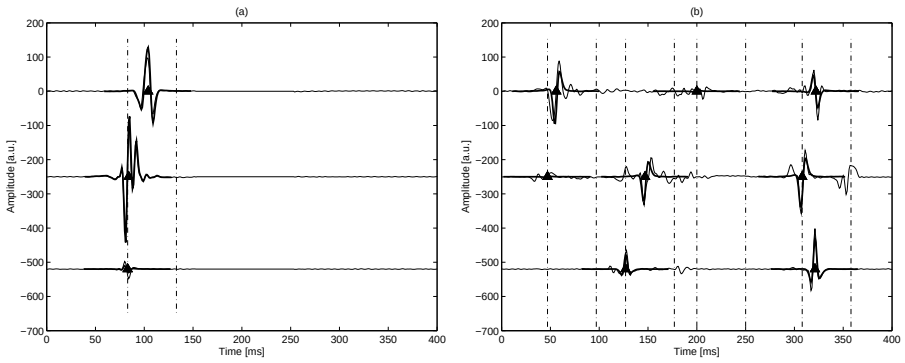

Figure 3.3: Events detected in SR (a) and AF (b). The position of LAA waves is marked with a triangle, while the thick black line is the mean template of the cluster. Each event is bracketed by a 50 ms window (sketched lines).

Figure 3.4 shows the result of the clustering procedure for a subject in AF. It is interesting to notice that the shapes of the waves are grouped in well defined clusters even when using only the first two PCs.

3.3.3 WORD COMPOSITION

Every event was coded by words of 6 symbols; the first three denoted the order of arrival of the wavefront on the electrodes, while the others coded the shape of the cluster. In the case of no activations, in one or two electrodes, they were encoded using a special value (zero).

The words were composed as $(t_1,t_2,t_3,l_1,l_2,l_3)$ where t_y was the number of the activated electrode linked to the corresponding shape, l_x represented the cluster of the electrode x. For example (2, 1, 0, 3, 4, 0) means that an event on two electrodes has been found and the first activated electrode has been the second with a cluster equals to 4. The second activated electrode has been the first with a cluster equals to 3.

3.3.4 COMPUTATION OF THE OD

The organization degree (OD) was calculated using the Shannon Entropy (SE) of a series of words by

$$OD = \frac{H_0 - H}{H_0} \tag{3.1}$$

where H was the SE of the series of words and H_0 was the maximum SE obtainable from uniform distribution composed by 492 different symbols, *i.e.*, the total amount of possible words having the definition described in sec. 3.3.3. OD was bounded between 0 and 1. When series were not long enough to provide a sufficient convergency of the entropy's estimate, we calculated the value of H_0 by Montecarlo simulations.

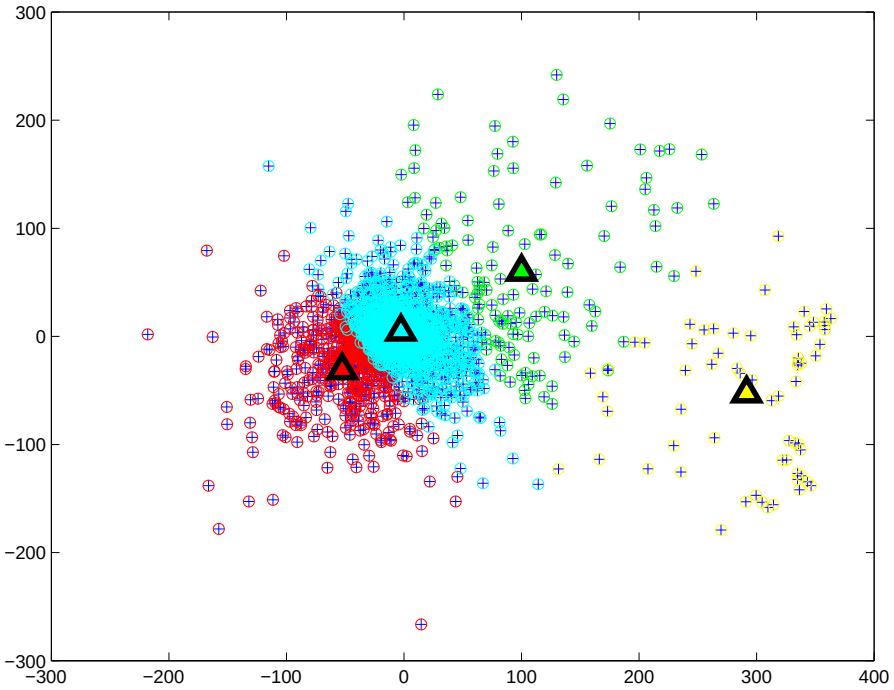

Figure 3.4: LAA waves during AF described by the first two PCs of the input matrix. Triangles mark the centroids as found by K-means.

3.4 REAL DATA VALIDATION

3.4.1 DATASET

The dataset was the same used in [88]. Briefly, it contained 10 subjects (8 males, 1 females, 1 not categorized; mean age 60 ± 6 years) suffering from either paroxysmal or persistent AF. This dataset was generated in a study designed to evaluate the effect of the pro-arrhythmic role of the autonomous nervous system, using isoproterenol (ISO). Four different sets of bipolar AEGs were measured and named using the experimental protocol phase (PP).

The protocol was divided into 4 phases:

1. Measurements in SR
2. Measurements in SR after infusion of ISO (SRISO)
3. Measurements in AF
4. Measurements in AF after infusion of ISO (AFISO)

Each sets contained the 12 standard leads for the surface ECG and 5 bipolar AEGs recordings collected using a coronary sinus (CS) catheter (the electrodes were spaced about 2 mm from each other and were linearly located along the catheter).

3.4.2 PREPROCESSING

A passband filter was applied to AEG to reduce the baseline wandering and the high frequency noise (0.5-250 Hz).

The ventricular activity was present on the AEGs. Since the use of numerical filtering was not helpful in this case (see chap. 2), the classic template matching and substraction (TMS) [25] was used. Here, we decided to apply the classic TMS because the power of the ventricular activity was relatively small.

3.4.3 ACTIVATION TIME (AT) DETECTION

In order to estimate the position of the localized atrial activity (LAA), a set of numerical filters was applied to the AEG as in [85]. An adaptive threshold was used to detect peaks, and a blank period was selected (50 ms) to avoid double detections of the same wave.

LAAs displaying a cross-correlation larger than 0.9 were used to build a template, and these were aligned on the template ($\pm$4 ms); the process was repeated until convergence was reached. The alignment increased the quality of the clustering procedure described in the next section.

3.4.4 RESULT

We applied the method on 7 subjects (3 subjects were discarded for the low quality of the recordings). For every set of recordings, three spatially close bipolar electrodes were analyzed: [CS1, CS2, CS3], [CS2, CS3, CS4], [CS3, CS4, CS5]. For each of them, the OD was calculated and the median value was taken into account to describe the organization of a subject during that specific protocol phase. The OD values obtained in the different phases were compared by means of a paired t-test ($p < 0.05$).

The organization degree was also computed by using only words composed of three symbols (instead of 6). When we considered the times of arrival, we termed the index OD_{AT}, and when the shapes were taken into account, we labeled OD_S. The last one, *i.e.*, OD_S, was used to mimic and to compare OD with an index recently proposed by Faes *et al.* [85] that was based on the evaluation of the similarity between morphologies of LAAs.

Table 3.1: Organization degrees in AF. Mean(interquartile range); * $p < 0.05$

	AF	AFISO	
OD	$0.35(0.32-0.36)$	$0.32(0.27-0.35)$	*
OD_{AT}	$0.11(0.05-0.11)$	$0.12(0.07-0.15)$	
OD_S	$0.32(0.28-0.35)$	$0.29(0.24-0.34)$	

The average heart rate in each protocol phase was: i) 72.77 ± 13.44 bpm in SR; ii) 91.51 ± 16.41 bpm in SRISO; iii) 114.82 ± 30.83 bpm in AF; and iv) 141.73 ± 30.64 bpm in AFISO.

In all series, the mean value of the OD of SR was not significantly different to the SRISO's one. The results regarding the OD are summarized into tab. 3.1.

3.5 CONCLUSION

The method proposed in this work was capable to distinguish different atrial activity organizations. It supported the idea that considering both the shapes and the times of arrival of the wavefronts could permit a more complete description of atrial organization.

We compared the mean values of ODs between different phases of a clinical protocol which included administration of isoproterenol in SR and AF. During SR, the mean values of OD_{SR} and OD_{SRISO} were not significantly different. This is reasonable because the adrenergic drug increases the heart rate while the wavefronts still come from the same physical direction. In AF, the average OD values were significantly different because of the increased complexity of the fibrillatory status induced by the drug, as recently shown in [88] using linear and non-linear metrics applied on the inter-time interval between LAAs.

We also built the organization index using only the times of arrival: if the same pattern persists in time the organization degree is higher. However we preferred to consider both the information provided by the shapes of the waves and their times of arrival for a more thorough description of the biological phenomena. The results confirmed our initial hypothesis. Also, we estimated the organization degree by using only the information contained in the shapes of the wavefronts (OD_S) or in the times of arrival (OD_{AT}). Both of them were not able to detect the changes in the organization forced by the drug.

The method requires the selection of the number of bipolar electrodes used to construct the codewords. Here, it was set to three. This was a compromise between a fine symbolic description of the fibrillatory status, and the necessity to keep the number of possible words limited (as it has a clear effect on the convergence and reliability of SE estimates). However, the dependence of OD on the number of words should be quantitatively addressed in the future.

Furthermore, future research should tackle the effects on the symbolic series of preprocessing, ATs detection, length of the series and clustering. In particular, related to the latter, PCA and K-means produced a reduction of the dimensionality of the problem (as in [89]), which was necessary to render reliable the entropy's estimate. However, using a small number of clusters (4), information might get lost as slightly different dipoles could have been forced to stay in the same cluster.

In conclusion, the work presented highlights how the direction of wave propagation, encoded in a symbolic word, can aid to describe the degree of organization of the fibrillatory status. However, the study is preliminary and requires further investigations.

4

MODEL-BASED FEATURE EXTRACTION: A VALIDATION STUDY OF $\mathcal{V}$-INDEX

This chapter describes the validation of a new model-based feature, the $\mathcal{V}$-index, using real data. Such index has been proposed by Sassi and Mainardi [43] recently.

The $\mathcal{V}$-index is capable to estimate the dispersion of the time of occurance of the transient sources. When applied on ECG, it can quantify the spatial dispersion of the ventricular repolarization providing an estimate of the standard deviation of the repolarization times of the myocytes across the whole heart.

This parameters is extracted on real data in three different dataset, including subjects: i) under sotalol administration [90]; ii) under moxifloxacin administration [91]; and iii) affected by Chagas disease [92, 93].

4.1 SOURCE MODEL

The $\mathcal{V}$-index is based on two models: i) an equivalent linear surface model; and ii) a repolarization time model.

4.1.1 EQUIVALENT LINEAR SURFACE MODEL

Sources are mixed linearly and a set of measurements is available over time according to the model

$$\psi(t) = A \begin{bmatrix} D_1(t-\rho_1) \\ D_2(t-\rho_2) \\ \cdots \\ D_M(t-\rho_M) \end{bmatrix} \tag{4.1}$$

where ψ is $L \times N$ measurement matrix (L is the number of leads and N is the number of samples), A is the $L \times M$ transfer matrix and $D_i(t - \rho_i)$ is the i^{th} transient source that occurs at time ρ_i (M is the number of transient sources).

Defining

$$\rho_m = \bar{\rho} + \Delta\rho_m \tag{4.2}$$

where $\bar{\rho}$ is the mean occurance time across transient sources and $\Delta\rho_m$ is repolarization delay of the m^{th} transient source, it is possible to derive the second order approximation of the equation (4.1) centered in $\bar{\rho}$ as

$$\begin{aligned} D(t - \rho_m) = D(t - \bar{\rho}) - \Delta\rho_m \frac{dD(\tau)}{d\tau}|_{\tau=t-\bar{\rho}} + \cdots \\ \cdots + \frac{\Delta\rho_m^2}{2} \frac{d^2D(\tau)}{d\tau^2}|_{\tau=\rho-\bar{\rho}} + o(\Delta\rho_m^3) \end{aligned} \tag{4.3}$$

Naming $T_d = \frac{dD(\tau)}{d\tau}|_{\tau=t-\bar{\rho}}$, lead factor $w_1 = -A\Delta\rho$ and lead factor $w_2 = A\frac{\Delta\rho_m^2}{2}$, the measurement matrix can be approximated by

$$\psi(t) \simeq w_1 T_d + w_2 \dot{T}_d + C \tag{4.4}$$

The source model of eq. 4.1, proposed van Oosterom [44], is able to link the transmembrane action potential of the myocites with the surface ECG. Indeed, the surface of the ventricle can be divided in M nodes (or cells) and the measured ECG $\psi(t)$ is given by a weighted summation of the action potential of every cell. The quantity $-T_d$ is called dominant T-wave (DTW) by van Oosterom. Moreover, due to the properties of the matrix A (each row sums to 0), the constant term C in eq. (4.3) is 0. This fact reflects that constant electrical potential across the ventricles, at a given time, does not produce any variation on the measurements. Finally, it is worth noting that in eq. 4.4, the action potential of each myocites is approximated with a single AP function whose derivative is the dominant T-wave.

4.1.2 REPOLARIZATION TIME MODEL AND $\mathcal{V}$-INDEX

In 2011, Sassi and Mainardi [43] proposed a statistical model for the repolarization times of the ventricular cells; their model was

$$\Delta\rho_m = \theta_m + \varphi(k) \tag{4.5}$$

where θ_m represented the fixed time of the repolarization of the m-node (a constant property of the m-node), while $\varphi(k)$ modeled the small random variations across beats (a normal distribution with zero mean and variance depending on the heart rate).

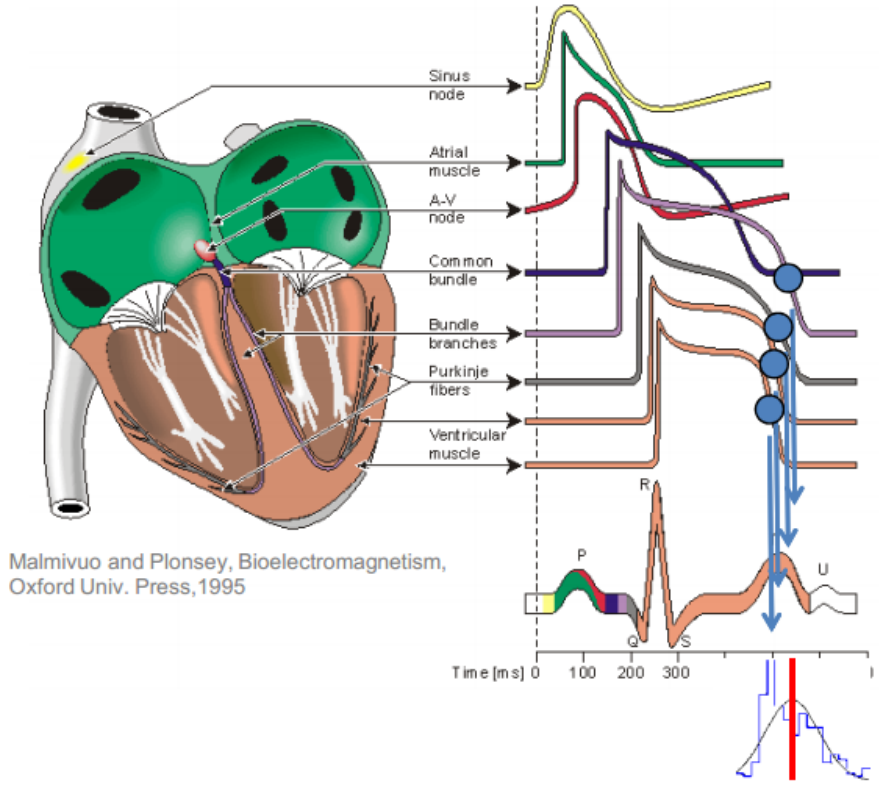

Figure 4.1: Drawing of APs across the heart with the distribution of RTs.

Using eq. (4.4) and eq. (4.5), they developed a formula to estimate the dispersion of the repolarization times by means of

$$\mathcal{V}_l = \frac{\mathrm{std}(w_2(l))}{\mathrm{std}(w_1(l))} \simeq s_\theta \tag{4.6}$$

where l was the lead and the standard deviation was computed across beats.

The metric produces a vector of L estimates of the dispersion of the repolarization times even if the value s_θ is constant across leads. A lead-dependent part is added to the metric and so, Sassi and Mainardi suggested to compute either the mean or the median value of all those values to reinforce the final estimate. Figure 4.1 shows a drawing explaining what the $\mathcal{V}$-index measures.

This concept can be easily generalized to any other problems in which the followings conditions are satisfied: i) the source model is composed by a linear combination of transient sources (eq. 4.1); ii) the morphologies of the transient sources do not differ too much ($D_i(t) \approx D(t)$ for each i); and iii) the second order approximation holds, *i.e.*, the dispersion of the repolarization times ($\Delta\rho_m$) is "small" enough.

4.2 $\mathcal{V}$-INDEX ESTIMATION ALGORITHM

An iterative algorithm structure is proposed to estimate the lead factors and the dominant T-wave, *i.e.*, fitting of the model in eq. 4.4 on a T-wave. After the initialization of

a first estimate of T_d (using the first right-singular vector of the SVD of ψ, as proposed by van Oosterom), the lead factors are determined by solving a linear system (being ψ linearly dependent on w_1 and w_2 when T_d is kept constant; see eq. 4.4). A new dominant T-wave, *i.e.*, a refined one, is determined minimizing the Frobenius norm of the error between the measured ψ and the model in eq. 4.4, when considering the lead factors previously calculated. Such technique is named operation splitting. Scheme in fig. 4.2 shows the structure of the algorithm.

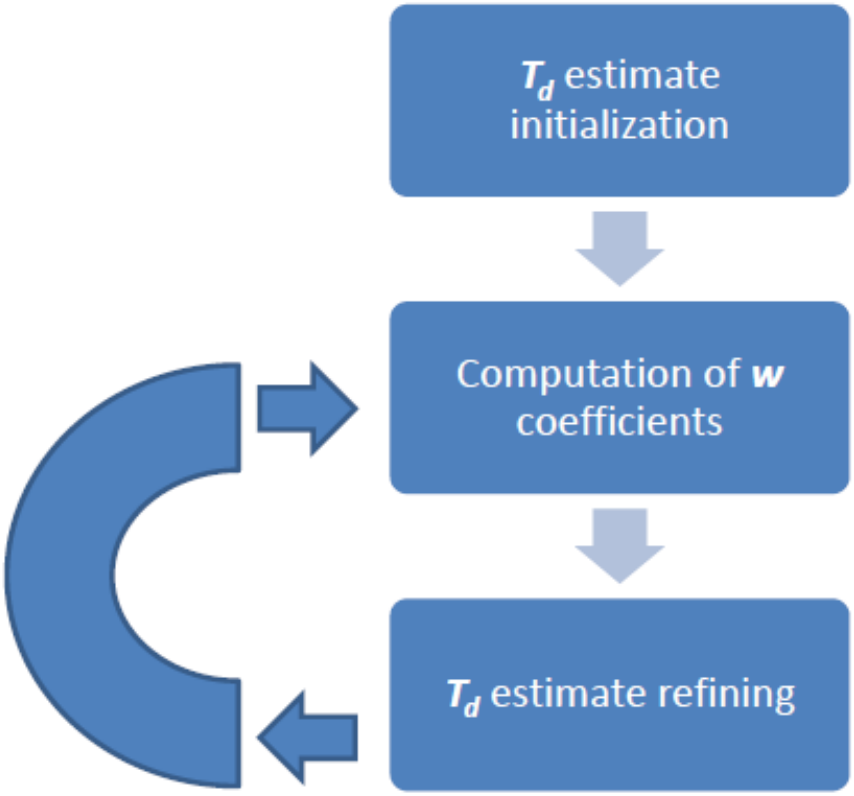

Figure 4.2: Scheme of the iterative algorithm for estimating the lead factors and the dominant T-wave T_d.

Four different algorithms for refining the dominant T-wave have been proposed [43, 94]. The first one involved only numerical calculus in the determination of T_d and its first derivate. Indeed, the function T_d can be calculated by means of the Eulero-Lagrange equation. The first derivate was computed using the centered differentiating formula. However, a 2^{th} order approximation model (eq. 4.4) might not be appropriate when $\Delta\rho_m$ is large. For such reason, higher order approximation models have been studied employing numerical simulations, to provide a better approximation error and a lesser bias between the true s_θ and the estimated $\mathcal{V}$-index. Yet, numerical differentiation becomes unstable due to noise present on real measurements. In order to address such issue, three parametric forms were used for approximating the dominant T-wave (using Levenberg-Marquardt fitting algorithm). The advantage of using parametric forms was that they were differentiable analytically but, on the other hand, the computational cost was higher, due to the non-linear fitting procedure.

Parametric forms did not provide significant differences with respect to the numerical algorithm for justifying an increase of the computational cost [94]. Hence, the numerical algorithm was used for the estimation of the $\mathcal{V}$-index in the studies described in the following sections.

4.3 REAL DATA VALIDATION

In this section, three different studies on real data are carried out to validate the $\mathcal{V}$-index, and to verify whether it is sensitive to physiological changes in the dispersion of the ventricular repolarization. The first two studies involve subjects under administration of two different drugs, *i.e.*, sotalol and moxifloxacin, and in the last one, a dataset of patients affected by Chagas disease is analyzed (see sec. 6.3.1).

Sotalol, moxifloxacin and Chagas disease are known to increase the heterogeneity of the ventricular repolarization [95, 33, 96]. While sotalol is considered pro-arrhythmic, increasing significantly the QT interval, moxifloxacin produces a prolongation of a few milliseconds (around 10 ms). On the other hand, Chagas disease frequently causes a progressive deterioration of the heart and it might affect the anatomy of the myocardium (myocarditis, cardiomegaly). For such reason, it is hypothesized that the abnormal enlargement of the myocardium could also alter the spatial distribution of repolarization times across the heart.

In conclusion, the aim of the study is to test the capability of the $\mathcal{V}$-index to estimate the dispersion of the ventricular repolarization. The QT interval is reported as well (see 1.3 for its description).

4.3.1 DATASETS AND PROTOCOL OF THE STUDIES

4.3.1.1 SOTALOL

The study population was composed by 39 healthy subjects in which 12-leads 24-hour digital Holter recordings were collected in three consecutive days (sampling frequency: 180 Hz; LSB: 2.50 μV). During the first day no drugs were administrated, and we used the data collected in this day as reference baseline values. A 160 mg dose of sotalol was injected the second day and a double dose was given the third one. In the third day, only 22 subjects were involved in the study. This dataset was the same used in [97].

Sotalol was given at 8:00 a.m., while plasma concentrations were measured at 16 predefined subsequent time instants, which in the following will be referred to as "time-points". For protocol details, please refer to [95].

QT intervals, heart rate corrected according to the Bazzet formula (QT_B), were provided with the dataset, and then used for comparison with the $\mathcal{V}$-index.

4.3.1.2 MOXIFLOXACIN

The E-HOL-12-0140-008 dataset from the Telemetric and Holter ECG Warehouse (THEW) was retrospectively analyzed. It contained 24-hour digital Holter recordings (12 standard leads, sampling frequency: 1 kHz, LSB: 3.75 μV) collected from 68 healthy subjects.

For each participant, two registrations were available when either a placebo or moxifloxacin (a 400 mg dose) were administrated. Drug's serum concentration was assessed at 11 time-points during the entire day.

QT intervals were determined using the algorithm described in 4.3.2 and then corrected using the Fridericia formula (QT_F) for a direct comparison with the Bloomfield's results [33]. They were determined as an average of QT values for beats with similar preceding RR values, then corrected with the average of these RR interval lengths.

4.3.1.3 CHAGAS DISEASE

Data were collected at the Chagas Disease Outpatient Reference Center of the Universidade Federal de Minas Gerais, Brazil. The study was designed as an observational cohort study and previously described in [98, 99]. Briefly, 113 patients aged $21-67$ (mean: 42.5) were enrolled between 1998 and 1999 and completed a 10-year follow-up period. The patients had a definite serological status showing a positive reaction to *Trypanosoma cruzi* and were followed until death or the end of the follow up in 2008. Death cases were not categorized, so no distinction was made between sudden, cardiac and non-cardiac death. 14 out of 113 subjects died during a 10-year follow-up period.

Several laboratory analysis and ambulatory tests were collected at enrollment, among which a 10 minutes 3 lead Holter recording, at rest in controlled conditions. The recordings were performed with a Burdick (Altair) digital Holter recorder with 1000 Hz sampling frequency and 10- or 16-bit resolution.

Two main analysis were performed. First, the average $\mathcal{V}$-index was tested between subjects who survived and who did not. Second, a multivariate survival analysis was performed to assess the hypothesis that the $\mathcal{V}$-index might be an independent prognostic factor. The multivariate model included also prolonged QRS duration ($>$ 133 ms), left ventricular ejection fraction (LVEF, measured using the Simpson's method) below 50%, ventricular tachycardia at either Holter monitoring or stress testing and median T-wave amplitude variability (TWV) $>$ 30 μV. For a definition of TWV please see [100].

The modeling strategy was enforced to reduce the risk of over-fitting because of the small sample size. The "optimism" of the model (to be limited) was evaluated according to Harrell [101]. Adjusted ("shrunk") regression coefficients were calculated using the linear shrinkage method [102].

4.3.2 PREPROCESSING AND FIDUCIAL POINT DETECTION

ECG recordings were preprocessed using a bandpass Butterworth filter (3^{th}-order, passband: $0.5-40$ Hz) to reduce powerline interference, baseline wandering and high frequency noise. After filtering, the baseline of all signals was adjusted: for each channel, the mode of the ECG's samples distribution (computed using a bin size of 75 μV) was identified. Then, ECG samples belonging to the modal bin were linearly fitted, and the obtained regression line subtracted from the signal.

Beat locations were provided for the moxifloxacin dataset, and detected for the sotalol and Chagas data using a multilead detector based on a modified version of OSEA (EP Limited, MA, USA, 2003). Then, the T-waves were segmented; in particular, the

end was determined using the Surawicz method [103]. This procedure does not need to be accurate because the $\mathcal{V}$-index has proven to be robust to displacement of fiducial points [104].

The quality of the leads was determined as the average crosscorrelation between a mean QRS complex and each ones. A lead was considered good when such average was higher than 0.9.

4.3.3 DATA ANALYSIS AND PARAMETER COMPUTATION

For the sotalol and moxifloxacin dataset, three consecutive windows, 10 minutes each, were analyzed at every time-point. The values of QT or $\mathcal{V}$-index obtained in the three windows were then averaged. For the Chagas data, only a 10-minute window was available.

The computation of both QT and $\mathcal{V}$-index required a heart rate to be approximately "stationary". Therefore, beats were selected using a criterion similar to the "binning" procedure proposed by [105]. A beat was considered "stable", and included into the computation, if the two preceding RR values were within ± 25 and ± 50 ms, respectively, with respect to a constant $\widehat{\text{RR}}$ value. Considering the beats in a given ECG segment, $\widehat{\text{RR}}$ was selected such to maximize the number of beats (typically it corresponded to the median value, but not necessarily). This approach was used for the sotalol and moxifloxacin data while for the Chagas data, a different procedure was used to select beats. Briefly, beats were selected only if their RR intervals were close enough to the mean RR. The threshold was adjusted to be as small as possible and to contain at least 60 beats, for a direct comparison with [98].

The $\mathcal{V}$-index was estimated using the algorithm described in sec. 4.2. A value of $\mathcal{V}$-index was obtained for each leads. We employed their average as overall estimate of the $\mathcal{V}$-index. The $\mathcal{V}$-index was determined only when, at least 3 good-quality leads were available (see 4.3.2), and 64 stable beats for the sotalol and moxifloxacin data, and 60 for the Chagas dataset were selected.

4.3.4 RESULTS

4.3.4.1 SOTALOL

The plasma concentrations of sotalol is shown in 4.3. The maximum values were measured after around 3 hours from administration. The time evolution of $\mathcal{V}$-index and QT_B is shown in 4.4.

After each sotalol's dose administration, both $\mathcal{V}$-index and QT_B were statistically larger than the time-matched values at baseline (day 1 vs day 2 and day 2 vs day 3), for the majority of the time-points ($p < 0.05$, after Bonferroni's correction for repeated comparisons). An estimate of $\mathcal{V}$-index was not available for each subject at every time-point, due to poor signal quality or to a small number of stable beats (the average percent of subjects for which a $\mathcal{V}$-index value was available in a time-point was 75.3%).

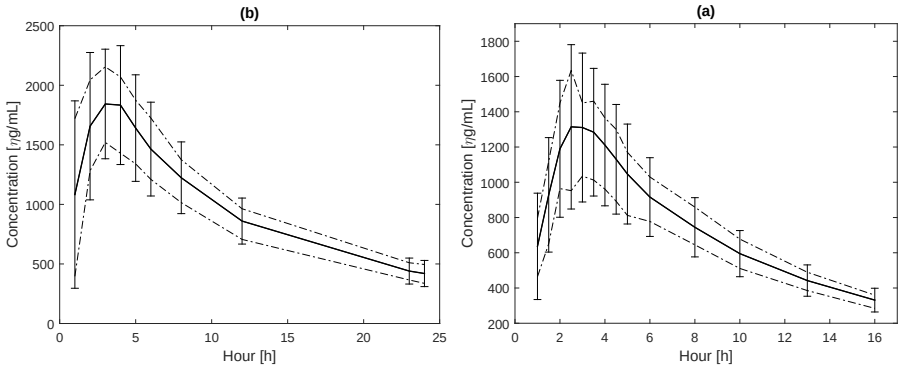

Figure 4.3: Mean and standard deviation of the serum concentration of sotalol (a) and moxifloxacin (b) over time. Dashed lines are the 25^{th} and 75^{th} percentiles, respectively.

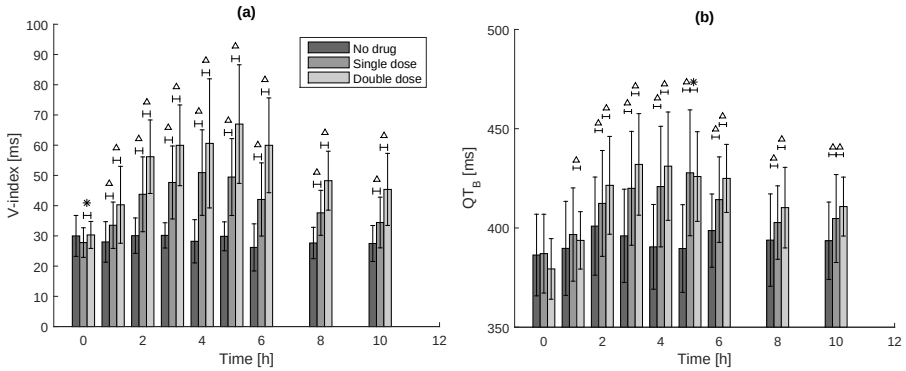

Figure 4.4: Mean $\pm$ standard deviation of $\mathcal{V}$-index (a) and QT_B (b) values during day 1 (no drug), day 2 (single dose of sotalol) and day 3 (double dose of sotalol). $*$: time-instants at a which statistically significant differences were obtained (paired single-tail Wilcoxon test, $p < 0.05$); $\triangle$: significance was retained after Bonferroni's correction. The standard deviation was estimated as $1.4826 \times$MAD, where MAD is the median absolute deviation, to reduce the possible impact of outliers. For clarity, only a selected number of time-points was included in the figure.

The maximum value of $\mathcal{V}$-index occurred on average after 5.64 hours after administration, on day 2, and after 2.71 hours, on day 3. QT_B peaked about 4.27 hours from administration, at day 2, and after 2.05 hours, at day 3. Both indexes' maximum values were statistically different (paired single-tail Wilcoxon test $p < 0.05$) from baseline, at day 2 ($\mathcal{V}$-index baseline: 27.79 ms $\pm$ 4.89 ms vs peak: 60.13 ms $\pm$ 18.52 ms; QT_B baseline: 387.07 ms $\pm$ 19.84 vs peak: 437.76 ms $\pm$ 32.05 ms) and at day 3 ($\mathcal{V}$-index baseline: 30.32 ms $\pm$ 4.46 ms vs peak: 79.79 ms $\pm$ 27.60 ms; QT_B baseline: 379.36 ms $\pm$ 15.26 ms vs peak: 447.97 ms $\pm$ 20.39 ms).

The relative percent variation of $\mathcal{V}$-index at peak was statistically higher than that of QT_B in both day 2 and day 3 (day 2: $\mathcal{V}$-index% peak: 114.77% $\pm$ 33.15% vs QT_B% peak: 12.13% $\pm$ 2.85%, $p = 1.911 \times 10^{-7}$; day 3: $\mathcal{V}$-index% peak: 188.75% $\pm$ 53.58% vs QT_B% peak: 18.47% $\pm$ 2.85%; paired single-tail Wilcoxon test $p < 0.05$).

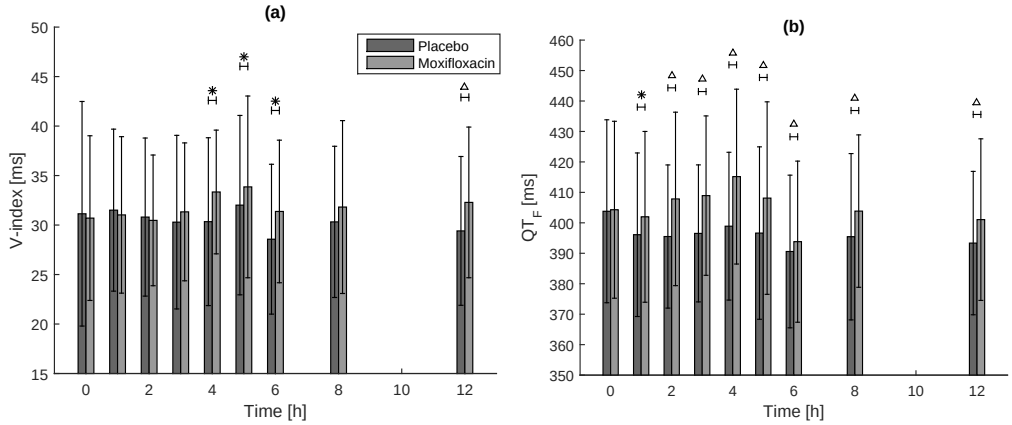

Figure 4.5: Mean ± standard deviation of $\mathcal{V}$-index (a) and QT_F (b) values over time, after placebo and moxifloxacin administration. $*$: time-instants at which statistical significant differences were obtained (paired single-tail Wilcoxon test, $p < 0.05$); $\triangle$: significance was retained after Bonferroni's correction. To reduce the possible impact of outliers, the standard deviation was estimated as $1.4826 \times$MAD, where MAD is the median absolute deviation. For clarity, only a selected number of time-points was included in the figure. In panel (b), the difference in QT_F after moxifloxacin administration was significantly larger than 10 ms, confirming that the statistical sensitivity of our setup was coherent with what expected in [33, 32].

4.3.4.2 MOXIFLOXACIN

The plasma concentrations of moxifloxacin is shown in 4.3. As for the sotalol, the maximum values were measured after around 3 hours from administration.

The time evolution of $\mathcal{V}$-index and QT_F is shown in 4.5. On average, in each time-point, $\mathcal{V}$-index values were available for 94.28% of the subjects). As shown, at several time-points, $\mathcal{V}$-index and QT_F values were significantly different from the corresponding values in the placebo arm.

Maximum values were reached, on average, after 5.01 hours for $\mathcal{V}$-index and after 4.37 hours for QT_F. Peak values were statistically larger than those during baseline (moxifloxacin arm, $\mathcal{V}$-index baseline: 30.70 ± 8.32 ms vs peak: 40.48 ± 7.61 ms and QT baseline: 404.29 ± 29.05 ms vs peak: 426.77 ± 36.67 ms; paired single-tail Wilcoxon test $p < 0.05$). The relative percent variation of $\mathcal{V}$-index at peak was statistically higher than that of QT_F ($\mathcal{V}$-index: $34.56\% \pm 24.60\%$ vs QT_F: $5.56\% \pm 2.98\%$; paired single-tail Wilcoxon test $p = 3.640 \times 10^{-11}$).

4.3.4.3 CHAGAS DISEASE

The $\mathcal{V}$-index was determined on each recording but on three cases. Those values larger than 100 ms were excluded from the analysis because estimated on poor quality signals and/or with small number of stable beats. After excluding the bad estimates, the $\mathcal{V}$-index was computed on an average of 76 ± 19 beats.

The survivors had an average $\mathcal{V}$-index and QT_B value smaller than those of non-survivor ($\mathcal{V}$-index S: 31.2 ± 13.3 ms vs NS: 41.2 ± 18.6 ms, $p = 0.029$; QT_B S: 420.0 ± 30.2 vs NS: 443.2 ± 36.6, $p = 0.022$; single-tail Wilcoxon rank sum test). Boxplots of $\mathcal{V}$-index and QT_B are given in fig. 4.6 for both S and NS.

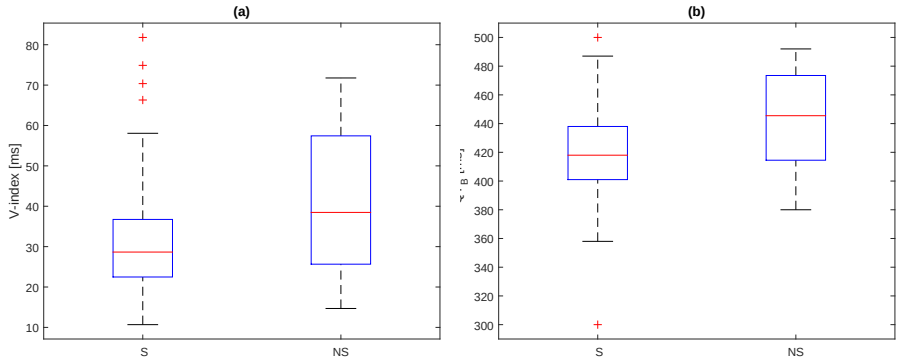

Figure 4.6: Boxplot of the $\mathcal{V}$-index (a) and QT_B (b) values for the surviving (S) and non-surviving (NS) subjects.

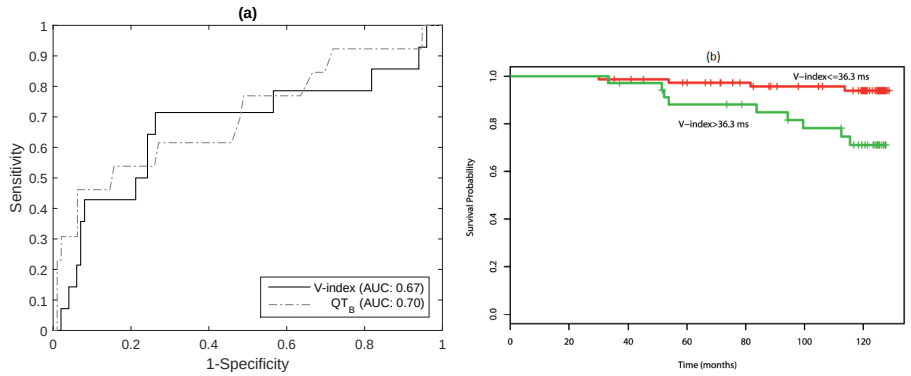

Figure 4.7: ROC curve (a) and Kaplan-Mayer curves (b) of $\mathcal{V}$-index in the survival analysis.

The $\mathcal{V}$-index was dichotomized at the cut-off value 36.3 ms determined as the value which maximized positive and negative predictability in the ROC curve (the point at which sensitivity and specificity were equivalent and equal to 71.4%). The area under the curve was small for both $\mathcal{V}$-index (0.672) and QT_B (0.704). Figure 4.7 shows the ROC curves for $\mathcal{V}$-index and QT_B, and the Kaplan-Mayer curves for $\mathcal{V}$-index.

A $\mathcal{V}$-index larger than 36.3 ms was related to an elevated risk of death in a univariate Cox proportional hazards analysis (hazard ratio, $HR = 5.34$, $p = 0.0046$) and the log-rank χ^2 test ($p = 0.0022$) suggests a significant distinction on mortality across the two populations. Figure 4.6 shows the Kaplan-Meier curves when the $\mathcal{V}$-index was dichotomized.

Finally, once dichotomized at 36.3 ms, the $\mathcal{V}$-index retained its prognostic value in a Cox proportional-hazards analysis, after adjustment for the other four variables considered: prolonged QRS duration ($>$ 133 ms), left ventricular ejection fraction (LVEF, measured using the Simpson's method) below 50%, ventricular tachycardia (VT) at either Holter monitoring or stress testing and median TWV $>$ 30 μV. These thresholds values were determined in [99]. The significance was preserved for any of the five factors, even when the shrinkage method was used to protect against over-fitting on small sample size.

Table 4.1 contains the results of the analysis. The shrinkage factor was $s = 0.918$ (likelihood ratio $\chi^2 = 56.71$, degrees of freedom: 5).

Table 4.1: Multivariate Cox Proportional-Hazards Analysis of risk of death in Chagas disease patients.

	β coefficient	Shrunk β coefficient	SE	Hazard ratio	95% CI
LVEF $< 50\%$	1.80	1.65	0.71	5.19	$1.30 - 20.73$
VT	2.24	2.05	0.82	7.74	$1.56 - 38.38$
QRS > 133 ms	2.14	1.95	0.82	7.05	$1.42 - 35.01$
TWV $> 30\mu$V	2.44	2.22	0.85	9.24	$1.75 - 48.66$
$\mathcal{V}$-index > 36.3 ms	1.52	1.39	0.66	4.00	$1.09 - 14.66$

4.4 CONCLUSION

In this chapter, a preliminar validation of a new index of dispersion, *i.e.*, the $\mathcal{V}$-index, has been described. When applied to ECG, such index estimates the heterogeneity of the ventricular repolarization as a measure of the standard deviation of the repolarization times of the myocites.

In particular, the $\mathcal{V}$-index is found to be associated with an increase in the ventricular heterogeneity when sotalol is administrated. Indeed, sotalol is known to be a potassium channel-blocker and a β-blocker [95], and it is normally used for the suppression of cardiac arrhythmias. However, an important side effect is to significantly prolong the action potential of the midcells [106]. Such block is related with a high risk of genesis of lethal arrhythmias as Torsade de Pointes. Therfore, a high heterogeneity of the ventricular repolarization as well as a prolongation of the QT are expected when sotalol is administrated. In this context, the $\mathcal{V}$-index was highly correlated with the QT interval in response to the plasma concentration of the drug for both single and double dose.

Similar results are obtained with the administration of moxifloxacin. Such drug produces a small increase of the QT interval ($\approx$ 10 ms; [33]) but it is not considered proarrhythmic (in fact it is typically used for drug safety evaluations such as in "thorough QT study"). In this regard, the $\mathcal{V}$-index is associated with an increase of the spatial heterogeneity at the peak plasma concentration ($> 20\%$ with respect to baseline) and also, it was correlated with a prolongation of the QT interval. Our results are in agreement with those of Chen *et al.* [107] on dogs where, at different moxifloxacin concentrations, they noticed that the prolongation of the action potentials duration was more prominent in the endocardial region than in the epicardial one.

In addition, a structural remodelling of the heart, such as hypertrophy or destruction of autonomic innervations, typically produced by Chagas disease effects, is supposed to produce a high spatial heterogeneity of the ventricular repolarization. It has been shown that an increase of the spatial dispersion of the ventricular heterogeneity [93], measured by $\mathcal{V}$-index, as well as an increase of the temporal dispersion [99], measured by TWV [100], are both independent predictors of death.

Technically speaking, the computation of the $\mathcal{V}$-index requires: i) to fit a model (see eq. 4.4) on each T-wave; and ii) similarity between TMPs during repolarization. While

the former is just related on the fitting algorithm itself, the latter is more challenging. Indeed, to ensure the similarity, the ion currents crossing the cell membrane have to be as stable as possible over time. To mitigate such issue, beats can be selected close in time and with a stable heart rate because the same autonomic regulation is acting on the ion influx. In this context, a proper selection of beats can result in more robust estimates of the spatial heterogeneity.

The fitting algorithm is based on operation splitting and such can lead to a suboptimal solution. The problem, in fact, is not convex and the iterative procedure can result in a solution that is a local optimum. Moreover, the implementation used estimates a different dominant T-wave for each selected beat. Further investigations are needed in this regard, for example, using different optimization solvers or mathematical approaches.

On the other hand, the computation of the $\mathcal{V}$-index does not require a perfect positioning of the FPs [43]. Therefore, the temporal window for the fitting procedure can be located on the T-wave in a rough way.

In conclusion, a new parameter, *i.e.*, the $\mathcal{V}$-index, able to estimate the temporal dispersion of transient sources has been discussed and tested on a few scenarios. Furthermore, when employed on the T-waves of ECG recordings, it is related to the spatial heterogeneity of the ventricular repolarization. This parameter has proven to be sensitive to either changes of ventricular heterogeneity induced by drug's infusion such as sotalol and moxifloxacin, or anatomical restructuring produced by the Chagas disease.

The $\mathcal{V}$-index is still being validated. In particular, we are designing new experiments on both synthetic and real data. The former can provide insights on the reliability of either the estimate or the fitting algorithm with respect to the noise, while the latter will be useful to clarify the clinical applicability of this index.

5

NON MODEL-BASED FEATURE EXTRACTION: ACCELERATION AND DECELERATION CAPACITIES

This chapter describes the study and the validation of two new features, the average acceleration (AC) and deceleration (DC) capacity, recently introduced by Bauer *et al.* [51]. This technique can be applied on any kind of signals to determine an average rate of acceleration or deceleration.

An extensive set of simulations has been designed to provide insights into: i) the relationships between AC/DC and classical spectral features; and ii) a proper selection of the parameters on which both AC and DC depend on.

Afterwards, a validation study of AC/DC has been performed on real data involving an *in*-vivo near-term pregnant sheep model. This work was the first validation of the PRSA method in a fetal animal model. The aim of the study was to determine changes in AC and DC in response to fetal hypoxia and acidemia imposed by umbilical cord occlusions (UCOs), and to evaluate their correlation with acid-base biomarkers. Moreover, we investigated which ranges of the PRSA's parameters led to have maximal correlation with the acid-base biomarkers.

5.1 INTRODUCTION ON PHASE-RECTIFIED SIGNAL ANALYSIS AND ACCELERATION/DECELERATION CAPACITIES

Phase-Rectified Signal Averaging (PRSA) is a methodology capable of extracting quasi-periodic oscillations out of noisy and non-stationary signals. A quasi-periodic behavior is defined as a patch of periodic signals built by external interferences, typically the control system. The aim of such technique is to compress the signal into a much shorter sequence, *i.e.*, PRSA, in which only the relevant quasi-periodicities of the original series are present [48].

When applied on heartbeat interval time series (RR), it provides two measures to quantify the average cardiac acceleration (AC) and deceleration (DC) capacity of the heart rate.

When applied on heart beat interval time series (RR), AC and DC have proven to be predictors of risk in several clinical scenario [108, 50, 49, 109]. Of note, Bauer *et al.* [51] showed that DC was a better predictor of risk of death than left-ventricular ejection fraction (LVEF) and standard deviation of normal-to-normal intervals (SDNN) in myocardial infarction.

The computation of AC/DC is made into two steps. First, a list of anchor points is determine using the following rule

$$\sum_{k=0}^{T} RR(i+k) > \sum_{k=1}^{T-1} RR(i-k) \tag{5.1}$$

where T is a parameter of the PRSA and i is a possible candidate. The value of i will be inserted in the anchor point list only if the previous relation holds. Equation 5.1 determines the anchor point list for the deceleration capacity because it searches in the RR series all the segments in which an average deceleration of the heart rate, as function of the T value, occurs. The anchor point list for the acceleration capacity can be determined inverting the inequality sign in eq. 5.1 (the equality sign is avoided in both capacities). It is worth noting that such framework can be applied on signals from different domains.

Second, the PRSA is obtained aligning and averaging all the windows of length 2L centered on their anchor points.

Third, the capacity is determined

$$DC/AC = \sum_{k=0}^{s} \frac{PRSA(i+k)}{2s} - \sum_{k=1}^{s-1} \frac{PRSA(i-k)}{2s} \tag{5.2}$$

where s selects the number of points involved in the computation of the capacity.

Summarizing, the calculation of AC and DC depends on three parameters: T, L and s. In particular, T plays a role in the selection of the anchor points, L defines the half of the length of the PRSA and s determines the number of samples to consider for the computation of both capacities. (Refer to [110] for their complete description).

Despite the proven capability of AC/DC on several clinical scenarios, what they can really capture on an RR series, and what roles the parameters play, are still matter of investigation. To give an example, it is unclear to what extent AC and DC are correlated with sympathovagal modulation of the autonomous nervous system (ANS). Indeed, it is speculated that AC and DC could be related with the sympatho and vagal modulation respectively [109].

Furthermore, the values of the parameters on which AC/DC are dependent have been typically set to those that provided the best classification rate for the specific application.

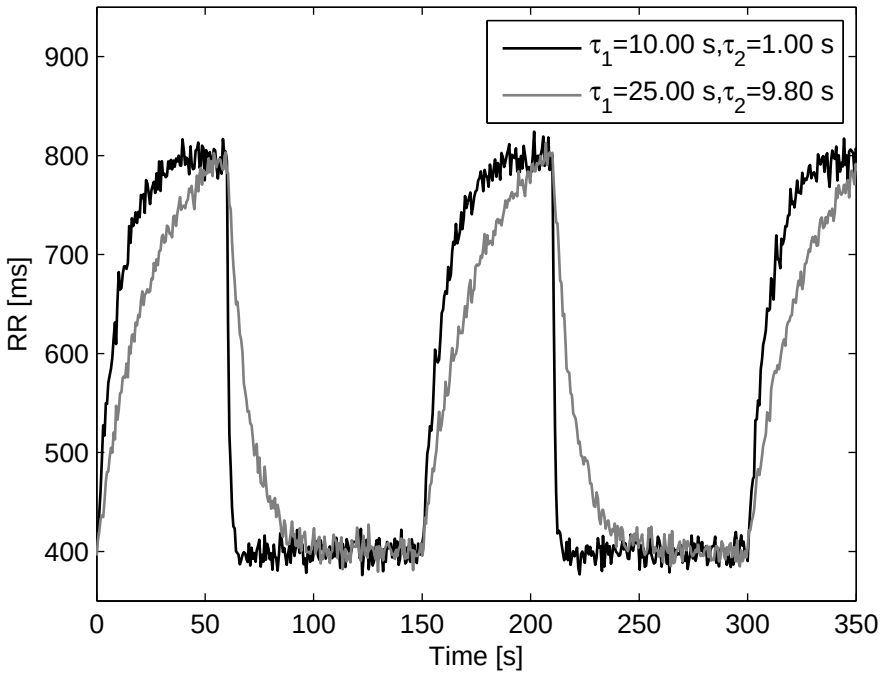

Figure 5.1: Example of UCOs with different growing and decreasing rates during umbilical cord occlusion.

5.2 ROLE OF THE PARAMETER L, T AND s BY MEANS OF NUMERICAL SIMULATIONS

An extensive set of numerical simulations was performed to provide insights about the meaning of AC/DC and for a more appropriate selection of the parameters [111]. In particular, the aims of the study were to: i) further clarify the influence of these parameters on AC/DC values; ii) evaluate the correlation between AC and DC; and iii) explore the relation between AC/DC and traditional spectral parameters. The simulations were designed considering both physiological and non-physiological models.

5.2.1 SIMULATION DESIGN

Three different sets of numerical simulations were prepared. $L = 40$ was consistently used in all of them.

First, the changes induced by different power spectra on AC/DC were evaluated varying the phase of the poles of a 2^{nd} order autoregressive (AR) model, between 0 and π (step 0.01), while normalizing the variance of the signals at 1 (the PRSA signal depends linearly on the variance of the series). Average measures were determined on 30 realizations of 3000 samples each. The hypothetical sample frequency was set to 2.5 Hz. Such analysis was repeated for s between 1 to 20 and $T = s$ or $T = 1$.

However, synthetic signals obtained from 2^{nd} order AR models, contained only a single periodic component. To have more realistic series (in adult human heart rate at least 3 components are present, typically labelled VLF, LF and HF), 93 AR models

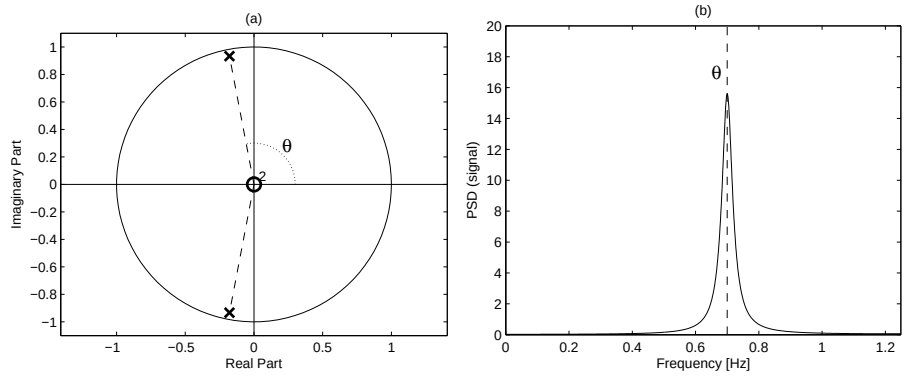

Figure 5.2: Example of location of poles of the 2nd order AR model (a) and its power spectrum (b). Sample frequency $f_s = 2.5$ Hz.

were fitted on 300 samples-long artifacts-free RR series, one for each subject in the Physionet's `nsr2db` (healthy) and `chf2db` (congestive heart failure) databases. Models' orders were significantly larger than 2 (minimum model order was 8, fulfilling Akaike's information criterion and Anderson's whiteness test). For each AR model, average AC and DC values were determined on 30 synthetic series, varying $s = T$ from 1 to 20. The power of the signals was normalized to 1.

Sawtooth-like heart rate trends[1] (*e.g.*, fig. 5.1) were employed for the third set of simulations, to assess the impact of time-reversal symmetry (or lack-of, as in asymmetric trends, *i.e.*, displaying different time-constants for the growing and decreasing traits) on AC/DC. Trends y were generated solving the ordinary differential equation:

$$\dot{y} = -\tau_2^{-1} y - \left(\tau_1^{-1} - \tau_2^{-1}\right) u y + u, \tag{5.3}$$

where u is the external input ($u = 1$ determines the presence of the trend), and τ_1 and τ_2 are the time-constants of the growing and decreasing traits, respectively. For the simulations, τ_1 was varied from 5 to 50 and τ_2 from 1 to 10. Finally, white Gaussian noise was added to y (signal-to-noise ratio: 25 db). Average values of AC/DC were obtained from 30 realizations, using $s = T$.

5.2.2 SIMULATION RESULTS

5.2.2.1 VARYING LOCATION OF AR MODELS' POLES

First, the mean value of AC (or DC), for a given phase of the poles of the 2nd order AR models (fig. 5.2), was more affected by s than T (fig. 5.3d-f). Hence s played a major role on selecting the frequency of the oscillations which most influenced AC/DC. Changing T surely modified the PRSA series by limiting its frequency content. However, if PRSA is subsequently used to assess AC/DC, the band-pass filtering effects imposed

1 Sawtooth-like RR series are common, for example, in sport medicine, *e.g.*, intervals training, or in fetal animal models, *e.g.*, umbilical cord occlusions. Within the context of UCO, the term u in equation 5.3 models the pressure signal occluding the umbilical cord and the series y varies from 400 to 800 ms, which is typical for a sheep fetus.

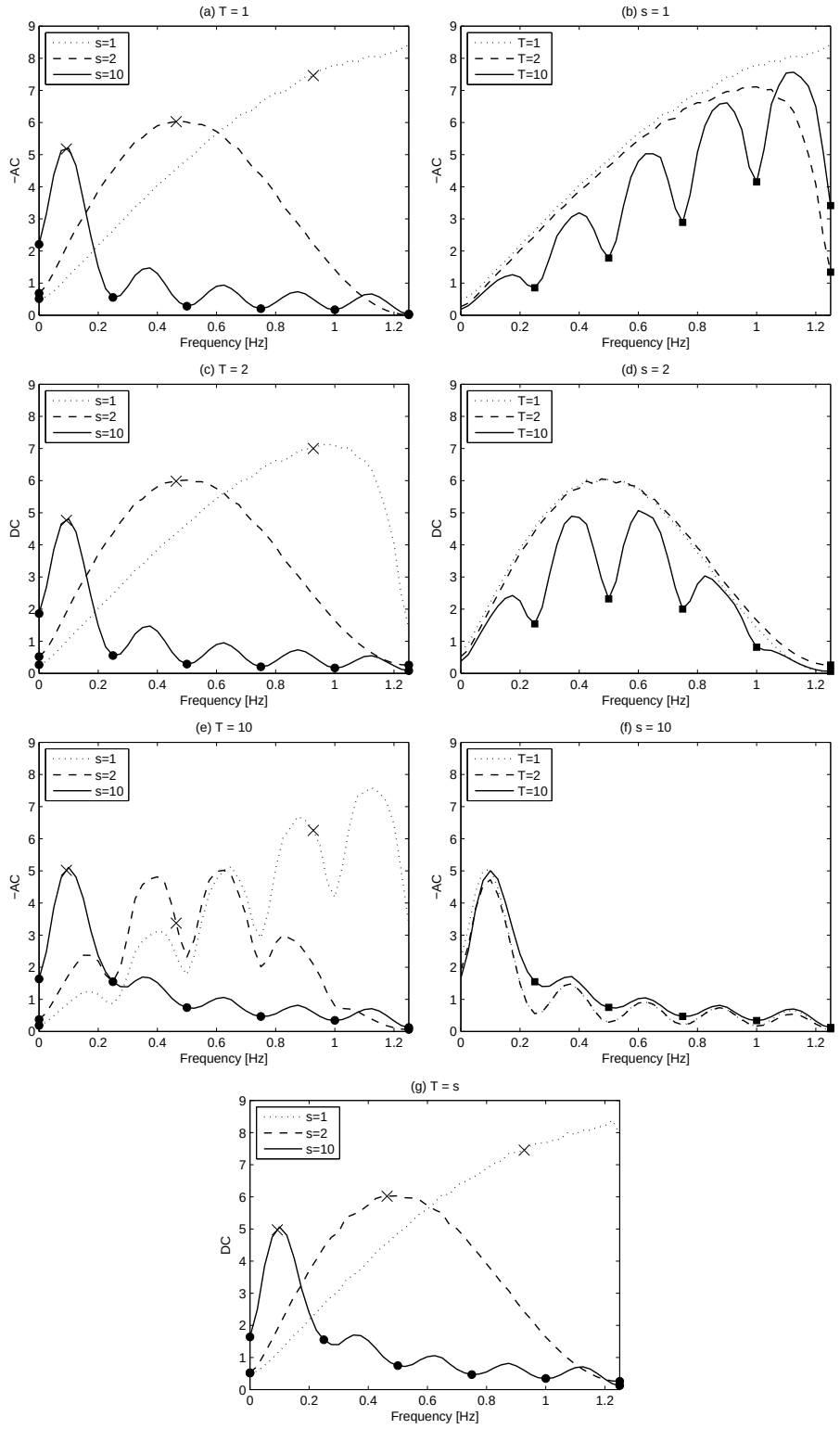

Figure 5.3: Bunch of examples of -AC and DC computed on a 2^{nd} order AR model, when varying T and s. The black circle indicates the zeros of the high pass filter $H_s(z) = \frac{1}{2s}\sum_{i=0}^{s-1} z^{-i} - \frac{1}{2s}\sum_{i=0}^{s-1} z^{-i-s}$. The black square points the zeros of the low-pass filter $H_T(z) = \frac{1}{T}\sum_{i=0}^{T-1} z^{-i}$ (FIR filter of order $T-1$). The sign $\times$ marks the frequency to which AC/DC should be more sensitive, as predicted theoretically by $0.371 f_s/s$ Hz (please note that in [110] the formula was derived for $s = T$).

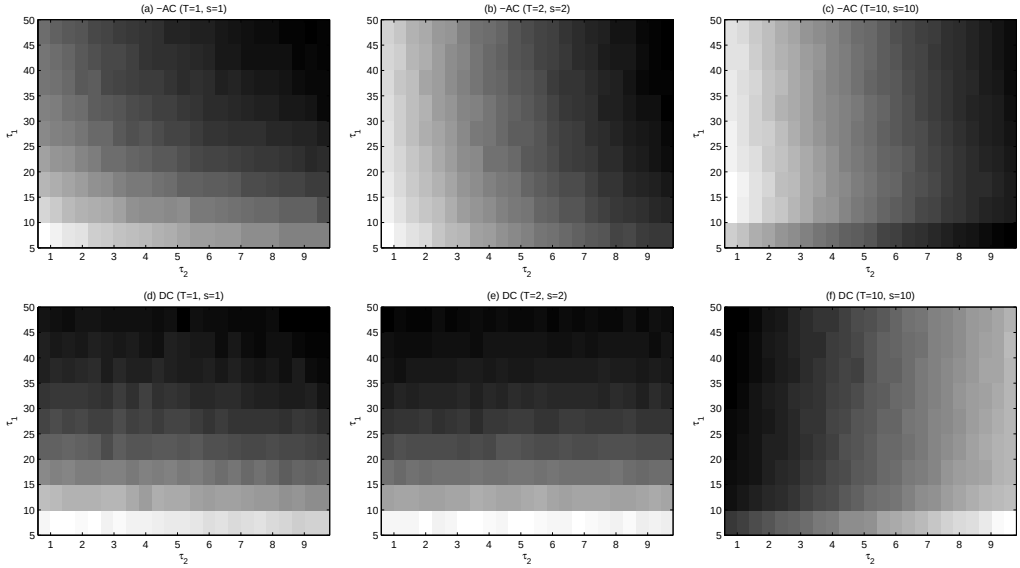

Figure 5.4: Values of -AC and DC for sawtooth-like signals for $T = s$, when varying the time-constants τ_1 and τ_2. For display purposes, values were rescaled in the interval 0 (black) to 1 (white).

by eq. (5.2) are predominant (fig. 5.3f) and changing T only affects frequencies in the neighborhoods of the zeros of the low-pass filter applied on both side of eq. (5.1). Second, no relevant differences were detected between -AC and DC for any values of s and T (fig. 5.3d and 5.3e). The latter findings were quantitatively confirmed on higher order models, where the mean values of -AC and DC were not statistically different within the same AR model (*t*-test, $p < 0.05$). However, AC (and DC) differed between models for a large range of $s = T$ values (see fig. 5.5 for an example).

5.2.2.2 SAWTOOTH-LIKE HEART RATE TREND

Notwithstanding AC and DC resulted practically identical on AR models in sec. 5.2.2.1, -AC and DC clearly differed when using sawtooth-like signals (fig. 5.4) with asymmetric trends. Indeed, both capacities varied independently, and DC was modulated by τ_1, which determines the growing trends (the "decelerating" part of the series) and, on the opposite, AC by τ_2 (the time-constant which dictates the "accelerations" in the sequence).

However, when employing small values of T, while DC was largely independent from τ_2 (fig. 5.4d and 5.4e), AC was also slightly dependent on τ_1 (fig. 5.4a and 5.4b). This is due to the fact that for $\tau_1 \gg T$, simply due to short erratic fluctuations, AC anchor points were selected also on the growing trends. On the other hand, for larger values of T, the number of points in the decaying trends was comparable to T, reducing the number of DC anchor points close to the transitions (and viceversa, increasing the number of AC anchor points). This resulted in an increased dependence of DC on τ_2 (fig. 5.4f).

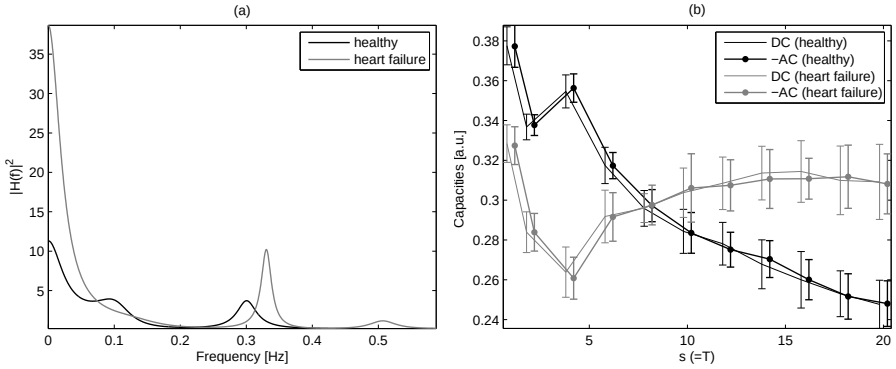

Figure 5.5: The influence of the ANS on AC/DC ($T = s$) is shown. First, the squared frequency responses of the AR model fitted on a healthy and heart failure subjects are shown in panel a). Second, the mean and the standard deviation of -AC/DC values computed on such AR models (black=healthy and grey=heart failure) are plotted on panel b). No statistical significant differences between -AC and DC were found for both AR models.

5.2.3 CONCLUSION OF THE SYNTHETIC SIMULATIONS

The value of s, more than T, determines the frequency band (centered around $f = 0.371 f_s/s$) of the oscillations which lead to larger AC/DC values, at a fixed signal's power. On the other hand, the value of T plays a major role in the selection of the anchor points, and having a low pass effect on the time series, it should be smaller than the average time-constant of the trends of interest (*e.g.*, τ_1 and τ_2 in fig. 5.4).

Moreover, a difference between the values of -AC and DC does not depend on the shape of the power spectrum, which is unchanged after time-reversal of the series (the anchor points of AC become those of DC). In fact, -AC and DC did not differ in AR models with largely different spectral content.

A difference between the two capacities was found only when asymmetries in time-constants of growing and decaying trends were present. Hence, AC and DC do not simply reflect the change in power of selected frequency bands contained in the series. On the contrary, they are strictly related to asymmetries present in the time series, and so they might quantify different underlying regulatory mechanisms. Indeed, Bauer *et al.* [51] showed that the predictive value of DC was higher than that of AC in the stratification of risk of death in post-MI patients.

Of minor relevance, the simulations also confirmed that L should be larger than the length of the period of the slowest oscillation of interest, and AC/DC are linearly dependent on the power of the signal.

One limitation of the study was that we only used simulated series to study the effects of T and s on AC/DC. In the Bauer's study [51], the optimal results was obtained for $s = T + 1$. Therefore, from an application point of view, it is not clear if the selection of s and T should be separated, and preliminary tests might be of help in each specific application.

5.3 REAL DATA VALIDATION

In this section, we applied the PRSA technique for the calculation of the acceleration and deceleration capacities on the inter-time beat series (RR) collected from an *in*-vivo near-term pregnant sheep model. Briefly, each sheep fetus has been led to hypoxia and acidemia by means of umbilical cord occlusion. Indeed, the occlusions produce a lack of oxygen and an autonomic response. The hypothesis of this work was that AC/DC can be sensitive to different levels of hypoxia and acidemia. This work was the first validation of AC/DC on an *in*-vivo animal model [90, 112, 113, 114].

5.3.1 CLINICAL INTRODUCTION

The labor exposes the fetus to repetitive transient hypoxic stress, *i.e.*, lack of oxygen, that can result in neurological permanent damages and death. Monitoring of the fetal wellbeing or distress are thus of crucial importance to timely identify hypoxia and to avoid acidemia.

Fetal heart rate (fHR) analysis by cardiotocogram (CTG) is widely used in clinical practice for fetal surveillance during labor. However, it is characterized by high sensitivity but low specificity; in fact, its role in decreasing perinatal mortality or cerebral palsy, despite increase in the rate of deliveries, is still matter of investigation [115]. Other screening techniques have been proven to be effective in reducing the fetal distress. The analysis of ST-waveforms on fetal electrocardiograms (fECG) reduces the number of instrumental vaginal deliveries for fetal complications [116]. Nevertheless, they do not solve the issue of fetal acidemia detection [117].

Another way to assess the fetal wellbeing is the direct measurement of pH or lactate concentration during partum by fetal scalp sampling. This procedure is not universally accepted as a standard of care, and, occasionally, may lead to complications [118]. Hence, further advances in fetal monitoring are needed to timely identify fetal hypoxia and acidemia.

Power spectral analysis has been extensively used as a method to quantify HR variability. When applied to fetal HR (fHR) series, several studies have proven that changes in the power spectrum are related to fetal hypoxia and/or acidemia during labor [13, 14, 16]. The variability of the fetal heart rate is strongly influenced by perturbations carried by the ANS regulation and the mother-fetus interaction. Moreover, the phase desynchronizations due to maternal uterine contractions, ventricular ectopic beats, miss-detected beats and signal losses determines a quasi-periodic behavior that limits the application of spectral analysis [119]. In this context, PRSA and AC/DC could be a reliable tool for a more robust estimate of the sympatho/vagal modulation of the ANS.

The aim of the study was to determine changes in AC and DC in response to fetal hypoxia and acidemia, and to evaluate their correlation with acid-base biomarkers. An *in*-vivo near-term pregnant sheep model was used for the assessment. For PRSA analysis, either the whole fRR signal was considered or the segments free of FHR

decelerations imposed by UCOs. Moreover, we investigated on which ranges of the PRSA's parameters were maximally correlated with the acid-base biomarkers.

5.3.2 ANIMAL MODEL

Nine near term pregnant sheep were employed as *in*-vivo model. Animal care followed the guidelines of the Canadian Council on Animal Care and was approved by the University of Western Ontario Council on Animal Care. The dataset was previously described and analyzed [120, 121].

Briefly, after a period of rest (BASELINE), a 1-minute periodical mechanical compression of the ovine fetus' umbilical cord was continuously alternated with a 1.5 minutes of recovery. Three levels of occlusion strength, from partial to complete, were designed: mild (MILD, 60 minutes), moderate (MODERATE, 60 minutes) and complete (SEVERE, 2 hours or until $pH < 7.00$ was reached). Results on these and additional animal models are reported in [120, 121, 122, 123].

Electrodes implanted into the left supra-scapular muscles, in the muscles of the right shoulder, and in the cartilage of the sternum of the fetus were used to measure the ECG which was sampled at 1000 Hz. Fetal blood samples were collected every 20 minutes to quantify the values of pH, lactate and base deficit (hereafter referred to as "biomarkers"). The severe phase of UCOs was stopped when the pH dropped below 7. Then, a recovery phase (RECOVERY) concluded the protocol.

fECGs were automatically analyzed to obtain the sequence of fetal RR intervals (fRR). Due to the long time span over which the data were collected, heart beat misdetections were common, especially during the umbilical compression. We considered suitable for further analysis only those sheep (7 out of 9) which had more than 90% of correctly located beats during MODERATE and SEVERE phases (gaps in the series were less than 10% of the total time).

5.3.3 PREPROCESSING

Fetal RR intervals greater than 1500 ms (40 bpm) were labeled as artifacts and substituted with an equivalent number of beats (calculated dividing the length of each artifact by the median of the 20 nearby fRR samples). These reconstructed samples were not used as anchor points in the PRSA analysis; however they contributed to the selection of nearby anchor points. Furthermore, each fRR interval that exceeded the preceding one by more than 20% was excluded from the anchor points' lists.

5.3.4 PROTOCOL OF THE STUDY

We analyzed fRR series obtained during the last 30 minutes of each UCO phase. The rationale for this choice was that the hypoxic levels induced by UCOs were maximal within the last part of each stimulation. Consequently, time-matched biomarkers' values were those measured from the last blood sample in each UCO phase.

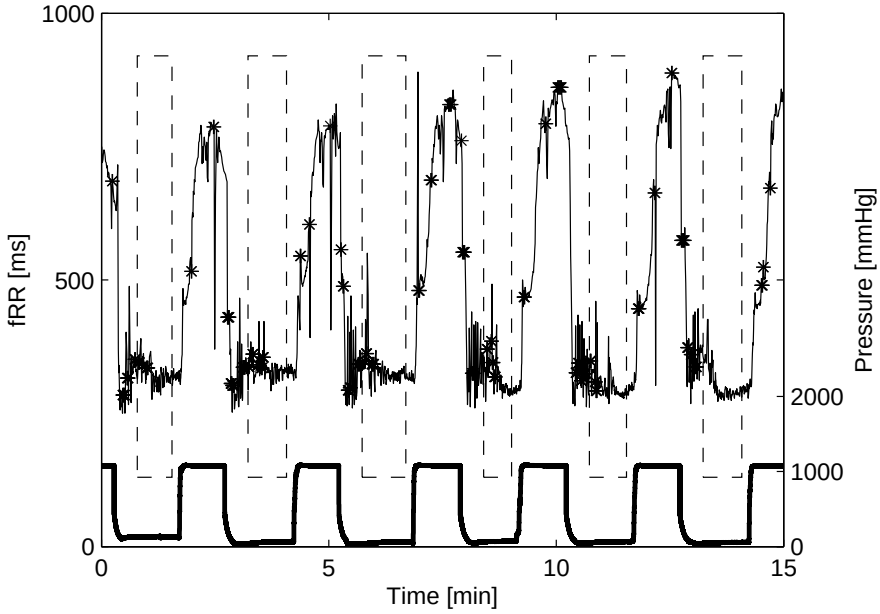

Figure 5.6: Example of fRR series and umbilical cord occlusions pressure signal (bottom bold line). Dashed boxes emphasize stable fRR intervals (without artifacts and UCO-induced decelerations). Black stars mark artifacts or reconstructed fRR samples, excluded from being anchor points in the PRSA analysis.

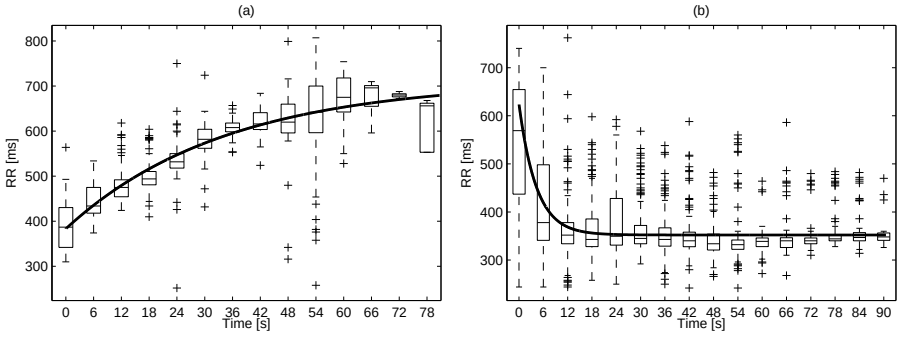

Figure 5.7: Example of fRR changes during cord occlusion and subsequent recovery. Panel (a): fRR during mechanical cord occlusion. The data belongs to the fetus of sheep #3 (tab. 5.1). Panel (b): fRR during recovery after UCO for the same case. Boxplots summarize the values of fRR at a given time distance from the occlusion (or its release). The model prediction is reported with a bold line. The vertical lines delimit the "whiskers" and the + mark the outliers.

AC and DC were determined independently for each of the UCO phases by PRSA analysis. We checked that more than 150 anchor points were available in each UCO phase. The computation was performed for values of T in the range $1-50$ with $L = 100$. The correlation between AC/DC and biomarkers' values was assessed by Spearman's correlation coefficient ($p < 0.05$ was considered significant).

UCO alters significantly the fHR series (fig. 5.6), and the influence of fHR on AC/DC is still matter of investigation. For this reason, a second PRSA analysis was performed after excluding fHR decelerations due to UCOs (hereafter referred as macro oscillations). "Stable" fHR intervals employed were located using the pressure signal applied

Table 5.1: Median values and interquartile ranges (IR) of pH, lactate and base deficit in each protocol phase.

Sheep	τ_{stim}	τ_{rec}
#1	9.63	6.46
#2	46.17	5.22
#3	34.56	4.30
#4	14.22	3.38
#5	34.65	7.88
#6	12.46	4.36
#7	11.76	5.61
Mean	23.35	5.32
Median	14.22	5.22
IR	12.11 – 34.61	4.33 – 6.03

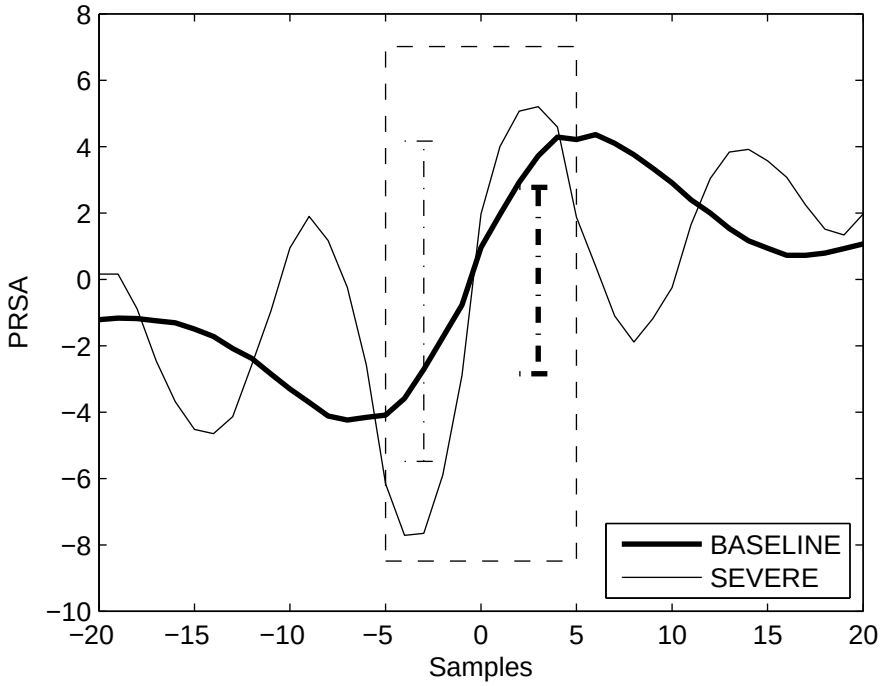

Figure 5.8: PRSA curve (DC) for a single case during BASELINE (bold line) and SEVERE UCO (PRSA's mean value was removed). The analysis was performed on stable fRR intervals. The dashed box emphasizes the samples used for computing DC (T = 5). Vertical dotted bars depict DC in the two cases considered.

on the umbilical cord during occlusion (fig. 5.6). At the beginning of each occlusion, fRR decreased progressively to quickly recover when pressure was released. The time

constants of the fRR during SEVERE cord occlusion ("stim") and recovery ("rec") were estimated, for each sheep, by fitting the exponential model:

$$\begin{aligned} RR_{stim}(t) &= A(1 - e^{-\frac{t}{\tau_{stim}}}) + B \\ RR_{rec}(t) &= Ce^{-\frac{t}{\tau_{rec}}} + D \end{aligned} \tag{5.4}$$

where τ_{stim} and τ_{rec} are two time constants (A, B, C and D are scalars necessary for the fitting but not further considered in this study). Levenberg-Marquardt least-square algorithm was used to estimate the parameters of the model for each sheep (median $R^2 > 0.9$). An example is reported in fig. 5.7 while tab. 5.1 lists the values of τ_{stim} and τ_{rec}. The two sets of time constants were largely different ($p < 0.05$, paired Wilcoxon signed rank test) suggesting that the recovery of the HR is far quicker than the onset of the deceleration.

Table 5.2: Median values of pH, lactate and base deficit according to protocol phases. Interquartile ranges are reported within brackets.

	BASELINE	MILD	MODERATE	SEVERE
pH	7.34(7.34, 7.37)	7.33(7.31, 7.34)	7.28(7.24, 7.30)	6.98(6.96, 7.07)
Lactate	1.60(1.33, 1.85)	1.65(1.40, 2.05)	3.80(2.68, 4.60)	11.40(5.20, 12.43)
Base deficit	1.08(0.31, 3.28)	0.29(−2.10, 1.06)	−2.46(−3.85, −1.17)	−14.07(−15.34, −12.64)

We considered stable (free from fHR decelerations) those intervals spanning 30 s after the end of each occlusion and ending at the beginning of the next one. The value of 30 s was selected to be larger than 3 times the longest recovery time, *i.e.*, $\tau_{rec} = 8$ s, so that fRR is substantially back to the baseline value. By definition, stable baseline intervals between decelerations were short (at most 1 minute each once removed artifacts): they were concatenated to explore larger value of T.

In conclusion, for each UCO phase two sets of AC/DC values were obtained: 1) from the entire fRR series (entire fRR); and 2) from stable baseline and free of FHR decelerations fRR intervals extracted from the fRR series and then concatenated (stable fRR). Two examples of PRSA curves are shown in fig. 5.8.

A paired Wilcoxon signed rank test was used to compare AC/DC values between: BASELINE and MILD; MILD and MODERATE; MODERATE and SEVERE. A Bonferroni correction for multiple comparisons was applied. A non-parametric test was preferred because of the small number of samples.

5.3.5 RESULTS

Table 5.2 contains the values of the biomarkers (pH, lactate and base deficit) for each protocol phase. As expected from the protocol's design, there was a trend from BASELINE to SEVERE UCOs.

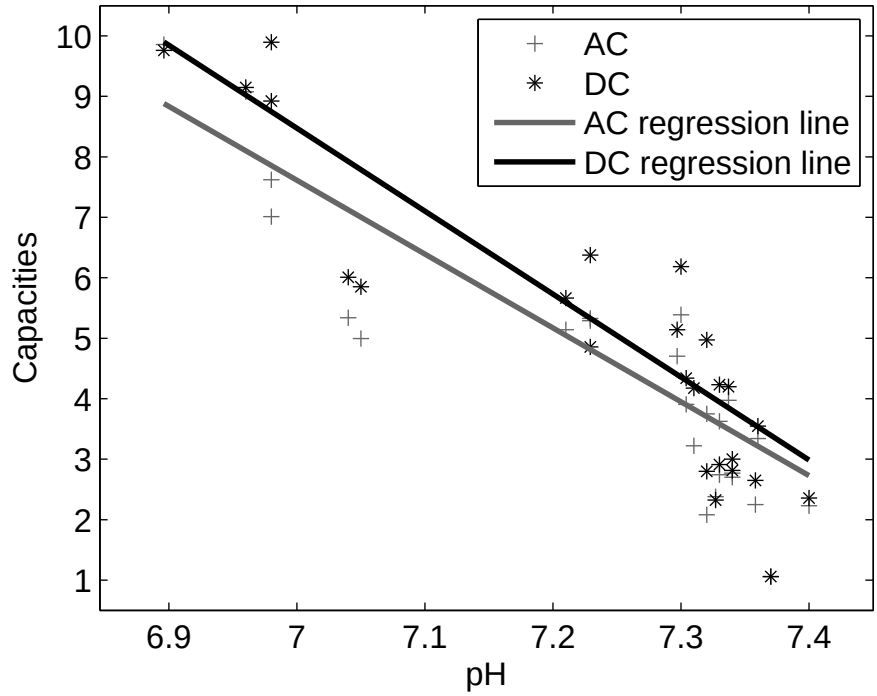

Figure 5.9: Relationship between AC and DC with pH for T = 4 (entire fRR series). The regression lines are also shown.

5.3.5.1 AC AND DC CHANGE DURING PROTOCOL PHASES

Values of AC and DC followed a similar growing trend from BASELINE to SEVERE UCOs. Table 5.3 reports median AC and DC values for each protocol phase and for a few T values (PRSA was computed on the entire fRR signal). Differences between phases varied according to the value of T used. The list of T values for which a statistically significant difference was found between successive phases ($p < 0.05$) is contained in tab. 5.4. Summarizing, as the hypoxic-acidemia progressed, DC (for T = 2 to 5) and AC (for T = 1 to 3) were different between MILD and MODERATE and then between MODERATE and SEVERE. However, MILD phase was not distinguishable from BASELINE. Parameters computed with higher values of T were different between MILD and MODERATE only.

When repeated on stable fRR intervals, the results were confirmed but weaker, as reported in tab. 5.5 and tab. 5.6. Specifically, while SEVERE was distinguishable from MODERATE for T in the range 3 to 5, MILD and MODERATE were significantly different only for large values of T. However, for $T > 25$, anchor points were selected using fRR samples coming from two consecutive recovery periods, and, thus, the results were less reliable.

Furthermore, AC/DC values, computed on a window of 5 minutes immediately after the end of the SEVERE phase, were not statistically different from those during the BASELINE phase ($p > 0.05$).

Table 5.3: AC and DC absolute median values (in ms) when considering the entire signal (including UCO-induced fHR decelerations). Interquartile ranges are reported within brackets. Any AC or DC value (for MILD, MODERATE and SEVERE) is statistically different from the corresponding one in tab 5.5 ($p < 0.05$).

AC	BASELINE	MILD	MODERATE	SEVERE
$T = 2$	2.30(1.55, 2.51)	1.92(1.56, 2.26)	4.32(3.40, 6.14)	6.57(4.21, 8.18)
$T = 4$	2.77(2.35, 3.56)	2.56(2.25, 3.91)	5.33(4.85, 7.12)	7.01(5.19, 8.71)
$T = 6$	3.27(2.99, 3.93)	3.14 (2.78, 4.45)	6.13(5.89, 7.77)	6.84(6.30, 8.45)
$T = 10$	4.07(3.60, 4.24)	4.06(3.59, 4.82)	8.09(7.07, 8.82)	6.40(5.82, 9.02)
$T = 20$	4.58(4.12, 4.66)	5.04(4.75, 5.50)	10.92(8.96, 11.21)	7.81(7.02, 10.60)
DC	BASELINE	MILD	MODERATE	SEVERE
$T = 2$	2.78(1.93, 3.79)	2.26(2.05, 3.19)	4.91(3.72, 5.85)	7.21(4.36, 7.55)
$T = 4$	3.00(2.47, 4.06)	2.86(2.65, 4.20)	6.19(4.93, 7.48)	8.92(5.89, 9.61)
$T = 6$	3.29(2.98, 4.42)	3.49(3.26, 4.60)	6.62(6.07, 8.45)	9.55(7.56, 10.14)
$T = 10$	3.74(3.46, 4.79)	4.44(4.19, 5.18)	7.69(7.37, 9.86)	10.40(9.30, 10.82)
$T = 20$	4.21(3.74, 4.96)	5.61(5.48, 5.88)	9.45(8.87, 10.22)	12.24(9.65, 14.66)

Table 5.4: Ranges of T in which a significant difference between two phases was found (Wilcoxon signed rank test, $p < 0.05$). PRSA was performed on the entire signal (including UCO-induced FHR decelerations).

	BASELINE	MILD	MODERATE	SEVERE
BASELINE	-	none	-	-
MILD	-	-	any	-
MODERATE	-	-	-	$T \leqslant 3$(AC); $2 \leqslant T \leqslant 5$(DC)

Finally, during UCO the values of AC/DC computed on the entire signals (tab. 5.3) were significantly different from those obtained on stable series (tab. 5.5), and this was true for each value of T ($p < 0.05$).

Comparing the values in tab. 5.2 with those in tab. 5.3, although the decelerations imposed by UCOs are low frequency variations of the fHR, it is clear that the PRSA is still influenced by them. In fact, for any value of T (even the smaller ones) AC (or DC) computed on the entire fRR series and on stable fRR intervals were different ($p < 0.05$).

5.3.5.2 CORRELATIONS WITH ACID BASE BALANCE

A significant Spearman's correlation coefficient between AC/DC (computed on the entire fRR series) and each biomarker of acid base balance was found for a large range of T values (fig. 5.9 and fig. 5.10). However, maximal correlation ($0.40 < \|\rho\| < 0.90$; $p < 0.05$) was for T in the interval 2 to 6, and was stronger for DC. Both AC and DC

Table 5.5: AC and DC absolute median values (in ms) when considering stable (concatenated baseline segments free of FHR decelerations) fRR intervals. Interquartile ranges are reported within brackets. Any AC or DC value (for MILD, MODERATE and SEVERE) is statistically different from the corresponding one in tab. 5.3 ($p < 0.05$).

AC	BASELINE	MILD	MODERATE	SEVERE
$T = 2$	2.31(1.55, 2.53)	1.61(1.17, 2.11)	2.18(1.75, 2.85)	3.99(2.10, 4.34)
$T = 4$	2.77(2.36, 3.52)	2.14(1.68, 2.67)	2.79(2.47, 3.58)	4.45(3.10, 5.29)
$T = 6$	3.26(3.00, 3.87)	2.49(2.12, 2.96)	3.41(2.95, 4.20)	4.81(3.49, 5.22)
$T = 10$	4.07(3.61, 4.24)	3.01(2.46, 3.48)	4.31(3.31, 5.46)	3.99(3.84, 5.26)
$T = 20$	4.53(4.13, 4.68)	3.34(2.73, 4.41)	5.43(3.92, 6.25)	5.36(4.42, 5.94)
DC	BASELINE	MILD	MODERATE	SEVERE
$T = 2$	2.79(1.95, 3.78)	2.00(1.54, 2.95)	2.68(2.28, 3.13)	4.18(2.82, 4.44)
$T = 4$	2.99(2.50, 4.03)	2.37(1.85, 2.96)	3.11(2.89, 4.10)	4.87(3.57, 5.25)
$T = 6$	3.27(3.01, 4.36)	2.79(2.37, 3.26)	3.61(3.28, 5.13)	4.81(3.63, 6.11)
$T = 10$	3.73(3.49, 4.70)	3.22(2.81, 4.11)	4.60(3.67, 6.48)	4.83(4.49, 6.29)
$T = 20$	4.20(3.77, 4.86)	3.82(3.55, 5.10)	5.55(4.53, 7.59)	6.35(4.99, 7.45)

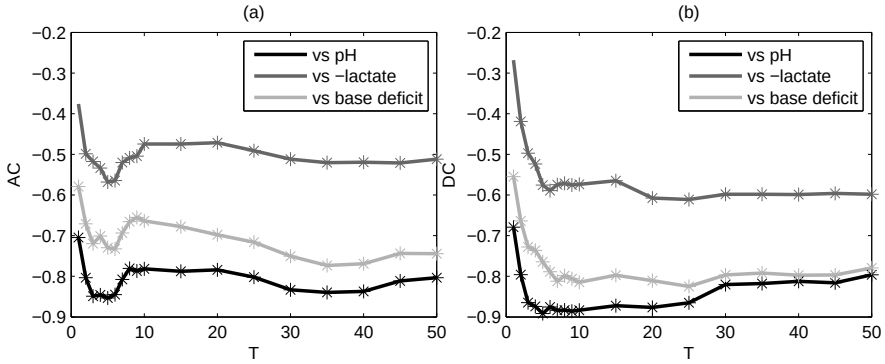

Figure 5.10: Spearman's correlation coefficients between AC (a) and DC (b) and each acid-base balance biomarker. PRSA was performed on the entire fRR series. Stars refer to significant p values ($p < 0.05$). Lactate values were multiplied by -1.

correlated stronger to pH and base deficit, than to lactate concentration. For instance, considering $T = 4$, we found a negative correlation among AC (its absolute value) and pH ($\rho = -0.85$; $p < 0.05$), base deficit ($\rho = -0.70$; $p < 0.05$), and a positive correlation with lactate ($\rho = 0.53$; $p < 0.05$).

Similarly, we found a negative correlation among DC and pH ($\rho = -0.87$; $p < 0.05$), base deficit ($\rho = -0.74$; $p < 0.05$), and a positive correlation with lactate ($\rho = 0.52$; $p < 0.05$).

When excluding decelerations imposed by UCOs, a significant correlation was found for a narrower range of T values (fig. 5.11), the range was wider for DC than AC). However, these values matched those for which the correlation coefficients were maximal in the previous analysis.

Table 5.6: Ranges of T in which a significant difference between two phases was found (Wilcoxon signed rank test, $p < 0.05$). PRSA was performed on stable (concatenated baseline segments and free of FHR decelerations) fRR intervals.

	BASELINE	MILD	MODERATE	SEVERE
BASELINE	-	none	-	-
MILD	-	-	$T = 50$ (AC); $T \geqslant 45$ (DC)	-
MODERATE	-	-	-	$3 \leqslant T \leqslant 5$ (AC); $4 \leqslant T \leqslant 5$ (DC)

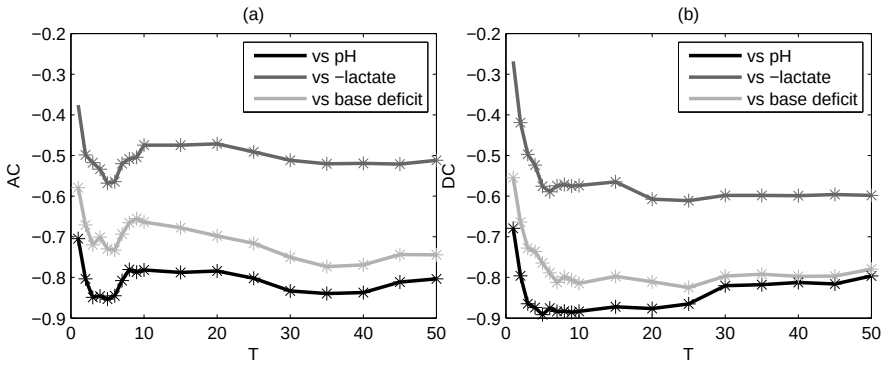

Figure 5.11: Spearman's correlation coefficients between AC (a) and DC (b) and each acid-base balance biomarker. PRSA was performed on stable fRR intervals. Stars refer to significant p values ($p < 0.05$). Lactate values were multiplied by -1.

5.3.6 DISCUSSION

The principal findings of the study are: 1) AC and DC increase with worsening of acidemia; 2) AC and DC correlate to acid base balance observed at different phases of hypoxic-acidemia; 3) PRSA computed with $T = 2$ to 5 best enhances differences among protocol phases (this is particularly true for SEVERE cord occlusions), resulting in the highest correlation between AC or DC with biomarkers; and 4) considering only stable fRR segments or the entire fRR series led to different results (AC/DC values obtained on stable fRR segments were smaller on average). Hence, fHR decelerations, even if composed by low frequency components, induce changes in the PRSA series and, consequently, in AC and DC.

5.3.6.1 AC AND DC INCREASE WITH WORSENING OF ACIDEMIA

AC and DC identify different behavior of the fHR during acceleration and deceleration, respectively. Nevertheless, it would be too simplistic to consider AC only as an expression of sympathetic modulation and DC as an expression of parasympathetic modulation. Rather, both AC and DC result from the interaction of parasympathetic and sympathetic component, and represent an integration of several input signals such as chemoreceptor, baroreceptor and others. The two components of the autonomic ner-

vous system (ANS) operate at different frequency scales: sympathetic component in low frequency domain, while parasympathetic both in low and high frequency domain, respectively. In PRSA computation, the $s = T$ parameter determines an upper frequency limit for the periodicities that mostly influence AC and DC [48]. For $T = 1$ high frequencies dominate the computation. At contrary, increasing values of T will progressively also emphasize the contribution of low frequency components.

When looking at the absolute values of AC and DC we observed a clear increasing trend with worsening acidemia. Indeed, during SEVERE UCOs (*i.e.*, severe acidemia), the AC and DC were maximal with respect to BASELINE. This trend was present when analyzing the whole fRR series and for a large range of T values suggesting the activation of both sympathetic and parasympathetic component during progressive acidemia.

However, only a smaller range of T ($2 \leqslant T \leqslant 5$) was able to differentiate MODERATE vs SEVERE phase. The same was true for $3 \leqslant T \leqslant 5$ when excluding fHR decelerations. This would suggest that, for higher degree of acidemia, the frequencies dominated by parasympathetic component become predominant. These findings are in agreement with other reports that evaluated ANS response to hypoxia, but with different methodologies: 1) Frasch *et al.*, in the same population of 7 near-term pregnant sheep employed for this work, reported that the root mean square of successive differences (RMSSD, a time-domain index mainly influenced by the vagal activity [124]) has the most pronounced changes during acidemia [122]; 2) Siira *et al.* found that in an acute phase of hypoxia, without acidemia, there is an activation of sympathetic system, while, when acidemia occurs, the vagal influence increases [13].

The activation of ANS by initial and acute hypoxia most likely constitutes a first line adaptive response, and results in a more pronounced fHR modulation and a larger cardio-vascular response. Indeed, in experiments on fetal lambs, acute fetal hypoxia led to increased fHR variability representing a sign of adequate fetal compensatory response [125]. Moreover, the predominant involvement of vagal tone has been associated to a more efficient modulation of ANS [126]. In fact, in the presence of acute hypoxia, the reduction in fHR (*i.e.*, deceleration) is thought to be protective for the fetus, because it reduces myocardial work and oxygen consumption [127], and is mediated by the chemoreceptors via the parasympathetic branch. Nevertheless, if there is a prolonged hypoxic insult and overwhelming acidemia, parasympathetic activity decreases [13], causing reduced fHR variability [128]. In fact, when the vagal regulation becomes inadequate, some of the adaptive mechanisms (such as chemoreceptor-mediated circulatory adaptation) might fail causing fetal brain damage, and ultimately fetal death.

Interestingly, our data did not show the final fall in parasympathetic activity before the pH reached the predefined threshold, most likely due to the acute nature of the insult. This was confirmed by the rapid recovery (tab. 5.1 and fig. 5.7) that each animal showed both for acid-base balance and PRSA parameters [120].

5.3.6.2 AC AND DC CORRELATE WITH ACID BASE BALANCE

We found that AC and DC correlate to the biomarkers of acidemia, and this correlation is significant both for fRR series that include and exclude FHR decelerations. Interestingly, the correlation was stronger for pH and base deficit, and to a lesser extent for lactate concentration. This finding can be explained by the fact that both pH and base deficit are strong stimulators of chemoreceptors which are highly sensitive to the presence of hypoxemia, and, consequently, influence FHR modulation [129].

Moreover, we found that the correlation with acidemia was maximal for low values of T. This would suggest that, in the presence of acute hypoxic insult, the low frequencies dominated by parasympathetic branch are more responsive to the changes of acid base balance. Several studies evaluated the correlation between fHR variability assessed by spectral analysis and acid base balance, either during labor [13], or at birth [14, 15]. Although, all studies confirmed that hypoxia and acidemia have a direct effect on fHR variability, and thus on ANS, it is difficult to derive a common mechanism for all studies because of profound methodological differences [16]. Nevertheless, our findings are in agreement with those by Siira *et al.*, who found a correlation between high frequency bands at power spectral analysis of fHR variability and pH obtained by fetal scalp blood sampling during labor [13].

5.3.6.3 CHANGES IN AC AND DC VARYING THE PARAMETER T

The significance of the parameter T has been explored in adult cardiology, and a T of $1-2$ has been found as the best value [49] (when $T = 1$, $s = 2$ might be preferred [51]). Although some studies applied PRSA to fHR [50, 108, 109], the impact of changing T when PRSA is applied to FHR has not been reported. We found that T value in interval $2-5$ best enhances the differences between progressive cord occlusion phases (worsening acidemia).

Similarly, when evaluating the correlation with acid-base biomarkers, the best correlation was observed for T value in the range 2 to 6. Very recent analysis in cardiac patients also showed that application of a larger T makes PRSA more robust to artifacts and noise [130]. Thus, we suggest this time scale for an effective computation of PRSA analysis, when detecting hypoxic-acidemic events in laboring fetuses. However, the small sample size used requires a validation in a larger study.

5.3.6.4 EXCLUDING FHR DECELERATIONS IN PRSA COMPUTATION

We wanted to evaluate if there were significant differences between stable intervals of fRR series and the entire fRR series. The rationale was the fact that abrupt perturbations, such as uterine contractions, or in this case UCOs, may lead to a phase de-synchronization in the fRR series. Interestingly, we found significant differences between AC and DC computed on the entire signal or on stable fRR signal. This was true even for small values of T, hence, for high order frequencies. When interpreting these findings it has to be taken into account that: 1) the frequency content of macro oscillations is very limited (compared with those of other components of the fRR), and, therefore, should be filtered out from the series when calculating PRSA; and 2) ca-

pacity estimates should be independent from fHR decelerations when ANS regulation does not change (at least for small values of $T < 20$). However, our results showed the contrary. There could be two possible explanations. First, during UCOs, not only the mean trend of the series changes but also the beat-to-beat relationships regulated by ANS. Second, PRSA's amplitude depends on the power of the oscillatory components of the signal, and AC and DC may be influenced by severe fHR decelerations that determine changes in total spectral power.

The analysis on the stable fRR segments seems to strengthen the first explanation. Moreover, in order to address the issue of total power of the signal we computed the standard deviation of normal-to-normal intervals (SDNN, [125]), a fHR variability measure capturing all cyclic components responsible for the variability in the period of recording and strictly related to the total power of the sequence. SDNN was statistically indistinguishable between any two consecutive phases of the stable segments of fRR intervals (paired Wilcoxon signed rank test, $p > 0.05$; data not shown). Therefore, the total power cannot explain the difference in AC and DC between phases.

To summarize, we found differences in AC/DC between entire and stable fRR series, that in our data series cannot be explained by the change in total power suggesting a higher order influence of ANS on fRR series during decelerations. Which one of the two phases (*i.e.*, entire or stable fRR series) could be more valuable in a clinical scenario remains to be evaluated.

5.3.7 CONCLUSION ON REAL DATA

In conclusion, our study has shown that PRSA-based analysis of fHR variability was a sensitive tool for detecting hypoxia-induced autonomic activations. Overall, we found the evidence of ANS activation in sheep fetus exposed to acute hypoxic-acidemic insult. Such activation was more prominent at mid/high frequencies (which mostly influence PRSA in the range $3 \leqslant T \leqslant 5$), that correspond to a more relevant activation of the parasympathetic branch). Moreover, the PRSA-based measures, AC and DC, were significantly correlated with measures of acidemia with strongest correlation in a range of high frequencies. We evaluated the impact of the parameter T and we offered suggestions for its choice.

5.3.7.1 LIMITATIONS AND STRENGTHS OF THE STUDY

This is the first validation, in an *in*-vivo pregnant sheep model, of PRSA analysis of fHR to detect different acid-base states during worsening hypoxic-acidemia. Studies performed on *in*-vivo models (usually pregnant sheep) permit to simulate near-term pregnancies, and repetitive UCOs to mimic uterine contractions. Moreover, the data such as fRR series, pH, base deficit and lactate concentration were obtained directly from the fetus during the entire course of the experiment.

A limitation of the study was the small sample size. However, it was adequately powered to detect differences of DC and AC at different hypoxic phases.

5.4 CONCLUSION

In this chapter, we described our work, *i.e.*, a set of extensive numerical simulations and a preliminary validation of the acceleration and deceleration capacities, computed by PRSA.

The use of numerical simulations has provided insights into the meaning of AC/DC. Although, the computation of the PRSA contains a non-linear step, *i.e.*, the selection of anchor points, it is clear that T and s play an important role as frequency band selectors. The parameter s, more than T, acts as a high pass filter and it is primarily involved in the computation of AC and DC from the PRSA and then, AC/DC are more sensitive to it. On the other hand, the value of T imposes $T-1$ equispaced zeros in the frequency domain making some frequency bands more relevant than others. It is worth noting that the highest sensitivity of AC/DC can be predicted using the formula $0.371 f_s/s$ Hz (excluding $T = 1$ that is a particular case). Therefore, a proper combination of T and s permits to maximize the sensitivity of AC/DC in specific frequency bands. These results are preliminary confirmed by several clinical studies. For example, in the study of Bauer *et al.*, the PRSA analysis was applied to RR series of subjects after myocardial infarction [51]. The myocardial infarction is characterized to a reduced SDNN and an altered sympathovagal regulation [131, 132]. This means that the frequency band to select must be in the range influenced by the autonomic nervous system. Bauer *et al.* used a value of $s = 2$ and $T = 1$ that corresponded to a maximum sensitivity around 0.23 Hz at 75 bpm [111].

The validation study on data coming from an *in*-vivo near term pregnant sheep model has shown that PRSA analysis of fHR variability was a sensitive tool for detecting hypoxia-induced autonomic activations. We found the evidence of ANS activation in sheep fetus exposed to acute hypoxic-acidemic insult.

6

PHYSIOLOGICAL BACKGROUND

This chapter has been thought for making more understandable some algorithmical choices presented in the thesis. The real world applications considered for validating the methodologies developed are in the biomedical field and, in particular, they are related to the heart and to the analysis of electrocardiogram recordings. When not specified elsehow, information about the physiology of the heart are referred to the work of Podrid and Kowey [26].

A general and raw description on the functionality of the heart, its electrical conduction system and a few knowledges about arrhythmias will be given in this chapter.

6.1 THE HEART

6.1.1 THE PUMPS

The heart is the main organ of the cardiovascular system whose primary function is to pump blood throughout the body by means of the blood vessels.

It is composed by two different pumps. The first pump is responsible to push the oxygen-rich blood from the heart to every other tissue of the body by means of arteries, such circuit is called *systemic circulation*. The second pump receives the blood from the body, *i.e.*, blood without oxygen and nutrients, by the veins and leads it to the lungs through the *pulmonary circulation*, where it is enriched by oxygen again.

The heart is divided into four chambers, two atria and two ventricles. The left atrium and the left ventricle form the left pump responsible for the systemic circulation. The right ones belong to the pulmonary circulation.

Pumps do not communicate between each other, *i.e*, there is no direct exchange of blood. Only atrium and ventricle of the same pump exchange blood and, in addition, in just one direction: from the atrium to the ventricle. The direction of blood flow is controlled by four valves, the *atrioventricular valves*, located between the atria and the

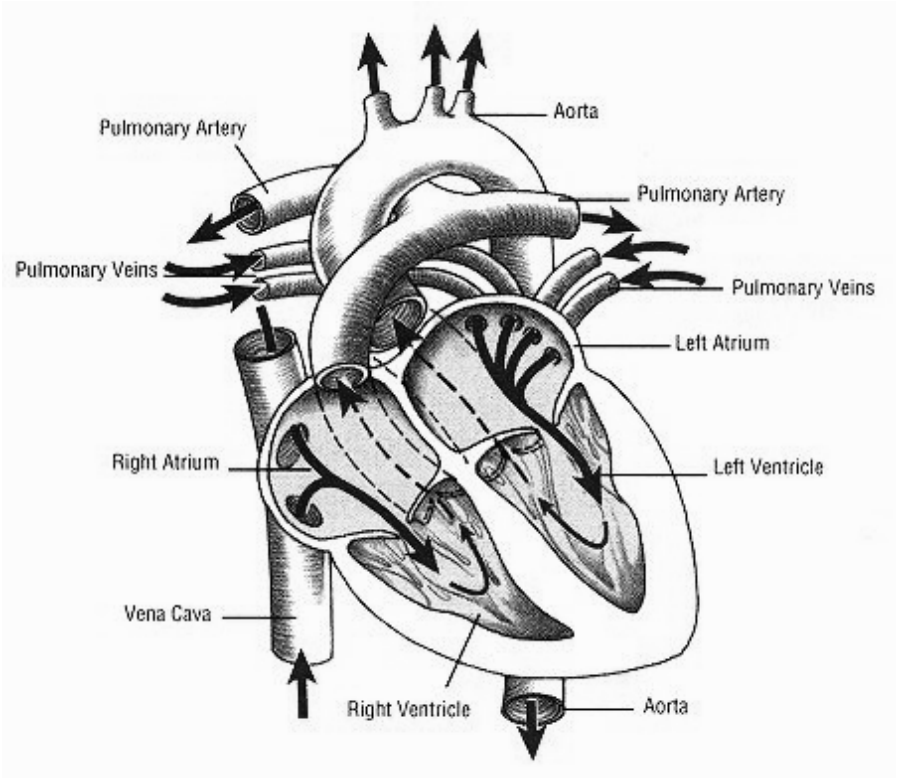

Figure 6.1: Sketch of the heart and both systemic and pulmonary circulations.

ventricles, and the *pulmonary and aortic valves*, located between the ventricles and the arteries. In such a way, blood cannot flow back in the ventricles. Figure 6.1 shows both the systemic and the pulmonary circulation as well as the four chambers and valves.

The blood without oxygen arrives through two big veins, the superior and the inferior vena cava respectively, to the right atrium. The atrium pushes such blood to the right ventricle. The right ventricle pumps the blood to the lungs through the pulmonary arteries. The typology of a blood vessel depends on the tissue on which it is composed and not on which kind of blood it carries.

The left atrium receives the oxygen-rich blood from the pulmonary veins. This blood is pushed into the left ventricle. The left ventricle, the stronger among the four chambers, pumps the blood to the rest of the circulation. To do that, it produces a high level of pressure.

Blood is pushed by means of a mechanical contraction of the heart. The alternation of contraction and resting condition, *i.e.*, systole and diastole respectively, is called cardiac cycle.

6.1.2 THE CARDIAC TISSUE AND THE ELECTRICAL EXCITABLE CELLS

The heart is located in a sac called pericardium whose main duty is to anchor it to other structures while ensuring anatomical changes due to contraction. In addition, the heart is composed of three layers of cells: the epicardium, the mid-myocardium and the endocardium. Both epicardium and endocardium serve to protect the myocardium.

In particular, the former lubricates the heart and to prevent friction, while the latter excludes the direct contact with the blood that needs to be pushed. The myocardium, in fact, is the contractile muscle responsible of the pushing. Each part of the heart is composed by different cells with different chemical and physical properties.

The contractile force produced by the myocardium is generated by electrical impulses. Indeed, the cells of the myocardium are electrically excitable. They can produce a mechanical force when an electrical impulse goes through them. Such phenomenon demonstrates that the heart tissue has a well structured electrical conduction system in which an electrical impulse propagates easily.

The electrical current responsible of the propagating impulse is generated by the flows of ions, either positive or negative charged, through the cell membrane of a cardiac cell. The cell membrane is a structured phospholipid double layer whose permit to separate ions inside the intracellular domain from those in the extracellular one. Moreover, this membrane has multiple ion channels. Ion channels are selective to a specific ion, *e.g.* Na^+, Cl^-, Ca^{2+}, K^+, etc.

Because of this selectivity, the concentration gradient, *i.e.*, spatial difference of ion concentration, and the electrical gradient, *i.e*, spatial difference in the amount of charge, equilibrate each other blocking every flow of ions and forming a constant transmembrane potential (TMP) between the intracellular domain and the extracellular one. Such electrical potential is called *resting potential* of the cells and it has a value about $-80\text{m}V$ for a cardiac cell. Figure 4.1 shows the TMP of the cardiac cells across the heart.

Once an electrical impulse stimulates a cell in resting condition, a sodium current (Na^+) flows from the extracellular domain into the cell, increasing the electrical potential up to $+20\text{m}V$. This rapid phenomenon is called "*depolarization phase*".

Afterwards, a potassium current (K^+) starts to flow outside the membrane trying to re-establish the resting condition. At the same time, the ion current related to Ca^{2+} starts to go inside the cell producing a steady-state TMP called "*plateau phase*".

Finally, the calcium current (Ca^2+) influx stops while the potassium one still goes out, leading back to the resting condition of TMP. This phase is called "*repolarization phase*".

During depolarization and plateau phases no other electrical impulses can produce a change in the TMP. That is due to the capability of the ion channels to either modify or stop the ion flux depending on the value of the TMP. Such time interval is called *absolute refractory period*. However, during repolarization, a second electrical impulse, stronger than the first one, could force a new depolarization (*relative refractory period*). Because of the absolute refractory period, the electrical impulse travels in just one direction.

The electrical excitability of the cells combined with the electrical properties of the extracellular domain permit to create ion currents outside the cell. Such currents are able to depolarize neighbor cells and so, the electrical impulse moves.

Finally, it is worth noting that systole and diastole are respectively linked with the depolarization and repolarization phase of the myocardium cells. Indeed, during depolarization, the electrical impulse which travels through the cells, produces a mechanical

contraction, *i.e.*, systole. During repolarization, the cells return back to the resting state with a progressive relaxing of the blood pressure, *i.e.*, diastole.

6.1.3 PATHWAY OF THE ELECTRICAL CONDUCTION SYSTEM

In order to produce an optimal pumping function, the heart follows a precise and organized sequence of electrical events.

The cardiac cycle starts in a mass of pacemaker cells generating spontaneously electrical impulses: they periodically depolarize themselves producing the so-called *heart rate* (HR). These cells are located in a zone of the upper part of the right atrium called *sinoatrial node* (SA).

Such electrical impulse spreads on the heart through the conduction system. In particular, the impulse reaches the *atrio-ventricular node* (AV), then goes through the *bundle of His* and finally, with the help of the *Purkinje fibers*, it depolarizes the right and the left ventricles. Such electrical circuits are a part of the electrical conduction system of the heart, with specific chemical and physical properties suitable for the transmission of electrical impulses.

Figure 6.2 shows the electrical conduction system of the heart and how the electrical impulse spreads through the whole organ.

6.1.4 THE ELECTROCARDIOGRAM

The electrocardiogram (ECG) represents and describes the electrical activity of the heart recorded by electrodes placed on the body surface.

The depolarization of the right and left atria is represented by the P wave, whereas the atrial repolarization cannot be visualized from the ECG since it is completly overlapped by the depolarization of the ventricles, *i.e.*, the QRS complex. Finally, the repolarization of the ventricles is represented by the T-wave. Figure 4.1 shows a sketch of an heart beat, including P wave, QRS complex and T-wave measured by a single electrode.

The amplitude and the shape of the heart beat depends on the position of the electrodes. In addition, they also change when considering unipolar or bipolar lead system.

In clinical routine, the standard 12 lead ECG is used for general screening. It is composed by 3 bipolar leads called *limb leads* (lead I, II and III), 3 unipolar leads called *augmented leads* (aVL, aVR and aVF) and other 6 unipolar leads called *precordial leads* (V_1, V_2, V_3, V_4, V_5 and V_6).

In particular, lead I is defined as the difference between the activity measured by the electrode on the left arm (LA) and the one on the right (RA). Lead II is defined as left leg (LL) minus the LA and lead III as LL minus RA. Because of their composition, only 2 leads are independent. Figure 6.3 shows a sketch of the positioning of the standard 12 leads.

The unipolar augmented leads are computed as the electrical potential of one limb minus the average of the remaining two. Therefore, the augmented leads are linear dependent on the limb leads.

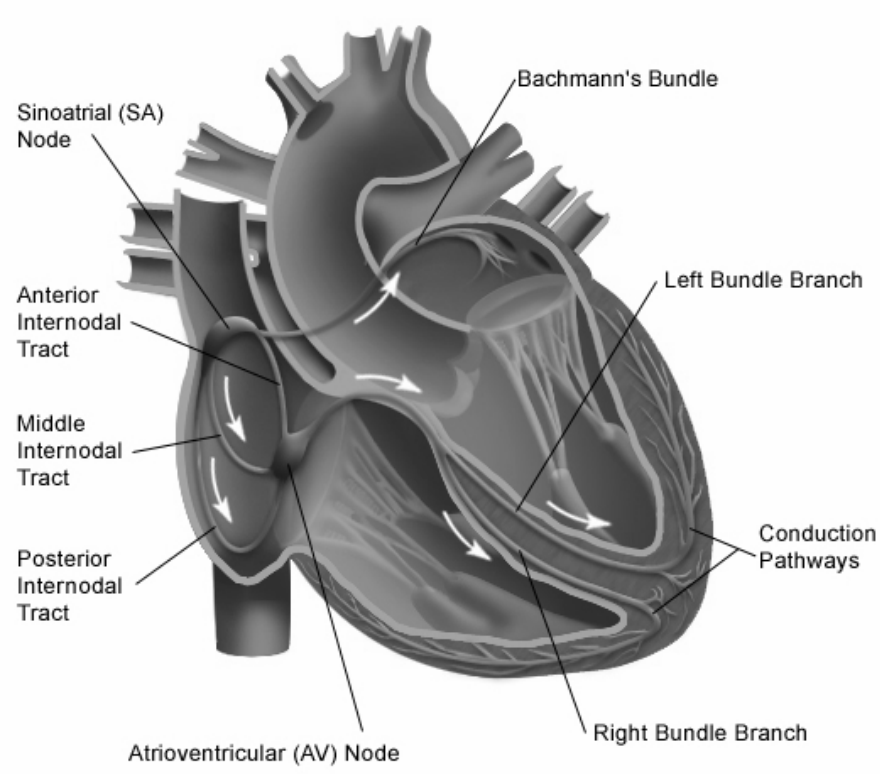

Figure 6.2: Sketch of the electrical conduction system of the heart.

The precordial leads (from V_1 to V_6) are placed on the chest. They are referred to the *Wilson's central terminal* (V_W), *i.e.*, the average of the potential measured on the limb leads.

In conclusion, all these leads permit to "visualize" the electrical activity of the heart from different point of view. Moreover, only 8 leads are independent views. The other ones can be reconstructed by means a linear combination.

6.2 ATRIAL FIBRILLATION

Atrial fibrillation (AF) is the most common cardiac arrhythmia in elderly people and it has a large economical cost for health systems [133, 134].

AF is the result of alterations of the electrical properties of the conduction system of the atrial surface. Indeed, heart failure, hypertension or dysfunction of the sinus node can alter the electrical propagation, generating extra-foci on the atrial surface capable to discharge electrical impulses independently from the sinus node. The combination of such non-normal impulses may lead to have some regions electrically self-sustained, *i.e.*, atrial chambers do not stop to be activated.

AF is clinically classified into three classes named I, II, or III Well class, in function of the degree of organization of the electrical propagation. Furthermore, AF can be paroxysmal or persistent.

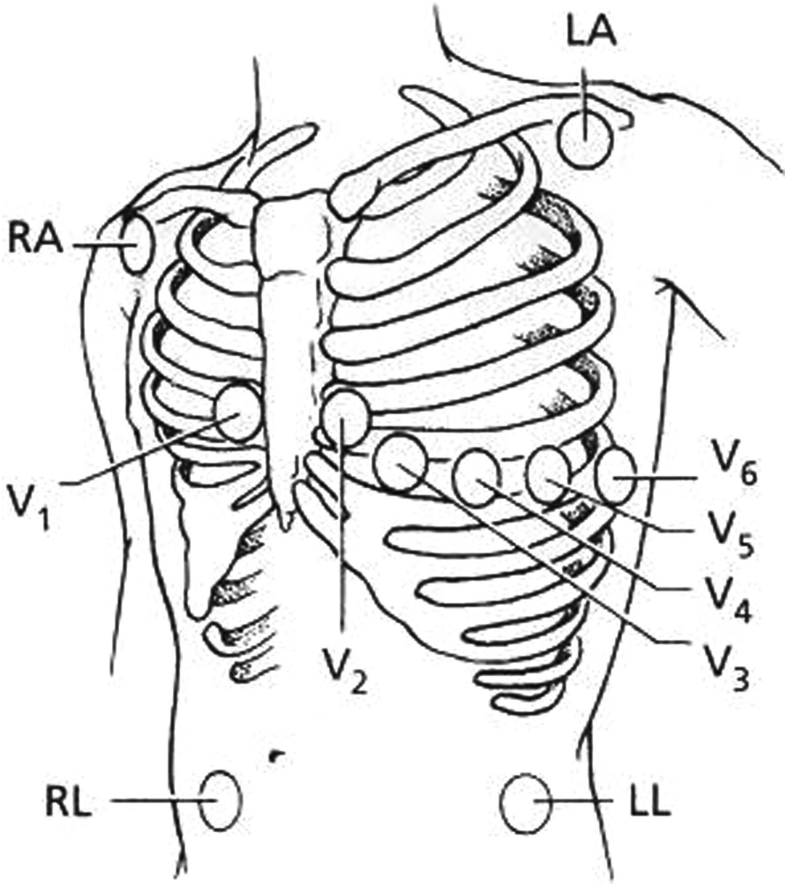

Figure 6.3: Sketch of the position of the electrodes in the standard 12 lead ECG. LA = left arm, RA = right arm, LL = left leg and RL = right leg. The precordial leads are those from V_1 to V_6.

When pharmacological or electrical cardioversion treatments [135] do not work, a surgical procedure called *ablation* is performed [134]. This technique attempts to isolate electrically those regions that are responsible for the fibrillation. Typically, when the four pulmonary veins of the left atrium are electrically isolated, the AF stops. However, in many cases, there are other sites responsible for AF.

A standard ablation treatment is performed by inserting a catheter into either the femoral or the jugular vein, up to reach the right atrium chamber. Then, the wall between the two atrium chambers is holed to reach the left one. Now, the surgeon performs a series of measurements of the electrical potential on the internal surface, *i.e.*, endocardium, in order to select the best suitable sites to be electrically isolated.

These measurements contain the atrial electrical activity (AEG), both near and far field from the electrode, and the ventricular one [79].

6.3 VENTRICULAR FIBRILLATION

Ventricular fibrillation (VF) is a dangerous cardiac arrhythmia, and it represents a cardiac event in which an uncoordinated contraction of the cardiac muscle, results in a

low blood pumping function. If it is not treated suddenly, it leads to death in a few minutes: the so-called sudden cardiac death.

Many reasons are known to be associated with the genesis of the ventricular fibrillation. Most of them are linked with alterations of the electrical properties of the ventricular tissue during repolarization. For example, a high dispersion of the ventricular repolarization or large number of early after depolarizations are correlated with the risk. Moreover, some genetic mutations, as in the long QT sindrome, produce a dysfunction of the normal behavior of the ion channels of the myocytes, typically increasing the dispersion of the ventricular repolarization and prolonging the QT interval.

Other mechanisms are induced by the deformation of the ventricular tissue due to scars, infarction and enlargement of the muscular mass. The last one can be even due to parasitic infection as in Chagas disease (see sec. 6.3.1).

6.3.1 CHAGAS DISEASE

American trypanosomiasis, also called Chagas disease, is a parasitic infection widely present in central and South America.

Due to migration of infected persons from endemic areas to developed countries, ill patients now can be found also in Europe and the United States. It is induced by Trypanosoma cruzi, a protozoa that elects as its preferential sites of multiplication the myocardial and nervous fibers. As a consequence, in the chronic phase of the disease, it frequently causes a progressive deterioration of the heart muscle [136]. Chagas disease is still one of the main causes of sudden death in Latin America [137, 96].

Chagas disease might affect the anatomy of the myocardium (*e.g.*, myocarditis, cardiomegaly), the electrophysiology of the heart and its autonomic innervations. Hence, abnormalities such as sinus block, atrioventricular block, inter-ventricular block and premature ventricular contractions are typically observed. Moreover, the autonomic neuropathy that characterizes most patients with Chagas disease may also contribute to the development of heart failure or the occurrence of syncope, bradyarrhythmia or tachyarrhythmia [138].

7

CONCLUSION

In this thesis, new methodologies related to source separation and feature extraction have been proposed, studied, developed and discussed. We tested these methods on cardiac signals. Tests were performed on both synthetic and real data. Regarding synthetic simulations, we also proposed some methodologies to generate such signals.

The main novelties of this work were: i) a new algorithm for non-blind source separation; and ii) the characterization of the properties of three new features. We employed specific tests to assess the quality of the new algorithms and features.

In particular, we proposed a new non-blind source separation algorithm, *i.e.*, the modulated TMS, to track changes of the source over time. The main idea of this approach was to modulate the TMS template, *i.e.*, the source estimate, to keep the residual power in a specific range. Indeed, the main disadvantage of the classic TMS is the assumption of stationarity of the source. This assumption does not hold in many application, resulting in a limited performance of the separation and adding high power artifacts on the residue.

The modulation was performed solving an optimization problem in which the modulation parameters were refined comparing the power of the residue and the power of its first derivative with reference powers. Such reference powers were estimated considering traces of signals where it was known that the source was not present. Furthermore, since the problem had many possible solutions, we kept the modulate TMS close to the template built by the classic TMS.

The technique was tested first on synthetic data and then on real atrial electrograms to separate the atrial activity from the ventricular one. The synthetic validation was performed using signals generated by a set of equations specifically meant and proposed to model AEGs. This generator was able to mimic different types of heart rhythm, from SR to AF. The modulated TMS was tested on the most complex case, *i.e.*, AF, obtaining better performance with respect to the classic TMS. Afterwards, real AEGs of three different subjects collected during ablation procedures were employed as a real case.

In this case, the performance was evaluated counting the amount of segments in which the residual power was outside the 95^{th} percentile of the atrial power. The modulated TMS performed better even in such case.

In conclusion, this algorithm is suitable in those application in which a single measurement is available and transient sources need to be separated.

As second area of research, we studied and tested three new features. They measure the variability of the time of occurrence of transient sources ($\mathcal{V}$-index), the organization degree of wave propagation (OD), and the acceleration and deceleration capacities (AC and DC) of a system.

First, $\mathcal{V}$-index is a model-based feature requiring similar shapes for the transient sources and a relatively small variability in their times of occurrence. These assumptions are necessary to use the approximate model of the equivalent linear surface model proposed by Van Oosterom for the real T-wave.

We tested the $\mathcal{V}$-index in three different situations: i) under administration of sotalol; ii) under administration of moxifloxacin; and iii) on subjects affected by Chagas disease. Our findings suggested that the $\mathcal{V}$-index was sensitive to changes of the spatial heterogeneity of the ventricular repolarization, as result from the administration of both drugs or anatomical alterations induced by Chagas disease.

We addressed the issue of similarities among sources selecting beats with a stable heart rate. Indeed, when the heart rate is stable, the interaction of the autonomous nervous system on the ion currents can be considered stationary and thus, the action potentials as well.

Second, the OD was meant to measure the regularity of wave propagation using data collected by a set of sensors and symbolic analysis. This parameter is associated with the direction of wave propagation when the electrical activity is generated by a single wave. Indeed, when the organization of the wave propagation is relatively high, there is a high correlation between the direction of the wave and the symbol used to describe it. On the other hand, this correlation decreases when the electrical potential is generated by multiple waves. In this situation, the value of the symbols just represents the local electrical status of the atrial activity.

We tested OD on real AEGs measured on 7 subjectes during SR and AF, and during administration of isoproterenol. The atrial waves were detected and a symbolic word was used to describe the morphology and the order of arrival on a set of three electrodes. In this way, a sequence of words was built and the Shannon entropy computed.

OD was able to distinguish between the organization of atrial electrical propagation during AF from that in AF with administration of isoproterenol. Isoproterenol forced an increase of the heart rate, then made the electrical propagation more disorganized. However, in sinus rhythm, there were no differences when the isoproterenol was given because wavefronts still came from the same physiological direction.

Finally, the acceleration and deceleration capacities, *i.e.*, two metrics recently introduced by Bauer *et al.*, were tested to infer some information about the meaning of the parameters on which they depend. We tested AC and DC using a set of synthetic simulations involving AR models. These parameters, *i.e.*, L, T and s, affect the value of both capacities. In particular, the value of s played a fundamental role as frequency band

selector while T, playing on the selection of the anchor points, acts as a low pass filter. However, being this parameter built using non-linear operations, *i.e.*, the rule for the construction of the anchor point list, the linear superposition does not hold.

We also tested AC and DC on an *in*-vivo near term pregnant sheep model in which the umbilical cord was periodically occluded to mimic a lack of oxygen. We computed both capacities to assess a possible correlation with several parameters, *i.e.*, pH, lactates and base deficit, indicating the amount of lack of oxygen. Both capacities resulted in high correlation when using $s = T$ within the range $[3 - 5]$. Such values correspond to the frequency band of the RR series known to be correlated with hypoxia and acidemia.

[1] S. Särkkä, *Bayesian Filtering and Smoothing*. Cambridge Univ Pr, 2013. *(Cited on page 2)*

[2] P. Laguna, R. Jané, and P. Caminal, "Adaptive filtering of ECG baseline wander," in *Conf Proc IEEE Eng Med Biol Soc*, vol. 2. IEEE, 1992, pp. 508–509. *(Cited on page 3)*

[3] L. S ornmo, "Time-varying filtering for removal of baseline wander in exercise ECGs," in *Comput Cardiol*. IEEE, 1991, pp. 145–148. *(Cited on page 3)*

[4] L. F. Brown and S. P. Arunachalam, "Real-time t-p knot algorithm for baseline wander noise removal from the electrocardiogram - biomed 2009," *Biomed Sci Instrum*, vol. 45, pp. 65–70, 2009. *(Cited on page 3)*

[5] A. Fasano and V. Villani, "ECG baseline wander removal by QVR preserving the ST segment," in *ESGCO 2014*. IEEE, 2014, pp. 117–118. *(Cited on page 3)*

[6] ——, "Baseline wander removal for bioelectrical signals by quadratic variation reduction," *Signal Processing*, vol. 99, pp. 48–57, 2014. *(Cited on page 3)*

[7] ——, "ECG baseline wander removal and impact on beat morphology: A comparative analysis," in *Comput Cardiol*. IEEE, 2013, pp. 1167–1170. *(Cited on page 3)*

[8] J. Piskorowski, "Digital notch filter with time-varying quality factor for the reduction of powerline interference," in *Proceedings of 2010 IEEE International Symposium on Circuits and Systems (ISCAS)*. IEEE, 2010, pp. 2706–2709. *(Cited on page 3)*

[9] ——, "Powerline interference removal from ecg signal using notch filter with non-zero initial conditions," in *2012 IEEE International Symposium on Medical Measurements and Applications Proceedings (MeMeA)*. IEEE, 2012, pp. 1–3. *(Cited on page 3)*

[10] A. K. Ziarani and A. Konrad, "A nonlinear adaptive method of elimination of power line interference in ecg signals," *IEEE Trans Biomed Eng*, vol. 49, no. 6, pp. 540–547, 2002. *(Cited on page 3)*

[11] L. D. Avendaño Valencia, L. E. Avendaño, J. M. Ferrero, and G. Castellanos-Domínguez, "Improvement of an extended kalman filter power line interference suppressor for ecg signals," in *Comput Cardiol*, vol. 34. IEEE, 2007, pp. 553–556. *(Cited on page 3)*

[12] S. M. M. Martens, M. Mischi, S. G. Oei, and J. W. M. Bergmans, "An improved adaptive power line interference canceller for electrocardiography," *IEEE Trans Biomed Eng*, vol. 53, no. 11, pp. 2220–2231, 2006. *(Cited on page 3)*

[13] S. Siira, T. Ojala, T. Vahlberg, K. Rosén, and E. E., "Do spectral bands of fetal heart rate variability associate with concomitant fetal scalp ph?" *Early Hum Dev*, vol. 89, pp. 739–742, 2013. *(Cited on pages 4, 58, 67, and 68)*

[14] T. Rantonen, E. Ekholm, S. Siira, T. Mets al a, R. Leino, U. Ekblad, and I. V alim aki, "Periodic spectral components of fetal heart rate variability reflect the changes in cord arterial base deficit values: a preliminary report," *Early Hum Dev*, vol. 60, pp. 233–238, 2001. *(Cited on pages 4, 58, and 68)*

[15] D. Y. Chung, Y. B. Sim, K. T. Park, S. H. Yi, S. J. C., and S. P. Kim, "Spectral analysis of fetal heart rate variability as a predictor of intrapartum fetal distress," *Int J Gynecol Obstet*, vol. 73, pp. 109–116, 2001. *(Cited on pages 4 and 68)*

[16] J. O. Van Laar, M. M. Porath, C. H. Peters, and S. G. Oei, "Spectral analysis of fetal heart rate variability for fetal surveillance: review of the literature," *Acta Obstet Gynecol Scand*, vol. 87, pp. 300–306, 2008. *(Cited on pages 4, 58, and 68)*

[17] P. E. McSharry, G. D. Clifford, L. Tarassenko, and L. A. Smith, "A dynamical model for generating synthetic electrocardiogram signals," *IEEE Trans Biomed Eng*, vol. 50, no. 3, pp. 289–294, 2003. *(Cited on page 4)*

[18] R. Sameni and G. D. Clifford, "A review of fetal ECG signal processing; issues and promising directions," *Open Pacing Electrophysiol Ther J*, vol. 3, pp. 4–20, 2010. *(Cited on page 4)*

[19] M. Niknazar, B. Rivet, and C. Jutten, "Fetal ECG extraction by extended state kalman filtering based on single-channel recordings," *IEEE Trans Biomed Eng*, vol. 60, no. 5, pp. 1345–1352, 2013. *(Cited on page 4)*

[20] F. Andreotti, M. Riedl, T. Himmelsbach, D. Wedekind, N. Wessel, H. Stepan, C. Schmieder, A. Jank, H. Malberg, and S. Zaunseder, "Robust fetal ECG extraction and detection from abdominal leads," *Physiol Meas*, vol. 35, no. 8, pp. 1551–1567, 2014. *(Cited on page 4)*

[21] R. Sameni, M. B. Shamsollahi, C. Jutten, and G. D. Clifford, "A nonlinear bayesian filtering framework for ECG denoising," *IEEE Trans Biomed Eng*, vol. 54, no. 12, pp. 2172–2185, 2007. *(Cited on page 4)*

[22] R. Sameni, M. B. Shamsollahi, and C. Jutten, "Model-based bayesian filtering of cardiac contaminants from biomedical recordings," *Physiol Meas*, vol. 29, no. 5, pp. 595–613, 2008. *(Cited on page 4)*

[23] S. M. M. Martens, C. Rabotti, M. Mischi, and R. J. Sluijter, "A robust fetal ECG detection method for abdominal recordings," *Physiol Meas*, vol. 28, pp. 373–388, 2007. *(Cited on page 4)*

[24] V. D. A. Corino, M. W. Rivolta, R. Sassi, F. Lombardi, and L. T. Mainardi, "Ventricular activity cancellation in electrograms during atrial fibrillation with constraints on residualsṕower," *Med Eng Phys*, vol. 35, no. 12, pp. 1770–1777, 2013. *(Cited on pages 5 and 17)*

[25] J. J. Rieta and F. Hornero, "Comparative study of methods for ventricular activity cancellation in atrial electrograms of atrial fibrillation," *Physiol Meas*, vol. 28, pp. 925–936, 2007. *(Cited on pages 5, 23, 28, and 36)*

[26] P. J. Podrid and P. R. Kowey, *Cardiac Arrhythmia: mechanisms, diagnosis and management*. Williams & Wilkins, 1995. *(Cited on pages 8 and 71)*

[27] S. A. Guidera and J. S. Steinberg, "The signal-averaged p wave duration: a rapid and noninvasive marker of risk of atrial fibrillation," *J Am Coll Cardiol*, vol. 21, no. 7, pp. 1645–1651, 1993. *(Cited on page 8)*

[28] D. Amar, N. Roistacher, H. Zhang, M. S. Baum, I. Ginsburg, and J. S. Steinberg, "Signal-averaged p-wave duration does not predict atrial fibrillation after thoracic surgery," *Anesthesiol*, vol. 91, pp. 16–23, 1999. *(Cited on page 8)*

[29] Y. Koide, M. Yotsukura, H. Ando, S. Aoki, T. Suzuki, K. Sakata, E. Ootomo, and H. Yoshino, "Usefulness of p-wave dispersion in standard twelve-lead electrocardiography to predict transition from paroxysmal to persistent atrial fibrillation," *Am J Cardiol*, vol. 102, pp. 573–577, 2008. *(Cited on page 8)*

[30] T. Yamagata, A. Shimizu, T. Ueyama, T. Hayano, M. Esato, H. Tatsuno, M. Ohmura, K. Tamura, and M. Matsuzaki, "Assessment of right atrial mapping and p wave-triggered signal-average in patients with paroxysmal atrial fibrillation," *J Electrocardiol*, vol. 32, no. 3, pp. 243–251, 1999. *(Cited on page 8)*

[31] F. Censi, G. Calcagnini, C. Ricci, R. P. Ricci, M. Santini, A. Grammatico, and P. Bartolini, "P-wave morphology assessment by a gaussian functions-based model in atrial fibrillation patients," *IEEE Trans Biomed Eng*, vol. 54, pp. 663–672, 2007. *(Cited on page 9)*

[32] P. Kligfield, F. Badilini, I. Rowlandson, J. Xue, E. Clark, B. Devine, P. Macfarlane, J. de Bie, D. Mortara, S. Babaeizadeh, R. Gregg, E. D. Helfenbein, and C. L. Green, "Comparison of automated measurements of electrocardiographic intervals and durations by computer-based algorithms of digital electrocardiographs," *Am Heart J*, vol. 167, no. 2, pp. 150–159.e1, 2014. *(Cited on pages XII, 9, and 47)*

[33] D. M. Bloomfield, J. T. Kost, K. Ghosh, D. Hreniuk, L. A. Hickey, M. J. Guitierrez, K. Gottesdiener, and J. A. Wagner, "The effect of moxifloxacin on QTc and implications for the design of thorough QT studies," *Clin Pharm Ther*, vol. 84, no. 4, pp. 475–480, 2008. *(Cited on pages XII, 9, 43, 44, 47, and 49)*

[34] H. C. Bazett, "An analysis of the time-relations of electrocardiograms," *Heart*, vol. 7, pp. 353–370, 1920. *(Cited on page 9)*

[35] L. S. Fridericia, "The duration of systole in the electrocardiogram of normal subjects and of patients with heart disease," *Acta Med Scand*, vol. 53, pp. 469–486, 1920. *(Cited on page 9)*

[36] M. Malik, K. Hnatkova, D. Kowalski, J. J. Keirns, and E. M. van Gelderen, "Importance of subject-specific QT/RR curvatures in the design of individual heart rate corrections of the QT interval," *J Electrocardiol*, vol. 45, pp. 571–581, 2012. *(Cited on page 9)*

[37] M. Malik, K. Hnatkova, T. Novotny, and G. Schmidt, "Subject-specific profiles of QT/RR hysteresis," *Am J Physiol Heart Circ Physiol*, vol. 295, pp. 2356–2363, 2008. *(Cited on page 9)*

[38] J. H. Indik, E. C. Pearson, K. Fried, and R. L. Woosley, "Bazett and fridericia QT correction formulas interfere with measurement of drug-induced changes in QT interval," *Heart Rhythm*, vol. 3, no. 9, pp. 1003–1007, 2006. *(Cited on page 9)*

[39] A. Mincholé, E. Pueyo, J. F. Rodríguez, E. Zacur, M. Doblaré, and P. Laguna, "Quantification of restitution dispersion from the dynamic changes of the T-Wave peak to end, measured at the surface ECG," *IEEE Trans Biomed Eng*, vol. 58, no. 5, pp. 1172–1182, 2011. *(Cited on page 9)*

[40] F. Extramiana, R. Dubois, M. Vaglio, P. Roussel, G. Dreyfus, F. Badilini, A. Leenhardt, and P. Maison-Blanche, "The time course of new t-wave ECG descriptors following single-and double-dose administration of sotalol in healthy subjects," *Ann Noninvasive Electrocardiol*, vol. 15, no. 1, pp. 26–35, 2010. *(Cited on page 9)*

[41] F. Extramiana, C. Tatar, P. Maison-Blanche, I. Denjoy, A. Messali, P. Dejode, F. Iserin, and A. Leenhardt, "Beat-to-beat t-wave amplitude variability in the long QT syndrome," *Europace*, vol. 12, no. 9, pp. 1302–1307, 2010. *(Cited on page 9)*

[42] F. Extramiana, A. Haggui, P. Maison-Blanche, R. Dubois, S. Takatsuki, P. Beaufils, and A. Leenhardt, "T-wave morphology parameters based on principal component analysis reproducibility and dependence on t-offset position," *Ann Noninvasive Electrocardiol*, vol. 12, no. 4, pp. 354–363, 2007. *(Cited on page 9)*

[43] R. Sassi and L. T. Mainardi, "An estimate of the dispersion of repolarization times based on a biophysical model of the ECG." *IEEE Trans Biomed Eng*, vol. 58, no. 12, pp. 3396–3405, 2011. *(Cited on pages 9, 39, 40, 42, and 50)*

[44] A. van Oosterom, "Genesis of the t wave as based on an equivalent surface source model," *J Electrocardiol*, vol. 34, pp. 217–227, 2001. *(Cited on pages 9 and 40)*

[45] V. D. A. Corino, F. Holmqvist, L. T. Mainardi, and P. G. Platonov, "Beta-blockade and a1-adenosine receptor agonist effects on atrial fibrillatory rate and atrioventricular conduction in patients with atrial fibrillation," *Europace*, vol. 16, no. 4, pp. 587–594, 2014. *(Cited on page 10)*

[46] R. Buchhorn, "Why are psychiatric disorders in children becoming more and more common?" *Int J Emerg Ment Health*, vol. 16, no. 2, pp. 322–325, 2014. *(Cited on page 10)*

[47] S. Lee, H. Kim, D. H. Kim, M. Yum, and M. Son, "Heart rate variability in male shift workers in automobile manufacturing factories in south korea," *Int Arch Occup Environ Health*, 2015. *(Cited on page 10)*

[48] A. Bauer, J. W. Kantelhardt, A. Bunde, P. Barthel, R. Schneider, M. Malik, and G. Schmidt, "Phase-rectified signal averaging detects quasi-periodicities in non-stationary data," *Physica A*, vol. 364, pp. 423–434, 2006. *(Cited on pages 10, 51, and 67)*

[49] J. W. Kantelhardt, A. Bauer, A. Y. Schumann, P. Barthel, R. Schneider, M. Malik, and G. Schmidt, "Phase-rectified signal averaging for the detection of quasi-periodicities and the prediction of cardiovascular risk," *Chaos*, vol. 17, no. 1, pp. 015 112–015 112–9, 2007. *(Cited on pages 10, 52, and 68)*

[50] E. A. Huhn, S. Lobmaier, T. Fischer, R. Schneider, A. Bauer, K. T. Schneider, and G. Schmidt, "New computerized fetal heart rate analysis for surveillance of intrauterine growth restriction," *Prenat Diagn*, vol. 31, pp. 509–514, 2011. *(Cited on pages 10, 52, and 68)*

[51] A. Bauer, J. W. Kantelhardt, P. Barthel, R. Schneider, T. M akikallio, K. Ulm, K. Hnatkova, A. Sch omig, H. Huikuri, A. Bunde, M. Malik, and G. Schmidt, "Deceleration capacity of heart rate as a predictor of mortality after myocardial infarction: cohort study," *The Lancet*, vol. 367, no. 9523, pp. 1674–1681, 2006. *(Cited on pages 10, 51, 52, 57, 68, and 70)*

[52] A. Bauer, P. Barthel, A. M uller, K. Ulm, H. Huikuri, M. Malik, and G. Schmidt, "Risk prediction by heart rate turbulence and deceleration capacity in postinfarction patients with preserved left ventricular function retrospective analysis of 4 independent trials," *J Electrocardiol*, vol. 42, no. 6, pp. 597–601, 2009. *(Cited on page 10)*

[53] M. Mohebbi and H. Ghassemian, "Prediction of paroxysmal atrial fibrillation based on non-linear analysis and spectrum and bispectrum features of the heart rate variability signal," *Comput Methods Programs Biomed*, vol. 105, no. 1, pp. 40–49, 2012. *(Cited on page 10)*

[54] F. Onorati, R. Barbieri, M. Mauri, V. Russo, and L. Mainardi, "Characterization of affective states by pupillary dynamics and autonomic correlates," *Front Neuroeng*, vol. 6, no. 9, pp. 1–11, 2013. *(Cited on page 10)*

[55] T. E. Dick, J. R. Mims, Y. H. Hsieh, K. F. Morris, and E. A. Wehrwein, "Increased cardio-respiratory coupling evoked by slow deep breathing can persist in normal humans," *Respir Physiol Neurobiol*, vol. 204, pp. 99–111, 2014. *(Cited on page 10)*

[56] S. Nakahara, Y. Hori, A. Hayashi, S. Kobayashi, H. Nakamura, Y. Okumura, and K. Takayanagi, "Impact of left atrial appendage ridge ablation on the complex

fractionated electrograms in persistent atrial fibrillation," *J Interv Card Electrophysiol*, vol. 41, no. 1, pp. 55–64, 2014. *(Cited on page 10)*

[57] O. Berenfeld, M. Yamazaki, D. Filgueiras-Rama, and J. Kalifa, "Surface and intramural reentrant patterns during atrial fibrillation in the sheep," *Methods Inf Med*, vol. 53, no. 4, pp. 314–319, 2014. *(Cited on page 10)*

[58] M. Rodrigo, M. S. Guillem, A. M. Climent, J. Pedrón-Torrecilla, A. Liberos, J. Millet, F. Fernández-Avilés, F. Atienza, and O. Berenfeld, "Body surface localization of left and right atrial high-frequency rotors in atrial fibrillation patients: A clinical-computational study," *Heart Rhythm*, vol. 11, no. 9, pp. 1584–1591, 2014. *(Cited on page 10)*

[59] J. L. Salinet, J. H. Tuan, A. J. Sandilands, P. J. Stafford, F. S. Schlindwein, and G. André Ng, "Distinctive patterns of dominant frequency trajectory behavior in drug-refractory persistent atrial fibrillation: preliminary characterization of spatiotemporal instability," *J Cardiovasc Electrophysiol*, vol. 25, no. 4, pp. 371–379, 2014. *(Cited on page 10)*

[60] S. K. Wood, "Cardiac autonomic imbalance by social stress in rodents: understanding putative biomarkers," *Front Psychol*, vol. 5, p. 950, 2014. *(Cited on page 10)*

[61] S. J. Brown, M. J. Barnes, and T. M undel, "Effects of hypoxia and hypercapnia on human hrv and respiratory sinus arrhythmia," *Acta Physiol Hung*, vol. 101, no. 3, pp. 263–272, 2014. *(Cited on page 10)*

[62] V. Brando, S. Castro-Zaballa, A. Falconi, P. Torterolo, and E. R. Migliaro, "Statistical, spectral and non-linear analysis of the heart rate variability during wakefulness and sleep," *Arch Ital Biol*, vol. 152, no. 1, pp. 32–46, 2014. *(Cited on page 10)*

[63] M. Mohebbi, H. Ghassemian, and B. M. Asl, "Structures of the recurrence plot of heart rate variability signal as a tool for predicting the onset of paroxysmal atrial fibrillation," *J Med Signals Sens*, vol. 1, no. 2, pp. 113–121, 2011. *(Cited on page 11)*

[64] L. Eduardo Virgilio Silva and L. Otavio Murta, "Evaluation of physiologic complexity in time series using generalized sample entropy and surrogate data analysis," *Chaos*, vol. 22, no. 4, p. 043105, 2012. *(Cited on page 11)*

[65] X. Zhou, H. Ding, B. Ung, E. Pickwell-MacPherson, and Y. Zhang, "Automatic online detection of atrial fibrillation based on symbolic dynamics and shannon entropy," *Biomed Eng Online*, vol. 13, no. 1, p. 18, 2014. *(Cited on page 11)*

[66] V. C. Kunz, R. B. Souza, A. C. Takahashi, A. M. Catai, and E. Silva, "The relationship between cardiac autonomic function and clinical and angiographic characteristics in patients with coronary artery disease," *Rev Bras Fisioter*, vol. 15, no. 6, pp. 503–510, 2011. *(Cited on page 11)*

[67] V. R. Neves, A. C. Takahashi, M. D. do Santos-Hiss, A. M. Kiviniemi, M. P. Tulppo, S. C. de Moura, M. Karsten, A. Borghi-Silva, A. Porta, N. Montano, and A. M.

Catai, "Linear and nonlinear analysis of heart rate variability in coronary disease," *Biomed Eng Online*, vol. 22, no. 4, pp. 175–183, 2012. *(Cited on page 11)*

[68] F. C. Pivatelli, M. A. Dos Santos, G. B. Fernandes, M. Gatti, L. C. de Abreu, V. E. Valenti, L. C. Vanderlei, C. Ferreira, F. Adami, T. D. de Carvalho, C. B. Monteiro, and M. F. de Godoy, "Sensitivity, specificity and predictive values of linear and nonlinear indices of heart rate variability in stable angina patients," *Int Arch Med*, vol. 5, no. 1, p. 31, 2012. *(Cited on page 11)*

[69] V. C. Kunz, E. N. Borges, R. C. Coelho, L. A. Gubolino, L. E. Martins, and E. Silva, "Linear and nonlinear analysis of heart rate variability in healthy subjects and after acute myocardial infarction in patients," *Braz J Med Biol Res*, vol. 45, no. 5, pp. 450–458, 2012. *(Cited on page 11)*

[70] T. J. Moss, D. E. Lake, and J. R. Moorman, "Local dynamics of heart rate: detection and prognostic implications," *Physiol Meas*, vol. 35, no. 10, pp. 1929–1942, 2014. *(Cited on page 11)*

[71] S. Lau, J. Haueisen, E. G. Schukat-Talamazzini, A. Voss, M. Goernig, U. Leder, and H. R. Figulla, "Low hrv entropy is strongly associated with myocardial infarction," *Biomed Tech (Berl)*, vol. 51, no. 4, pp. 186–189, 2006. *(Cited on page 11)*

[72] D. E. Vigo, L. Nicola Siri, M. S. Ladrón De Guevara, J. A. Martínez-Martínez, R. D. Fahrer, D. P. Cardinali, O. Masoli, and S. M. Guinjoan, "Relation of depression to heart rate nonlinear dynamics in patients > or =60 years of age with recent unstable angina pectoris or acute myocardial infarction," *Am J Cardiol*, vol. 93, no. 6, pp. 756–760, 2004. *(Cited on page 11)*

[73] J. Kennedy and R. Eberhart, "Particle swarm optimization," in *Proceedings of IEEE International Conference on Neural Networks. IV*, 1995, pp. 1942–1948. *(Cited on page 14)*

[74] F. Van den Bergh and A. P. Engelbrecht, "A cooperative approach to particle swarm optimization," *IEEE Trans Evol Comput*, vol. 8, pp. 225–39, 2004. *(Cited on page 14)*

[75] B. Niu, X. Zhu, Y.and He, and H. Wu, "Mcpso: A multi-swarm cooperative particle swarm optimizer," *Appl Math Comput*, vol. 2, pp. 1050–1062, 2007. *(Cited on page 14)*

[76] L. Vanneschi, D. Codecasa, and G. Mauri, "A comparative study of four parallel and distributed PSO methods," *New Gener Comput*, vol. 29, pp. 129–161, 2011. *(Cited on pages 14 and 29)*

[77] M. W. Rivolta, L. T. Mainardi, R. Sassi, and V. D. A. Corino, "Synthetic atrial electrogram generator," in *XIII Mediterranean Conference on Medical and Biological Engineering and Computing 2013*, 2013, pp. 670–673. *(Cited on page 17)*

[78] L. T. Mainardi, M. W. Rivolta, R. Scanziani, V. D. A. Corino, and R. Sassi, "Cancellation of ventricular activity in endocavitary recordings during atrial fibrillation by particle swarm optimization," in *Comput Cardiol*, vol. 38, 2011, pp. 597–600. *(Cited on pages 17 and 28)*

[79] M. S. Spach, R. C. Barr, E. A. Johnson, and J. M. Kootsey, "Cardiac extracellular potentials: Analysis of complex wave forms about the purkinje networks in dogs," *Circ Res*, vol. 33, pp. 465–473, 1973. *(Cited on pages 17, 27, and 76)*

[80] J. Malmivuo and R. Plonsey, *Bioelectromagnetism: Principles and Applications of Bioelectric and Biomagnetic Fields*. Oxford University Press, 1995. *(Cited on page 18)*

[81] T. S. Soderstrom and P. G. Stoica, *System Identification*, P. Hall, Ed. Prentice Hall, 1989. *(Cited on page 19)*

[82] J. Lian, J. Müssig, and V. Lang, "Computer modeling of ventricular rhythm during atrial fibrillation and ventricular pacing," *IEEE Trans Biomed Eng*, vol. 53, pp. 1512–1520, 2006. *(Cited on page 19)*

[83] V. D. A. Corino, F. Sandberg, L. T. Mainardi, and L. Sörnmo, "An atrioventricular node model for analysis of the ventricular response during atrial fibrillation," *IEEE Trans Biomed Eng*, vol. 58, pp. 3386–3395, 2011. *(Cited on page 19)*

[84] T. H. Everett, L. Kok, R. H. Vaughn, J. R. Moorman, and D. E. Haines, "Frequency domain algorithm for quantifying atrial fibrillation organization to increase defibrillation efficacy," *IEEE Trans Biomed Eng*, vol. 48, pp. 969–978, 2001. *(Cited on page 21)*

[85] L. Faes, G. Nollo, R. Antolini, F. Gaita, and F. Ravelli, "A method for quantifying atrial fibrillation organization based on wave-morphology similarity," *IEEE Trans Biomed Eng*, vol. 49, no. 12, pp. 1504–1513, 2002. *(Cited on pages 21, 28, 33, and 36)*

[86] M. W. Rivolta, L. T. Mainardi, and R. Sassi, "A novel measure of atrial fibrillation organization based on symbolic analysis," in *Comput Cardiol*, vol. 39, 2012, pp. 813–816. *(Cited on page 32)*

[87] G. A. F. Seber, *Multivariate Observations*. Hoboken, NJ: John Wiley & Sons, Inc., 1984. *(Cited on page 33)*

[88] L. T. Mainardi, V. D. A. Corino, L. Lombardi, C. Tondo, M. Mantica, F. Lombardi, and S. Cerutti, "Assessment of the dynamics of atrial signals and local atrial period series during atrial fibrillation: effects of isoproterenol administration," *Biomed Eng OnLine*, vol. 3, no. 37, 2004. *(Cited on pages 35 and 37)*

[89] L. Faes, G. Nollo, M. Kirchner, E. Olivetti, F. Gaita, R. Riccardi, and R. Antolini, "Principal component analysis and cluster analysis formeasuring the local organisation of human atrial fibrillation." *Med. Biol. Eng. Comput.*, vol. 39, pp. 656–663, 2001. *(Cited on page 37)*

[90] M. W. Rivolta, F. Badilini, L. T. Mainardi, M. Vaglio, and R. Sassi, "Quantification of ventricular repolarization heterogeneity during sotalol administration using the v-index." *J Electrocardiol*, vol. 46, no. 6, pp. 625–625, 2013. *(Cited on pages 39 and 58)*

[91] M. W. Rivolta, L. T. Mainardi, and R. Sassi, "Quantification of ventricular repolarization heterogeneity during moxifloxacin administration using v-index," in *8th Conference of the European Study Group on Cardiovascular Oscillations (ESGCO)*. IEEE, 2014, pp. 183–184. *(Cited on page 39)*

[92] R. Sassi, M. W. Rivolta, L. T. Mainardi, A. L. P. Ribeiro, and F. Lombardi, "Spatial repolarization heterogeneity and survival in chagas disease," in *Proceedings of the 7th International Workshop on Biosignal Interpretation (BSI2012)*, 2012, pp. 295–298. *(Cited on page 39)*

[93] R. Sassi, M. W. Rivolta, L. T. Mainardi, R. C. Reis, M. O. C. Rocha, A. L. P. Ribeiro, and F. Lombardi, "Spatial repolarization heterogeneity and survival in chagas disease," *Methods Inf Med*, vol. 53, no. 4, pp. 1–5, 2014. *(Cited on pages 39 and 49)*

[94] L. Mainardi, D. Di Donato, D. Falcone, and R. Sassi, "Improved estimation of v-index based on analytic forms of dominant t-wave," in *Computing in Cardiology Conference (CinC), 2013*, vol. 40, 2013, pp. 467–470. *(Cited on pages 42 and 43)*

[95] N. Sarapa, J. Morganroth, J. Couderc, S. F. Francom, B. Darpo, J. C. Fleishaker, J. D. McEnroe, W. T. Chen, W. Zareba, and A. J. Moss, "Electrocardiographic identification of drug-induced qt prolongation: Assessment by different recording and measurement methods," *ANE*, vol. 9, no. 1, pp. 48–57, 2004. *(Cited on pages 43 and 49)*

[96] M. C. P. Nunes, W. Dones, C. A. Morillo, J. J. Encina, and A. L. Ribeiro, "Chagas disease: An overview of clinical and epidemiological aspects," *J Am Coll Cardiol*, vol. 62, no. 9, pp. 767–776, 2013. *(Cited on pages 43 and 77)*

[97] F. Extramiana, R. Dubois, M. Vaglio, P. Roussel, G. Dreyfus, F. Badilini, A. Leenhardt, and P. Maison-Blanche, "The time course of new t-wave ECG descriptors following single-and double-dose administration of sotalol in healthy subjects," *Ann Noninvasive Electrocardiol*, vol. 15, no. 1, pp. 26–35, 2010. *(Cited on page 43)*

[98] A. L. Ribeiro, P. S. Cavalvanti, F. Lombardi, M. D. O. C. Nunes, M. V. Barros, and M. O. Rocha, "Prognostic value of signal-averaged electrocardiogram in chagas disease," *J Cardiovasc Electrophysiol*, vol. 19, no. 5, pp. 502–509, 2008. *(Cited on pages 44 and 45)*

[99] A. L. P. Ribeiro, M. O. D. C. Rocha, P. Terranova, M. Cesarano, M. D. C. P. Nunes, and F. Lombardi, "T-wave amplitude variability and the risk of death in chagas disease," *J Cardiovasc Electrophysiol*, vol. 22, no. 7, pp. 799–805, 2011. *(Cited on pages 44, 48, and 49)*

[100] J. P. Couderc, W. Zareba, S. McNitt, P. Maison-Blanche, and A. J. Moss, "Repolarization variability in the risk stratification of madit ii patients," *Europace*, vol. 9, no. 9, pp. 717–723, 2007. *(Cited on pages 44 and 49)*

[101] F. E. Harrell, *Regression Modeling Strategies: With Applications to Linear Models, Logistic Regression, and Survival Analysis*. Springer, 2001. *(Cited on page 44)*

[102] E. W. Steyerberg, *Clinical prediction models: a practical approach to development, validation, and updating*. New York: Springer, 2009. *(Cited on page 44)*

[103] E. Lepeschkin and B. Surawicz, "The measurement of the q-t interval of the electrocardiogram," *Circulation*, vol. 6, no. 3, pp. 378–388, 1952. *(Cited on page 45)*

[104] R. Sassi and L. Mainardi, "Quantification of spatial repolarization heterogeneity: Testing the robustness of a new technique," in *Computing in Cardiology Conference (CinC), 2012*, vol. 39, 2012, pp. 69–72. *(Cited on page 45)*

[105] F. Badilini, P. Maison-Blanche, R. Childers, and P. Coumel, "Qt interval analysis on ambulatory electrocardiogram recordings: a selective beat averaging approach," *Med Biol Eng Comput*, vol. 37, pp. 71–79, 1999. *(Cited on page 45)*

[106] F. G. Akar, G. X. Yan, C. Antzelevitch, and D. S. Rosenbaum, "Unique topographical distribution of m cells underlies reentrant mechanism of torsade de pointes in the long-QT syndrome," *Circulation*, vol. 105, no. 10, pp. 1247–1253, 2002. *(Cited on page 49)*

[107] X. Chen, J. D. Cass, J. A. Bradley, C. M. Dahm, Z. Sun, E. Kadyszewski, M. J. Engwall, and J. Zhou, "QT prolongation and proarrhythmia by moxifloxacin: concordance of preclinical models in relation to clinical outcome," *Br J Pharmacol*, vol. 146, no. 6, pp. 792–799, 2005. *(Cited on page 49)*

[108] S. M. Lobmaier, E. A. Huhn, S. Pildner von Steinburg, A. Müller, T. Schuster, J. U. Ortiz, G. Schmidt, and K. T. Schneider, "Phase-rectified signal averaging as a new method for surveillance of growth restricted fetuses," *J Matern Fetal Neonatal Med*, vol. 25, no. 12, pp. 2523–2528, 2012. *(Cited on pages 52 and 68)*

[109] E. M. Graatsma, E. J. H. Mulder, B. Vasak, S. M. Lobmaier, S. Pildner von Steinburg, K. T. M. Schneider, G. Schmidt, and G. H. A. Visser, "Average acceleration and deceleration capacity of fetal heart rate in normal pregnancy and in pregnancies complicated by fetal growth restriction," *J Matern Fetal Neonatal Med*, vol. 25, no. 12, pp. 2517–2522, 2012. *(Cited on pages 52 and 68)*

[110] A. Bauer, J. W. Kantelhardt, A. Bunde, P. Barthel, R. Schneider, M. Malik, and G. Schmidt, "Phase-rectified signal averaging detects quasi-periodicities in non-stationary data," *J Phys A*, vol. 364, pp. 423–434, 2006. *(Cited on pages XII, 52, and 55)*

[111] M. W. Rivolta, T. Stampalija, D. Casati, E. Ferrazzi, A. Bauer, and R. Sassi, "A methodological assessment of phase-rectified signal averaging through simulated beat-to-beat interval time series," in *Computing in Cardiology Conference (CinC), 2014*, vol. 41, 2014, pp. 601–604. *(Cited on pages 53 and 70)*

[112] T. Stampalija, D. Casati, V. Maggi, M. W. Rivolta, S. Lupini, K. Rizas, R. Sassi, A. Bauer, and E. Ferrazzi, "Analysis of fetal ecg in fetal growth restriction," in *REPRODUCTIVE SCIENCES*, vol. 21, no. 3. SAGE PUBLICATIONS INC 2455 TELLER RD, THOUSAND OAKS, CA 91320 USA, 2014, pp. 85A–85A. *(Cited on page 58)*

[113] M. W. Rivolta, R. Sassi, T. Stampalija, D. Casati, M. Frasch, B. Richardson, M. G. Ross, K. Rizas, A. Bauer, and E. Ferrazzi, "Correlation between average acceleration and deceleration capacity of fetal heart rate and biomarkers of acid-base status in a vivo sheep model." in *REPRODUCTIVE SCIENCES*, vol. 21, no. 3. SAGE PUBLICATIONS INC 2455 TELLER RD, THOUSAND OAKS, CA 91320 USA, 2014, pp. 171A–171A. *(Cited on page 58)*

[114] M. W. Rivolta, R. Sassi, D. Casati, T. Stampalija, M. Frasch, B. Richardson, M. G. Ross, K. Rizas, A. Bauer, and E. Ferrazzi, "In vivo evaluation of acceleration and deceleration capacity of fetal heart rate in worsening hypoxic acidemia," in *REPRODUCTIVE SCIENCES*, vol. 21, no. 3. SAGE PUBLICATIONS INC 2455 TELLER RD, THOUSAND OAKS, CA 91320 USA, 2014, pp. 85A–85A. *(Cited on page 58)*

[115] Z. Alfirevic, D. Devane, and G. M. Gyte, "Continuous cardiotocography (ctg) as a form of electronic fetal monitoring (efm) for fetal assessment during labour," *Cochrane Database Syst Rev*, vol. 5, p. CD006066, 2013. *(Cited on page 58)*

[116] J. P. Neilson, "Fetal electrocardiogram (ecg) for fetal monitoring during labour," *Cochrane Database Syst Rev*, vol. 5, p. CD000116, 2013. *(Cited on page 58)*

[117] M. Westerhuis, A. Kwee, A. van Ginkel, A. Drogtrop, W. Gyselaers, and V. G., "Limitations of st analysis in clinical practice: three cases of intrapartum metabolic acidosis," *BJOG*, vol. 114, pp. 1194–1201, 2007. *(Cited on page 58)*

[118] H. Sabir, H. Stannigel, A. Schwarz, and H. T., "Perinatal hemorrhagic shock after fetal scalp blood sampling," *Obstet Gynecol*, vol. 115, pp. 419–420, 2010. *(Cited on page 58)*

[119] D. Casati and M. G. Frasch, "Analysis of fetal heart rate variability in frequency domain: methodical considerations," *Exp Physiol*, vol. 99, pp. 466–467, 2014. *(Cited on page 58)*

[120] M. G. Ross, M. Jessie, K. Amaya, B. Matushewski, L. D. Durosier, M. G. Frasch, and B. S. Richardson, "Correlation of arterial fetal base deficit and lactate changes with severity of variable heart rate decelerations in the near-term ovine fetus," *Am J Obstet Gynecol*, vol. 208, no. 4, pp. 285.e1–6, 2013. *(Cited on pages 59 and 67)*

[121] L. R. Green, J. Homan, S. E. White, and B. S. Richardson, "Cardiovascular and metabolic responses to intermittent umbilical cord occlusion in the preterm ovine fetus," *J Soc Gynecol Investig*, vol. 6, no. 2, pp. 56–63, 1999. *(Cited on page 59)*

[122] M. Frasch, T. M uller, D. Hoyer, C. Weiss, H. Schubert, and M. Schwab, "Nonlinear properties of vagal and sympathetic modulations of heart rate variability in ovine fetus near term," *Am J Physiol Regul Integr Comp Physiol*, vol. 296, pp. R702–R707, 2009. *(Cited on pages 59 and 67)*

[123] A. P. Prout, M. G. Frasch, R. A. Veldhuizen, R. Hammond, and M. G. Ross, "Systemic and cerebral inflammatory response to umbilical cord occlusions with worsening acidosis in the ovine fetus," *Am J Obstet Gynecol*, vol. 202, no. 1, pp. 82.e1–82.e9, 2010. *(Cited on page 59)*

[124] T. F. of The European Society of Cardiology, T. N. A. S. of Pacing, and Electrophysiology, "Heart rate variability. standards of measurement, physiological interpretation, and clinical use," *Circulation*, vol. 93, pp. 1043–1065, 1996. *(Cited on page 67)*

[125] J. Parer, H. Dijkstra, J. Harris, T. Krueger, and M. Reuss, "Increased fetal heart rate variability with acute hypoxia in chronically instrumented sheep," *Eur J Obstet Gynaecol Reprod Biol*, vol. 10, pp. 393–399, 1980. *(Cited on pages 67 and 69)*

[126] L. J. Groome, P. C. Loizou, S. B. Holland, L. A. Smith, and C. Hoff, "High vagal tone is associated with more efficient regulation of homeostasis in low-risk human fetuses," *Dev Psychobiol*, vol. 35, pp. 25–34, 1999. *(Cited on page 67)*

[127] A. J. W. Fletcher, D. S. Gardner, C. M. B. Edwards, A. L. Fowden, and D. A. Giussani, "Development of the ovine fetal cardiovascular defense to hypoxemia towards full term," *Am J Physiol Heart Circ Physiol*, vol. 391, no. 6, pp. H3023–H3034, 2006. *(Cited on page 67)*

[128] J. Murotsuki, A. D. Bocking, and R. Gagnon, "Fetal heart rate patterns in growth-restricted fetal sheep induced by chronic fetal placental embolization," *Am J Obstet Gynecol*, vol. 176, pp. 282–290, 1997. *(Cited on page 67)*

[129] J. Itskovitz and A. M. Rudolph, "Denervation of arterial chemoreceptors and baroreceptors in fetal lambs in utero," *Am J Physiol*, vol. 242, no. 5, pp. H916–H920, 1982. *(Cited on page 68)*

[130] C. Eick, K. D. Rizas, C. S. Zuern, and B. A., "Automated assessment of cardiac autonomic function by means of deceleration capacity from noisy, nonstationary ecg signals: Validation study," *Ann Noninvasive Electrocardiol*, vol. 19, pp. 122–128, 2014. *(Cited on page 68)*

[131] A. Malliani, F. Lombardi, M. Pagani, and C. S., "Power spectral analysis of cardiovascular variability in patients at risk for sudden cardiac death," *J Cardiovasc Electrophysiol*, vol. 5, no. 3, pp. 274–286, 1994. *(Cited on page 70)*

[132] F. Lombardi, G. Sandrone, A. Mortara, D. Torzillo, M. T. La Rovere, M. G. Signorini, S. Cerutti, and A. Malliani, "Linear and nonlinear dynamics of heart rate variability after acute myocardial infarction with normal and reduced left ventricular ejection fraction," *Am J Cardiol*, vol. 77, no. 15, pp. 1283–1288, 1996. *(Cited on page 70)*

[133] A. Bollmann, D. Husser, L. T. Mainardi, F. Lombardi, P. Langley, A. Murray, J. J. Rieta, J. Millet, S. B. Olsson, M. Stridh, and L. Sörnmo, "Analysis of surface electrocardiograms in atrial fibrillation: Techniques, research, and clinical applications," *Europace*, vol. 8, pp. 911–926, 2006. *(Cited on page 75)*

[134] Developed with the special contribution of the European Heart Rhythm Association (EHRA), Endorsed by the European Association for Cardio-Thoracic Surgery (EACTS), Authors/Task Force Members, A. J. Camm, P. Kirchhof, G. Y. H. Lip, U. Schotten, I. Savelieva, S. Ernst, I. C. Van Gelder, N. Al-Attar, G. Hindricks, B. Prendergast, H. Heidbuchel, O. Alfieri, A. Angelini, D. Atar, P. Colonna, R. De Caterina, J. De Sutter, A. Goette, B. Gorenek, M. Heldal, S. H. Hohloser, P. Kolh, J.-Y. Le Heuzey, P. Ponikowski, F. H. Rutten, ESC Committee for Practice Guidelines (CPG), A. Vahanian, A. Auricchio, J. Bax, C. Ceconi, V. Dean, G. Filippatos, C. Funck-Brentano, R. Hobbs, P. Kearney, T. McDonagh, B. A. Popescu, Z. Reiner, U. Sechtem, P. A. Sirnes, M. Tendera, P. E. Vardas, P. Widimsky, Document Reviewers, P. E. Vardas, V. Agladze, E. Aliot, T. Balabanski, C. Blomstrom-Lundqvist, A. Capucci, H. Crijns, B. Dahlof, T. Folliguet, M. Glikson, M. Goethals, D. C. Gulba, S. Y. Ho, R. J. M. Klautz, S. Kose, J. McMurray, P. Perrone Filardi, P. Raatikainen, M. J. Salvador, M. J. Schalij, A. Shpektor, J. Sousa, J. Stepinska, H. Uuetoa, J. L. Zamorano, and I. Zupan, "Guidelines for the management of atrial fibrillation: The task force for the management of atrial fibrillation of the european society of cardiology (ESC)," *Eur Heart J*, vol. 31, no. 19, pp. 2369–2429, 2010. *(Cited on pages 75 and 76)*

[135] A. Bollmann and F. Lombardi, "Electrocardiology of atrial fibrillation. current knowledge and future challenges," *IEEE Eng Med Biol Mag*, vol. 25, no. 6, pp. 15–23, 2006. *(Cited on page 76)*

[136] F. S. Laranja, E. Dias, G. Nobrega, and A. Miranda, "Chagas' disease: A clinical, epidemiologic, and pathologic study," *Circulation*, vol. 14, no. 6, pp. 1035–1060, 1956. *(Cited on page 77)*

[137] A. Rassi, Jr, A. Rassi, W. C. Little, S. S. Xavier, S. G. Rassi, A. G. Rassi, G. G. Rassi, A. Hasslocher-Moreno, A. S. Sousa, and M. I. Scanavacca, "Development and validation of a risk score for predicting death in Chagas' heart disease," *N Engl J Med*, vol. 355, no. 8, pp. 799–808, 2006. *(Cited on page 77)*

[138] D. S. Amorim, R. A. Godoy, J. C. ManÃ§o, A. Tanaka, and L. Gallo, "Effects of acute elevation in blood pressure and of atropine on heart rate in chagas' disease: A preliminary report," *Circulation*, vol. 38, no. 2, pp. 289–294, 1968. *(Cited on page 77)*

A

PUBLICATIONS

Journal:

1. Rivolta MW, Mainardi LT, Sassi R. "Quantification of ventricular repolarization heterogeneity during moxifloxacin or sotalol administration using $\mathcal{V}$-index", Physiol Meas, in press.

2. Rivolta MW, Stampalija T, Casati D, Richardson BS, Ross MG, Frasch MG, Bauer A, Ferrazzi E, Sassi R. "Acceleration and deceleration capacity of fetal heart rate in an in-vivo sheep model", PLoS One, vol. 9, no. 8, pp. e104193, 2014.

3. Sassi R, Rivolta MW, Mainardi LT, Reis RC, Rocha MO, Ribeiro AL, Lombardi F. "Spatial Repolarization Heterogeneity and Survival in Chagas Disease", Methods Inf Med, vol. 53, no. 4, 2014.

4. Corino VD, Rivolta MW, Sassi R, Lombardi F, Mainardi LT. "Ventricular activity cancellation in electrograms during atrial fibrillation with constraints on residuals' power", Med Eng Phys, vol. 35, no. 12, pp. 1770 – 1777, 2013.

Conference:

1. Rivolta MW, Migliorini M, Aktaruzzaman M, Sassi R, Bianchi AM. "Effects of the series length on Lempel-Ziv Complexity during sleep", EMBC2014, pp. 693 – 696, 2014.

2. Rivolta MW, Mainardi LT, Sassi R. "Quantification of ventricular repolarization heterogeneity during moxifloxacin administration using $\mathcal{V}$-index", ESCGO2014, pp. 183 – 184, 2014.

3. Sassi R, Stampalija T, Casati D, Ferrazzi E, Bauer A, Rivolta MW. "A Methodological Assessment of Phase-Rectified Signal Averaging through Simulated Beat-to-Beat Interval Time Series", Computing in Cardiology, 2014.

4. Rivolta MW, Mainardi LT, Sassi R, Corino VDA. "Synthetic Atrial Electrogram Generator", IFMBE Proceedings, vol. 41, pp. 670 – 673, 2013.

5. Rivolta MW, Mainardi LT, Sassi R. "A Novel Measure of Atrial Fibrillation Organization based on Symbolic Analysis", Computing in Cardiology, vol. 39, pp. 813 – 816, 2012.

6. Sassi R, Rivolta MW, Mainardi LT, Ribeiro ALP, Lombardi F. "Spatial repolarization heterogeneity and survival in Chagas disease", BSI2012, pp. 295 – 298, 2012.

7. Mainardi L, Rivolta MW, Scanziani R, Corino V, Sassi R. "Cancellation of ventricular activity in endocavitary recordings during atrial fibrillation by particle swarm optimization", Computing in Cardiology, vol. 38, pp. 597 – 600, 2011.

Abstract:

1. Rivolta MW, Sassi R, Stampalija T, Casati D, Frasch M, Richardson B, Ross MG, Rizas K, Bauer A, Ferrazzi E. "Correlation between Average Acceleration and Deceleration Capacity of Fetal Heart Rate and Biomarkers of Acid-Base Status in a Vivo Sheep Model", Reproductive Sciences, vol. 21, no. 3, pp. 171A – 171A, 2014.

2. Rivolta MW, Sassi R, Stampalija T, Casati D, Frasch M, Richardson B, Ross MG, Rizas K, Bauer A, Ferrazzi E. "In Vivo Evaluation of Acceleration and Deceleration Capacity of Fetal Heart Rate in Worsening Hypoxic Acidemia", Reproductive Sciences", vol. 21, no. 3, pp. 85A – 85A, 2014.

3. Stampalija T, Casati D, Maggi V, Rivolta MW, Lupini S, Rizas K, Sassi R, Bauer A, Ferrazzi E. "Analysis of Fetal ECG in Fetal Growth Restriction", Reproductive Sciences", vol. 21, no. 3, pp. 85A – 85A, 2014.

4. Rivolta MW, Badilini F, Mainardi LT, Vaglio M, Sassi R. "Quantification of ventricular repolarization heterogeneity during sotalol administration using the V-index", J Electrocardiol, vol. 46, no. 6, pp. 625 – 625, 2012.